Understanding the Physics of Liquid Crystalline Elastomers

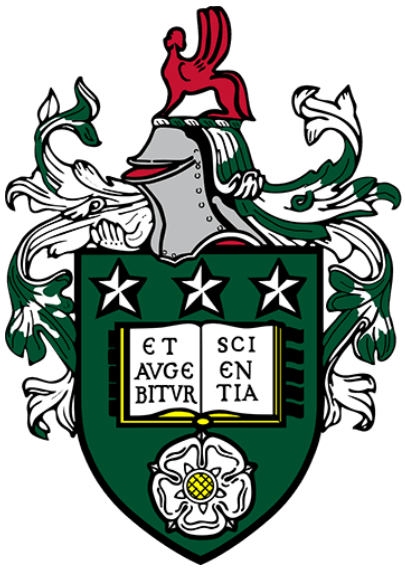

Emily Jane Cooper

School of Physics and Astronomy

University of Leeds

Submitted in accordance with the requirements for the degree of

Doctor of Philosophy

March 2025

The candidate confirms that the work submitted is her own, except where work which has formed part of jointly authored publications has been included. The contribution of the candidate and the other authors to this work has been explicitly indicated below. The candidate confirms that appropriate credit has been given within this thesis where reference has been made to the work of others. Any work that was not performed by the candidate, Emily Jane Cooper, is stated in the text or figure caption, throughout this thesis.

Chapter 3, **Chapter 4**, **Chapter 5**, and **Chapter 6** contain work that has been published in the following paper: Emily J. Cooper, Matthew Reynolds, Thomas Raistrick, Stuart R. Berrow, Ethan I. L. Jull, Victor Reshetnyak, Devesh Mistry, and Helen F. Gleeson. "Controlling the Optical Properties of Transparent Auxetic Liquid Crystal Elastomers". *Macromolecules*, 2024, *57* (5), 2030-2038. DOI: 10.1021/acs.macromol.3c02226.

Most of the experimental work and the writing of this paper was performed by Emily J. Cooper. Devesh Mistry and Helen F. Gleeson (supervisors of Emily J. Cooper) provided feedback, edits, and advice on the paper and its contents throughout. All authors provided feedback during writing.

Below, the specific contributions from the authors towards this paper will be provided, as well as any additional contributions towards this thesis that are separate from the paper.

Matthew Reynolds synthesised two monodomain nematic LCEs that were used for Raman Spectroscopy in **Chapter 5**: Section 5.2 (nLCE-75 and nLCE-84 appear in Figure 5.1, Figure 5.2, and Table 5-2). Matthew Reynolds also synthesised an isotropic LCE and a monodomain nematic LCE that were used for Abbé Refractometry in **Chapter 6**: the isotropic LCE appears in Section 6.5.1 (Figure 6.6) and the monodomain nematic LCE is used throughout **Chapter 6** (nLCE-62 appears in Figure 6.3, Figure 6.4, Figure 6.5, Figure 6.7, Figure 6.8, and Table 6-1).

Thomas Raistrick provided the Maier-Saupe theory fitting used in **Chapter 5** and **Chapter 7** (Figure 5.2, Figure 5.4, and Figure 7.4). Thomas Raistrick also performed Wide-Angle X-ray Scattering on a sample of poly-EHA (made by Stuart R. Berrow) which is shown in this thesis in **Chapter 5**: Section 5.4.3 (Figure 5.13C).

Stuart R. Berrow synthesised the sample of poly-EHA that is used in **Chapter 5** and **Chapter 6:** Section 5.4.3 (Figure 5.13C), Section 6.2 (Figure 6.2), and Section 6.5 (Figure 6.7). Stuart R. Berrow also measured the auxetic response of LCEs with 56 mol%, 62 mol%, and 64 mol% mesogenic content (which were made by Emily J. Cooper) in **Chapter 4**: Section 4.3.3 (Figure 4.9 and Table 4-3).

Ethan I. L. Jull synthesised a monodomain nematic LCE (nLCE-62) and measured its transmission spectroscopy, which is shown in **Chapter 6**: Section 6.2 (Figure 6.1); the Fresnel losses were corrected for by Ethan I. L. Jull and H. F. Gleeson (Figure 6.1).

Victor Reshetnyak provided theory on understanding the linear dependence of the transition temperatures from Maier-Saupe theory, which is given in **Chapter 4**: Section 4.3.1.

Chapter 4 features transition temperatures measured with Differential Scanning Calorimetry and Dynamic Mechanical Thermal Analysis. The errors in the transition temperatures were calculated from results by Aidan Street, Emily J. Cooper, Stuart R. Berrow, and Zhenming Wang.

The experimental Wide-Angle and Small-Angle X-ray Scattering that is used throughout **Chapter 5** was performed in collaboration between Devesh Mistry and Emily J. Cooper.

Conferences

- Poster Presentation at the International Liquid Crystal Society Conference, 2022, Lisbon, Portugal.
- Poster Presentation at the Bragg Exchange Conference, 2023, Leeds, U.K.
- Oral Presentation at the British Liquid Crystal Society Conference, 2023, Glasgow, U.K.
- Oral Presentation at the British Federation of Women Graduates Presentation Day, 2023, London, U.K.
- Poster Presentation at the International Optics of Liquid Crystal Conference, 2023, Szczecin, Poland.
- Oral Presentation at the University of Leeds Physics Postgraduate Symposium, 2024, Leeds, U.K.
- Oral Presentation at the Institute of Physics (IoP) Physical Aspects of Polymer Science Conference, 2024, Edinburgh, U.K.

Prizes and Bursaries

- **'*Crystals*' Poster Prize**, at the International Liquid Crystal Society Conference, 2022, Lisbon, Portugal.
- **Early Research Talk Prize** at the British Liquid Crystal Society Conference, 2023, Glasgow, U.K.
- **Bursary** from the British Liquid Crystal Society to attend the International Optics of Liquid Crystal Conference, 2023, Szczecin, Poland.
- **1st Place Talk Prize** at the University of Leeds Physics Postgraduate Symposium, 2024, Leeds, U.K.
- **Bursary** from the Soft Matter Physics Group at the University of Leeds to attend the Institute of Physics (IoP) Physical Aspects of Polymer Science Conference, 2024, Edinburgh, U.K.

Publications

- Emily J. Cooper, Matthew Reynolds, Thomas Raistrick, Stuart R. Berrow, Ethan I. L. Jull, Victor Reshetnyak, Devesh Mistry, and Helen F. Gleeson. “Controlling the Optical Properties of Transparent Auxetic Liquid Crystal Elastomers”. *Macromolecules*, 2024, *57* (5), 2030-2038. DOI: 10.1021/acs.macromol.3c02226.
- Emily J. Cooper. “Report on the British Liquid Crystal Society (BLCS) Annual Meeting, 19th-21st April 2023.” *Liquid Crystals Today*, 2023, 32 (2): 38–39. DOI:10.1080/1358314X.2023.2265791.

This thesis is dedicated to my younger self,

with her boundless ambition,

and a love for learning.

Acknowledgements

Without a doubt, this PhD has been the highlight of my Education.

I would like to thank all the people who have contributed to my education over the years. A special thanks goes to my PhD supervisors, Prof. Helen Gleeson, Dr Devesh Mistry, and Dr Peter Hine; thank you for all your unwavering support throughout this journey and for the countless hours of interesting discussions, honest advice, and all the fun moments in between. You have all been inspirational. Helen, I especially want to thank you for everything you have done for me on this journey that has been above and beyond. I also would like to thank the teachers that have had a lasting impact; my primary school teachers, Miss Hunt and Mrs Saunders, and my A-level Physics teacher, Mr Sidhu, who all made learning fun and developed in me a passion for learning.

During my PhD, I had the privilege to sit in office 1.35 – which is doubtlessly the best office. To work alongside such kind fellow PhD students has been a delight, and I want to thank you all. Adele, Afaf, Alex, Ardiana, Hessah, Meg, Sundus, and Viola: thank you especially for all the book swapping, the exchanging of propagated plants, and the much-needed tea breaks over the years. I know that I've made some friends for life.

Thank you to all my work colleagues and friends in the Soft Matter Physics Research Group and in the School of Physics and Astronomy. Dr Daniel Baker, I can't thank you enough for all your experimental help and support throughout my PhD. I would also like to thank those in 'Team LCE' for all the collaborative work and the exciting conversations: Aidan, Helen, Matt, Stuart, Tom, and Zhenming. It's been a pleasure to work on the same materials.

I would now like to thank my close friends that I started my undergraduate Physics journey with, particularly Anjali, Emma, Holly, and Rachael. Thank you for the frequent group calls, the spontaneous group games nights, the lovely visits to Leeds, and the wholesome weekends away. I look forward to our next adventures.

Last, but certainly not least, is an enormous thank you to all my family, since without their unconditional love and unwavering support, I simply could not have achieved all that I have. You are my greatest inspirations and my biggest supporters:

Mum and Dad, Nana Melty, Nana and Grandad, Great Uncle Sandy, Great Aunt Beryl, Ben, Sophie, and Brendan (and of course, Echo and Lyle). I hope I've made you all proud.

Finally, I would like to acknowledge how much my Mum and Dad have emotionally contributed to this journey. They have encouraged me to pursue every opportunity, have listened to me practice my conference presentations, and have always cheered me up, and cheered me on. They raised me to keep my aspirations high and helped to develop in me the courage to attain them. I am eternally grateful to you both.

Abstract

This thesis presents the ability to select an optimal material design for a specific function, such as laminates for impact resistant glass. This has been achieved by the full comprehension of the impact of templating and composition on the optical, physical, thermal, and mechanical properties of a series of acylate-based Liquid Crystalline Elastomers (LCEs).

The elastomeric materials were examined for three different templates, which display distinctive behaviour: the monodomain nematic, the polydomain nematic, and the isotropic. The transparent monodomain nematic template will be of particular interest since this exhibits an auxetic response to an applied strain and lends this material as a unique candidate for impact resistance. The composition was altered for this series of LCEs *via* the control of the mesogenic content within the network and was investigated between 51 - 84 mol% mesogenic content for the polymerized LCEs.

We demonstrate that a 10 mol% increase in the mesogenic content of an LCE (from 62 mol% to 72 mol%) subsequently provides a ~ 7°C higher glass transition temperature, an 11% increase in ordering, an enhanced energy dissipation, a 3% increase in density, and an 18% greater birefringence of the material. However, we also show that there is an upper limit of the mesogenic content that can be used to produce these monodomain nematic LCEs; at 72 mol% mesogenic content, we observe more smectic characteristics of the materials and a failure to display an auxetic response.

This work provides the formulation limitations and design rules for LCE materials and also offers an opportunity to select the ideal composition and template for a particular application. Following careful contemplation of all the materials, we will propose that the monodomain nematic material of 66 mol% mesogenic content is the optimal composition from this family of materials, as a laminate for impact resistant glass.

Contents

Symbols and Abbreviations

Symbols

$\vec{n}$	Director.
T	Temperature (°C or K).
T_{NI}	Nematic-to-Isotropic Transition Temperature (°C).
T_g	Glass Transition Temperature (°C).
$\langle P_2 \rangle$	Uniaxial Order Parameter (using second-order term of the Legendre polynomials).
$\langle P_4 \rangle$	Uniaxial Order Parameter (using fourth-order term of the Legendre polynomials).
β	The angle between the orientation of a mesogen and the director, $\vec{n}$ (°).
τ	The Exponent Fitting Parameter, used in the Haller model.
T^*	Critical Temperature, used in the Haller model (K, unless stated).
d	Layer spacing of a material, used in Bragg's Law (Å).
θ_{Bragg}	Diffraction angle of a material, used in Bragg's Law (°).
m	Order of diffraction of a material, used in Bragg's Law.
λ	Wavelength (nm).
q	Reciprocal Space ($= \frac{2\pi}{d}$, nm^{-1}).
χ	Azimuthal Angle defined for use in X-ray Scattering (°).
φ	Radial Angle defined for use in X-ray Scattering (°).
$I(\chi)$	Scattering Intensity along the Azimuthal Angle, χ.
$I(\varphi)$	Scattering Intensity along the Radial Angle, φ.
f_{2b}	Kratky Fitting Parameters, related to the ODF (b = 0, 1, 2, 3, 4, 5).
θ	Sample Rotation (°).

$I_{\parallel}$ Scattering Intensity for Parallel Polarization (used for PRS).

$I_{\perp}$ Scattering Intensity for Perpendicular Polarization (used for PRS).

r Differential Polarizability Ratio (used for PRS).

n_o Ordinary Refractive Index (anisotropic material).

n_e Extraordinary Refractive Index (anisotropic material).

Δn Birefringence (anisotropic material).

n_{av} Average Refractive Index (anisotropic material).

n_{iso} Isotropic Refractive Index (isotropic material).

n_{pEHA} Refractive Index of poly-EHA (pEHA).

$n_{mesogen}$ Refractive Index of a purely mesogenic material.

$\frac{dn}{dT}$ The Temperature Coefficient of Refractive Index.

$tan\delta$ Loss Tangent (ratio of loss modulus over storage modulus).

$\varepsilon_{x/y/z}$ Strain along the *x/y/z* axis of the LCE.

L_{perp} Length of an LCE perpendicular to the director.

L_{para} Length of an LCE parallel to the director.

L_x, L_y Orthogonal axes of an LCE.

$\Delta L/L_0$ Relative Length Change along axis, where L_0 is the length at 25°C.

$\alpha_{\parallel}$ The Polarizability along the director.

$\alpha_{\perp}$ The Polarizability perpendicular to the director.

$\bar{\alpha}$ The Average Polarizability.

$\Delta\alpha$ The difference in Polarizability.

ρ_{sol} Density of solution.

ρ_{LCE} Density of LCE.

$\langle P_2 \rangle_T$ The Temperature Dependent Order Parameter, at T (°C).

$\langle P_2 \rangle_0$ The Order Parameter measured at 25°C.

t Time.

A Upper limit of Order Parameter for a maximum mesogenic content.

M Mole Fraction mesogenic content in an LCE.

c Concentration of non-mesogenic component in LCE.

c^* Critical Concentration of a nematic LCE, above which the system is isotropic.

$\xi_{\parallel}$ The Correlation Length parallel to the director.

$w_{\parallel}$ Full Width Half Maximum of a scattering feature orientated parallel to director.

$\sigma_{critical}$ Critical Field Strength.

Abbreviations

LC Liquid Crystal.

LCP Liquid Crystalline Polymer.

LCE Liquid Crystalline Elastomer.

nLCE Nematic Liquid Crystalline Elastomer. The suffix indicates the composition (nLCE-62 is a nematic LCE containing 62 mol% mesogenic content).

iLCE Isotropic Liquid Crystalline Elastomer.

sLCE Smectic Liquid Crystalline Elastomer.

wt.% Weight percentage.

mol% Mole percentage.

MESSE Microscope Elastomer Stress Strain Enclosure.

DSC Differential Scanning Calorimetry.

DMTA Dynamic Mechanical Thermal Analysis.

SAXS Small Angle X-ray Scattering.

WAXS Wide Angle X-ray Scattering.

PRS Polarized Raman Spectroscopy.

POM Polarized Optical Microscopy.

UV Ultraviolet light.

ODF Orientational Distribution Function.

EHA 2-ethylhexyl acrylate.

pEHA Poly(2-ethylhexyl acrylate).

MBF Methyl benzoylformate.

A6OCB 6-(4-cyano-biphenyl-4'-yloxy)hexyl acrylate.

RM82 1,4-bis-[4-(6-acryloyloxyhexyloxy)benzoyloxy]-2-methylbenzene.

6OCB 4-cyano-4'-hexoxybiphenyl.

5CB 4-Cyano-4'-pentylbiphenyl.

LaB_6 Lanthanum hexaboride.

AgBeh Silver behenate.

List of Figures

List of Tables

Chapter 1 Motivation

1.1 Motivation

In 2018, a new class of elastomeric materials with a unique response to strain were discovered by Mistry *et al.* (1). Above some threshold of applied strain, these non-porous materials have exhibited an *auxetic behaviour*, in which the material can thicken along an axis orthogonal to the applied strain (1). This unique auxetic behaviour recommends these materials as strong candidates for impact resistance applications, such as laminates in impact resistant glass (2).

Specifically, these elastomeric materials first developed by Mistry *et al.* (1), are a type of Liquid Crystalline Elastomer (LCE) and are formed of loosely crosslinked liquid crystalline polymers. The coupling of the liquid crystalline and the elastomeric properties allows for highly ordered and birefringent soft materials (2). Therefore, the motivation for this thesis is to characterise the full properties of this unique class of materials, to allow for both the optimisation of specific properties, and the selection of an ideal material *via* clear design rules.

Indeed, there has always been a drive to optimize polymeric material properties for real world applications, which is guided by the need to improve factors such as the performance and the cost. Understandably so, the control of the material behaviour is crucial to ensure optimisation for applications. In fact, polymeric materials that are frequently used in applications, such as polystyrene and polyester, will often have their properties recorded in datasheets. These datasheets log the material's behaviour to stimuli, such as temperature, light, and strain. (3)

In this thesis, we will fully characterise the various material properties of a series of auxetic LCEs, that were first developed by Mistry *et al.* (1). By reporting the material properties in a manner like the datasheets for commercial polymeric materials, we can provide the opportunity to customise the LCE properties with composition for specific applications.

1.2 Thesis Structure

The underlying motivation for the work in this thesis has been provided within this chapter, and additional motivations are provided at the beginning of each results chapter to offer context to each investigation. A summary of this thesis shall be outlined below, and a flow diagram of the structure is displayed in Figure 1.1.

Chapters 1 - 3 are the introductory chapters of this thesis and will provide the reader with an understanding of the important principles for the research presented herein. **Chapter 2** will provide the relevant background knowledge of liquid crystalline and polymeric materials, before the relevant experimental techniques are described in **Chapter 3**.

Chapter 4 - 7 will present and discuss the results of this investigation and the chapters shall be separated by the properties investigated. The results given in **Chapters 4 - 6**, will feed into the last results chapter, **Chapter 7**. An abridged overview of each results chapter shall now be given.

Chapter 4 will outline the role of composition, phase, and templating on the various physical properties of this series of LCEs. Specifically, this will include the thermal and mechanical properties of the network. The thermal properties will include the transition temperatures of a series of precursor mixtures and polymerized LCEs that will be investigated using Differential Scanning Calorimetry (DSC). The mechanical properties of the network will be explored using the techniques of Dynamic Mechanical Thermal Analysis (DMTA) and an in-house Microscope Elastomer Stress Strain Enclosure (MESSE), which measure the dissipative properties and the auxetic behaviour of the networks, respectively.

Chapter 5 will continue the investigation into the material properties and will present the interesting roles that composition and templating have on the ordering and the structure of the polymerized network. The order parameters of the networks will be measured using both Raman Spectroscopy and X-ray Scattering. Using X-ray Scattering, the network structure and the correlation lengths of the materials can also be determined and will be compared to results for similar materials. Lastly, the density of these materials shall be measured using aqueous glycerol-solutions and shown to be dependent on the material composition.

Chapter 6 will then move on to discuss the tuneable optical properties of these materials, including the average refractive index, the ordinary and extraordinary refractive indices, and the birefringence. These properties shall predominantly be measured using Abbé Refractometry. The bulk of this chapter includes work that has been published in a first-author paper by Cooper *et al*. (2).

Finally, **Chapter 7** will explore the evidence of an order-to-disorder transition in the nematic LCEs, making use of optical and thermo-mechanical techniques to explore details of the materials at higher temperatures. This chapter will feature direct measurements of the temperature-dependent order parameters using Raman Spectroscopy.

The work of this thesis will be concluded in **Chapter 8**, which will summarise the novel results reported here, propose the best material as a laminate in impact resistant glass, and outline potential future work.

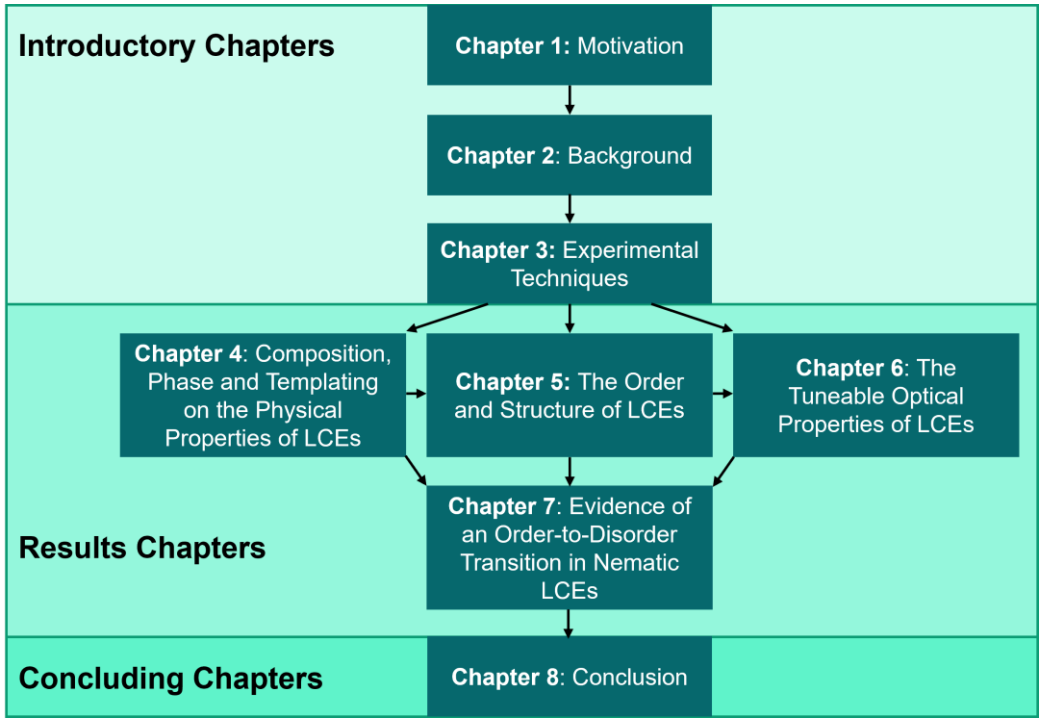

Figure 1.1. A flow diagram to illustrate the structure of this thesis, with introductory chapters (Chapters 1 - 3), results chapters (Chapters 4 – 7), and concluding chapters (Chapter 8). The results chapters (Chapters 4 - 6) will feed into the last results chapter, Chapter 7.

1.3 References

1. Mistry, D., Connell, S.D., Mickthwaite, S.L., Morgan, P.B., Clamp, J.H. and Gleeson, H.F. Coincident molecular auxeticity and negative order parameter in a liquid crystal elastomer. *Nature Communications.* 2018, **9**(1), p.5095. Available from: https://doi.org/10.1038/s41467-018-07587-y
2. Cooper, E.J., Reynolds, M., Raistrick, T., Berrow, S.R., Jull, E.I.L., Reshetnyak, V., Mistry, D. and Gleeson, H.F. Controlling the Optical Properties of Transparent Auxetic Liquid Crystal Elastomers. *Macromolecules.* 2024, **57**(5), pp.2030-2038. Available from: https://doi.org/10.1021/acs.macromol.3c02226
3. Campo, E.A. 1 - Polymeric Materials and Properties. In: Campo, E.A. ed. *Selection of Polymeric Materials*. Norwich, NY: William Andrew Publishing, 2008, pp.1-39.

Chapter 2 Background

2.1 An Introduction to Liquid Crystals: Microscopic to Macroscopic

In this thesis, we will explore the various properties of a series of materials that are known as *Liquid Crystalline Elastomers* (LCEs), which are named as such to directly reflect their incorporation of molecules called *liquid crystals* into an elastomeric network. Before we can begin to appreciate the physics of LCEs, we must first comprehend the significant properties and phases of liquid crystals. We shall therefore build our understanding from the microscopic liquid crystalline molecules to the macroscopic Liquid Crystalline Elastomers.

The following chapter will provide a broad background on liquid crystalline materials, including the transition temperatures, the order parameters and the anisotropic refractive indices, since these will be relevant throughout this thesis. The transition temperatures and the mechanical properties relevant to amorphous polymeric networks will also be briefly introduced here, with additional information provided in the relevant experimental chapters.

2.1.1 Liquid Crystals

Liquid crystalline materials are widely used, and their science is relevant to a range of applications, including displays, soaps, and lubricants. These materials are significant due to their manifestation of liquid crystalline phases, in which characteristics of both typical liquid and solid phases can be exhibited. Specifically, within liquid crystalline phases an orientational order (like a crystalline solid) is established whilst the material is still capable of flow (like an isotropic liquid). (1)

Liquid crystals can be further distinguished based on their behaviour. Of particular importance to this work are a class of thermally responsive materials, called *thermotropic liquid crystals*; herein out, we shall simply refer to thermotropic liquid crystals as *mesogens*. Interestingly, these materials can transition between disordered phases and ordered liquid crystalline phases at discrete temperatures, which are forms of *transition temperatures*. A good background on these thermally responsive materials can be found in textbooks such as those by Collings and Goodby (1), and Vertogen and de Jeu (2).

2.1.2 Liquid Crystalline Polymers

The following section will concern the incorporation of thermotropic liquid crystals (mesogens) into Liquid Crystalline Polymers (LCPs). Mesogens can be integrated into polymer chains in different configurations, and two simple examples of this are side-chain and main-chain polymers, which are shown in a schematic in Figure 2.1. In this example of a side-chain polymer, the mesogenic units are clearly distinct from the continuous polymer backbone and are attached laterally to the backbone. For the main-chain polymer, the mesogens are attached in a linear configuration within the polymer backbone. The design and the properties of various side-chain polymers have been previously detailed, and further information can be found in the following textbook chapters (3, 4).

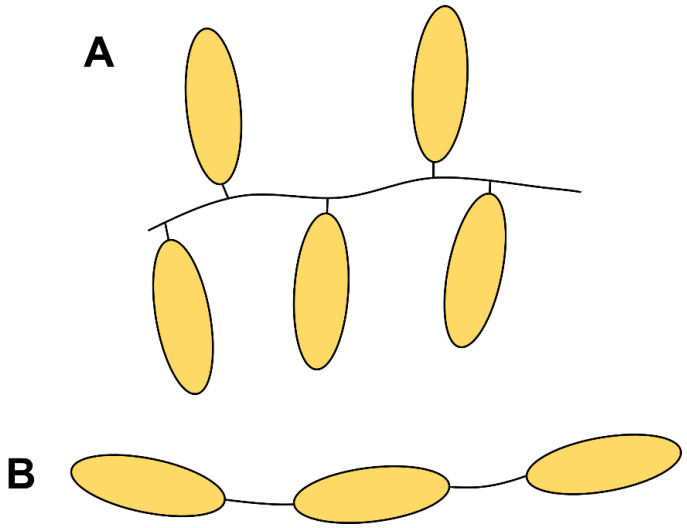

Figure 2.1. A schematic of simple (A) side- and (B) main- chain liquid crystalline polymers. The thermotropic liquid crystals (mesogens) are shown as yellow rods, and the backbone is indicated with a black line.

2.1.3 Liquid Crystalline Elastomers

The subsequent crosslinking of Liquid Crystalline Polymers (LCPs) leads to the construction of Liquid Crystalline Networks (LCNs). A simple representation of an ordered and lightly crosslinked LCN is shown in Figure 2.2. This type of network is known as a Liquid Crystalline Elastomer (LCE), and this form of material is of importance to the ensuing work in this thesis.

The first LCE was formulated by Finkelmann in 1981 and was in fact a siloxane-based material composed of crosslinked main-chain LCPs (5). However, the key

arrangement of LCEs that will be explored in this research are formed of side-chain LCPs, as shown in the schematic in Figure 2.2.

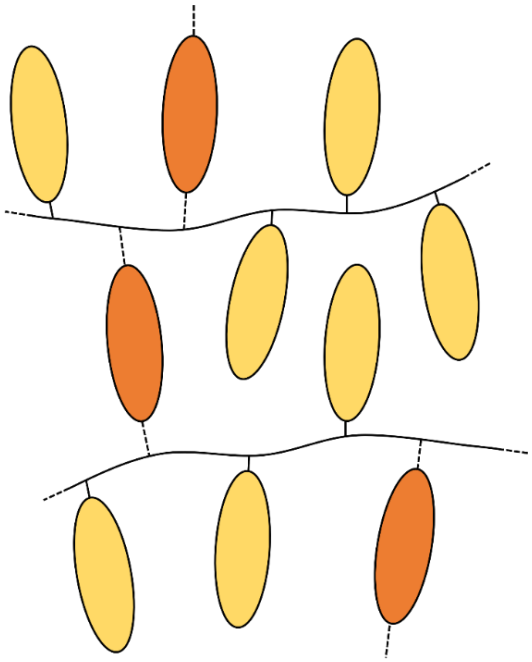

Figure 2.2. A simple schematic of a loosely crosslinked Liquid Crystalline Network (LCN), known as a Liquid Crystalline Elastomer (LCE). This ordered network is formed of side-chain liquid crystalline units (mesogens) and a mesogenic crosslinker. The mesogenic side groups are indicated in yellow, the mesogenic crosslinker is indicated in orange, the polymer backbone is an unbroken black line. The mesogenic crosslinker is connected to the polymer backbone via a spacer, indicated here by dashed black lines.

Since the materialisation of LCEs, there have been significant advances to the range of possible synthesis and alignment techniques for these materials, and further information can be found in a recent review by Herbert *et al.* (6). As a result of pushing the development of LCEs, these materials have achieved remarkable material properties and responses; light-sensitive LCEs can travel across water (7), whilst other LCEs possess mechanical behaviour similar to muscles (8) and can be electrically stimulated to actuate like an artificial muscle for soft robotics (9, 10), and to perform as self-cleaning coatings (11). As aforementioned in Section 1.1, another remarkable LCE was discovered recently by Mistry *et al.* (12) and these materials are capable of an auxetic behaviour, in which the material thickens above a threshold of applied strain and is therefore ideal for impact resistance. Clearly, there is a wide span of proposed functions of LCEs due to the variety of material responses.

Crucially, polymeric networks incorporating thermotropic mesogens retain the ability to transition between ordered liquid crystalline phases and disordered phases. Furthermore, the selected density of the crosslinking and the overall mesogenic content of the network will have an influence on the network properties, including the temperatures at which the material transitions occur (13, 14). We shall now review the phases of liquid crystalline materials that are relevant to this thesis.

2.2 The Phases and Templates of Liquid Crystalline Elastomers

Liquid crystalline materials can exhibit a variety of liquid crystalline phases, and in this work, the smectic and nematic phases are of particular interest. The nematic phase exhibits orientational order of the mesogens, however there is no positional order. The ordering of the material is along a unit vector known as the director, $\vec{n}$, and is indicated in Figure 2.3 for each material. In the smectic phase, there is an orientational order along the director and an additional positional order, with the mesogens forming 'smectic layers'. LCEs can also form a typical disordered phase, known as isotropic, in which the mesogens have no ordering. The organisation of the nematic, smectic, and isotropic phases of LCEs can be seen in Figure 2.3. However, to further discuss the arrangement of the mesogens shown in Figure 2.3, we must first introduce important terminology.

To describe in detail the forms of alignment within LCEs, the terms '*template'* and '*phase'* will be distinct from each other in this thesis. The phrase '*template'* will consider the nature of the director within the material, which is not necessarily characterised by the '*phase'*. To elaborate on these further, different phases and templates are presented in Figure 2.3 below. There are three phases of LCEs shown, and these are of decreasing order: smectic, nematic, and isotropic (no ordering). For the nematic phase, there are two different nematic templates shown, which are known as the monodomain nematic and polydomain nematic. These two templates clearly have different macroscopic behaviour of the director, despite being the same phase. The monodomain nematic displays a single director across the whole material, whereas the polydomain nematic has regions of alignment along a director, but each region is random across the material.

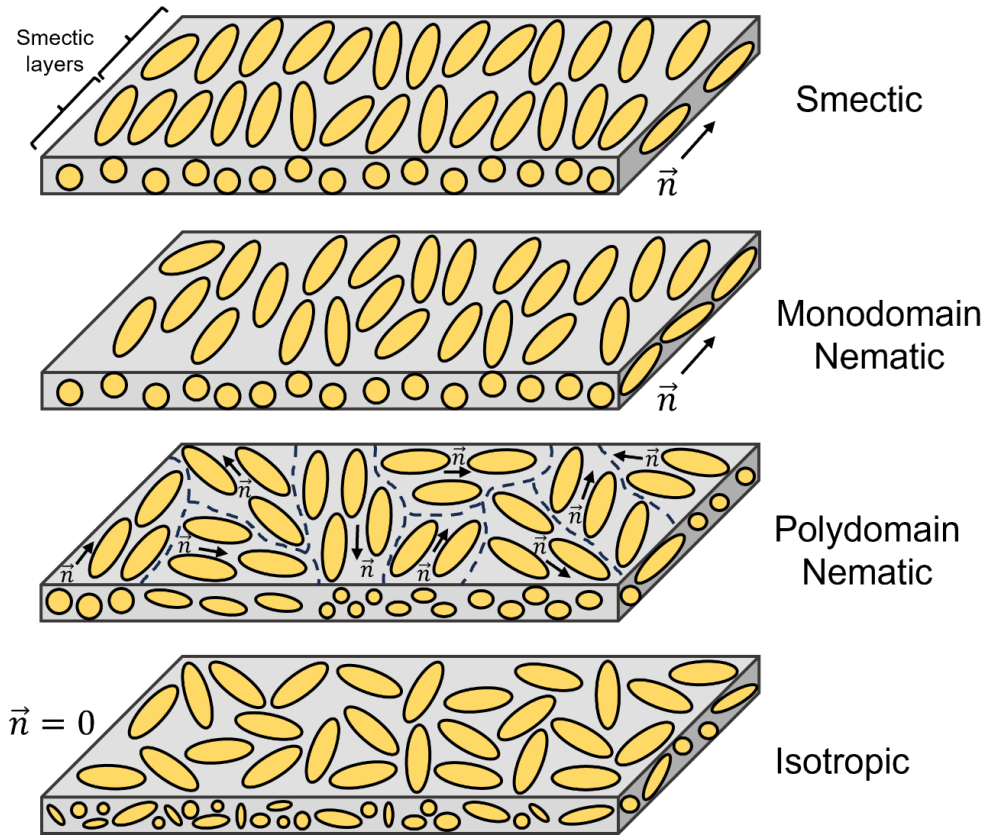

Figure 2.3. A schematic of the smectic, monodomain nematic, polydomain nematic, and isotropic templates of a Liquid Crystalline Elastomer (LCE). The mesogens (yellow rods) are aligned along a single director ($\vec{n}$) across the smectic and monodomain nematic LCEs, aligned along a director within small regions in the polydomain nematic LCE, and are not aligned in the isotropic LCE. The smectic LCE forms smectic layers parallel to the director.

Due to the differences in the nature of the above templates and phases, we will observe different properties for each material. For example, the uniaxial alignment of the mesogens in the smectic and the monodomain nematic templates will result in anisotropic material properties that are dependent on the axis of the material that is probed. Obviously, the isotropic template has no ordering within the material and is therefore always isotropic in nature. Despite having regions of an anisotropic nature, the polydomain nematic LCE shows no uniaxial director throughout the material; therefore, the polydomain nematic LCE displays an interesting range of properties which shall be explored in this thesis.

For further information, a detailed overview of Liquid Crystalline Elastomers can be accessed in the textbook by Warner and Terentjev (15).

2.3 The Transition Temperatures

With a sufficient increase in temperature, liquid crystalline materials can transition through ordered phases to a disordered (isotropic) phase and these transitions occur at discrete temperatures. A particularly relevant liquid crystalline transition to this work, is the transition between the nematic and isotropic phases. This nematic-to-isotropic transition has an associated transition temperature that shall be referred to as T_{NI}. This transition is typically a weakly first order (discontinuous) transition in low molar mass liquid crystals. Intriguingly, the nematic-to-isotropic transition has also been observed as continuous in nature for crosslinked liquid crystalline materials, such as LCEs (16, 17). These transitions are associated with a number of changes to the material properties, which shall be examined in this chapter and evidenced throughout this thesis. (1)

Another key transition temperature that is used in this work is known as the glass transition temperature, T_g, which is a particularly important transition to amorphous polymers (18). Below T_g the network is glassy; above this temperature, the network is rubbery (18). Therefore, the glass transition temperature is an important control for polymeric materials and can limit the operational temperature of applications. We shall briefly revisit the glass transition temperature in Section 2.6.

Lastly, we will use various techniques to measure the transition temperatures throughout this thesis, and these techniques shall be outlined in the following chapter, in Section 3.3.

2.4 The Order Parameters

The orientational ordering of the mesogens within a liquid crystalline phase are quantified by the order parameters. The second and fourth order terms of the Legendre polynomials are important for measuring the order parameters of nematic liquid crystals, and these are used to define the statistical average of the order parameters, $\langle P_2 \rangle$ and $\langle P_4 \rangle$. These are the foremost order parameters and are described respectively by Equation 2-1 and Equation 2-2 below. In these equations, β is the angle between the orientation of a mesogen and the director ($\vec{n}$) of the material, as indicated in Figure 2.4. (19-21)

$$\langle P_2 \rangle = \frac{1}{2}(3\langle \cos^2 \beta \rangle - 1) \qquad \textit{Equation 2-1}$$

$$\langle P_4 \rangle = \frac{1}{8}(35\langle \cos^4 \beta \rangle - 30\langle \cos^2 \beta \rangle + 3) \qquad \textit{Equation 2-2}$$

The uniaxial order parameter in Equation 2-1 is particularly important and is usually referred to as $\langle P_2 \rangle$. This order parameter can take values between 0 and 1; a material with no ordering has an order parameter of 0, and a material with a perfect alignment has an order parameter of 1 (2). However, for liquid crystalline phases, $\langle P_2 \rangle$ is typically between ~ 0.3 and 0.8 (2).

The Orientational Distribution Function (ODF) describes the probability of the orientation of a specific mesogen and is closely related to the order parameters. Specifically, the ODF considers the angle, β, between the mesogen's orientation and the director, $\vec{n}$. (19, 22)

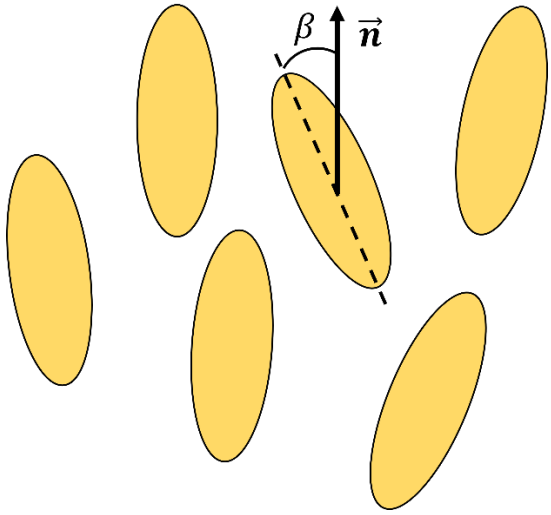

Figure 2.4. A schematic an anisotropic nematic material, with an average orientation of the mesogens along the director, $\vec{n}$. The angle, β, is between the principal axis of a mesogen and the director, $\vec{n}$.

Crucially, the order parameter of a liquid crystalline material is temperature-dependent; recall that a material can transition from an ordered liquid crystalline phase to a disordered phase upon heating, and vice versa. The variation of the order parameter, $\langle P_2 \rangle$, for a series of low molar mass liquid crystals heated through the nematic-to-isotropic transition is shown in Figure 2.5 by Gleeson *et al.* (23). The reduction in the order parameter, $\langle P_2 \rangle$, towards the nematic-to-isotropic transition is well described by the Haller model (24) and is given in Equation 2-3 below. This relation requires the temperature in Kelvin (T) and describes a critical temperature

(T^*) typically just above T_{NI}, in which the order parameter discontinuously changes to zero. Lastly, the Haller model describes an exponent fitting constant (τ), which typically takes values between 0.17- 0.23. (24)

$$\langle P_2 \rangle = \left(1 - \frac{T}{T^*}\right)^{\tau} \qquad \textit{Equation 2-3}$$

Further background information on the Orientational Distribution Function (ODF) and the order parameters of liquid crystalline materials can be found in several textbooks, some of which have been listed here (2, 19, 22, 25).

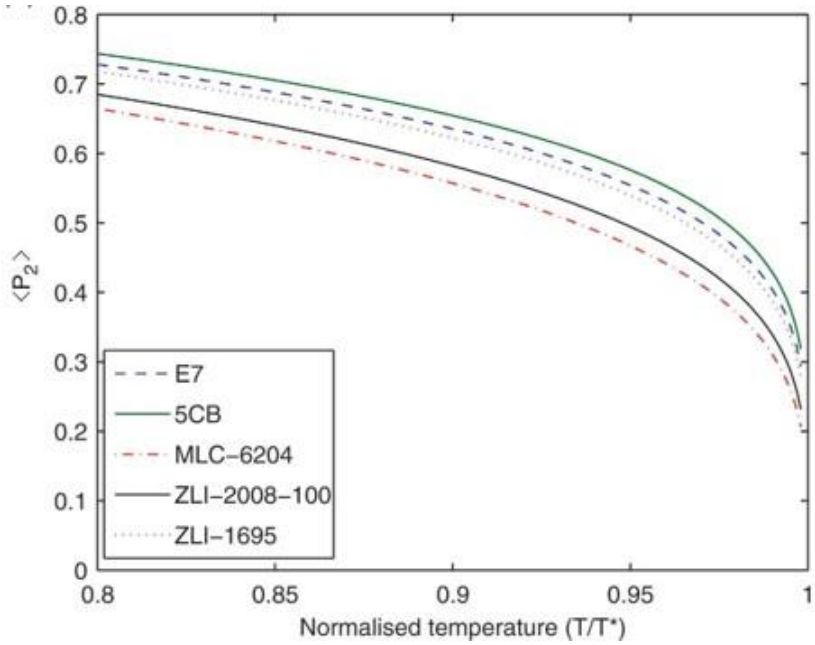

Figure 2.5. The order parameters of various liquid crystalline materials, which decrease in order parameter, $\langle P_2 \rangle$, with an increase in the temperature. This example shows the discontinuous transition from the nematic to the isotropic phase, which occurs as the normalised temperature, T/T, approaches a value of 1. The reduction in the order parameter below the critical temperature is well-described by the Haller model (24), as shown in Equation 2-3. This figure is taken from Gleeson et al. (23).*

From an experimental perspective, the order parameter $\langle P_2 \rangle$ can be readily measured using a range of techniques including, but not limited to, birefringence, Nuclear Magnetic Resonance (NMR), Raman Spectroscopy and X-ray Scattering. However, the order parameter $\langle P_4 \rangle$ proves difficult to measure and its quantification is limited to fewer techniques. Raman Spectroscopy and X-ray Scattering are techniques that are well known to be capable of measuring both order parameters, $\langle P_2 \rangle$ and $\langle P_4 \rangle$, and shall be used within this thesis. (21, 22, 26)

The main principles of determining order parameters using X-ray Scattering and Raman Spectroscopy shall be outlined below. We shall particularly focus on X-ray Scattering since this methodology has been recently introduced to our research group, whereas the technique of Raman Spectroscopy is familiar and regularly used. Further information about the practicalities of these techniques will be later provided in Section 3.4.

2.4.1 X-ray Scattering

X-ray Scattering is a form of elastic scattering that is well described by Bragg's Law (19, 27). The constructive interference of scattered light for a material with layer spacings of d, and an incident angle of θ_{Bragg}, must occur at a path difference of $m\lambda$, where m describes the order of diffraction. X-ray scattering utilizes the principle of Bragg's Law to reveal the internal structures of a material; any repeat distances within a material will form constructive interference observed at $2\theta_{Bragg}$ with a detector.

$$m\lambda = 2d \sin \theta_{Bragg} \qquad \textit{Equation 2-4}$$

The technique of X-ray Scattering is subdivided into Small Angle (SAXS) and Wide Angle (WAXS) X-ray Scattering. As one would presume, SAXS investigates the smaller angles resulting from the scattering and is investigated experimentally *via* a larger distance between the sample and the detector. The resultant scattering from SAXS typically provides information on the longer-range ordering within a material, for example, the layers present in the smectic phase (19). Correspondingly, WAXS utilises the wider scattering angles to probe the smaller structures and is especially used to measure the side-to-side molecular spacing of a material; this spacing is typically around ~ 4.5 Å for hydrocarbon molecules (19). The scattering of the side-to-side spacing can also be used to measure an order parameter of the material.

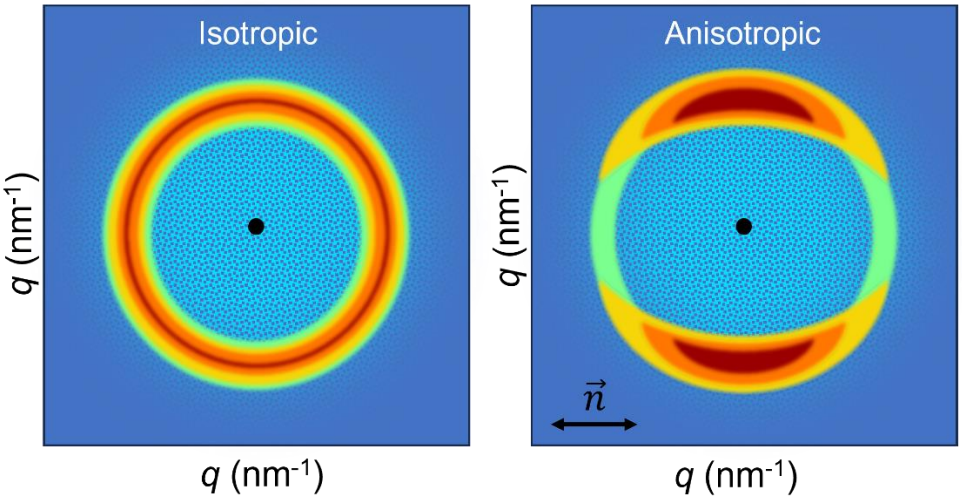

Figure 2.6. A simple schematic of the Wide-Angle X-ray Scattering (WAXS) pattern from an isotropic LCEs and an anisotropic (nematic) LCE, in reciprocal space (q, nm^{-1}). The anisotropic material has a director, $\vec{n}$, as indicated.

The phase of a material can, in principle, be identified through analysis of X-ray Scattering. As shown schematically in Figure 2.6, an isotropic material, or one with no macroscopic ordering, would produce diffused scattering rings in the reciprocal space ($q = \frac{2\pi}{d}$, nm^{-1}) with WAXS. There is therefore some difficulty with differentiating between an isotropic LCE and a polydomain nematic LCE when using WAXS; recall that the polydomain nematic template has no macroscopic ordering of the material.

Anisotropic scattering is also represented in Figure 2.6, with a scattering pattern that may be observed for nematic materials. The anisotropy is characterized by the arc-shaped scattering features. However, the manifestation of anisotropic scattering features can vary depending on the alignment and the phase of such a material. For example, a smectic phase would display sharp anisotropic features that appear at smaller scattering angles (towards the SAXS regime) and can be attributed to the smectic layer structure (19).

A methodology known as the Kratky method can be used to extract the order parameters from X-ray Scattering (20, 28) and this method utilises order parameter equations described by Davidson *et al.* (29). The complete methodology has been previously detailed by Sims *et al.* (20), but an overview shall be provided below.

First, a simplified schematic of the scattering that may be observed for an anisotropic material, is shown again in Figure 2.7A below. In this schematic, the anisotropic arc that is attributable to the side-to-side scattering has been highlighted and an angle known as the azimuthal angle (χ) has been defined. Figure 2.7B shows the scattering intensity of this anisotropic arc as a function of the azimuthal angle.

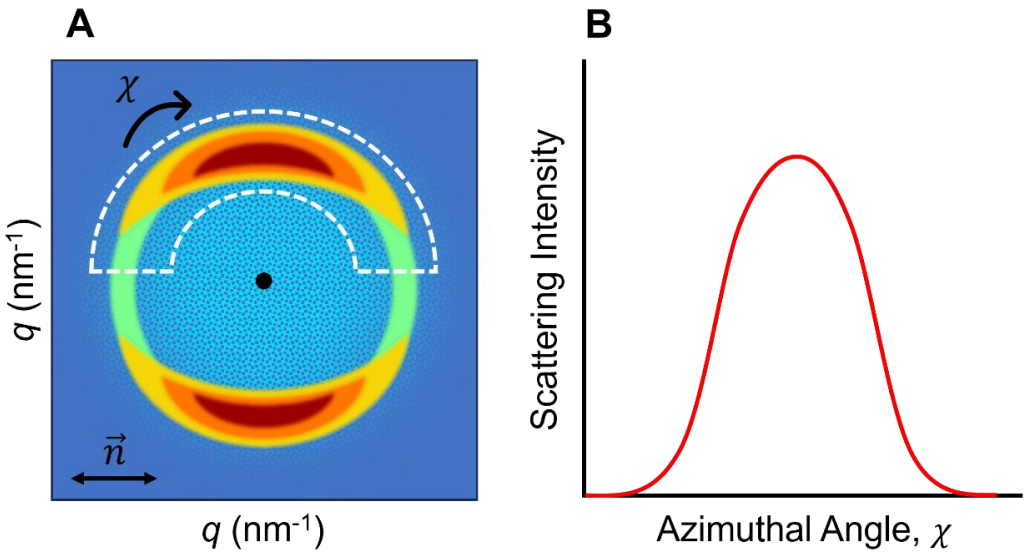

Figure 2.7. (A) A schematic of the scattering intensity of an anisotropic material, shown in reciprocal space, q (nm^{-1}). The scattering intensity of the anisotropic arc is being investigated (white dashed line) as a function of the azimuthal angle, χ, and a schematic of the resultant intensity figure is shown in (B).

A fitting to the scattering intensity (Figure 2.7B) can be performed using the first six terms of an expansion of the intensity, $I(\chi)$, according to Equation 2-5. This equation has terms of f_{2b} (b = 0, 1, 2, 3, 4, 5, …) and these parameters are related to the Orientational Distribution Function (ODF) (20).

$$I(\chi) = f_0 + \frac{1}{2} f_2 \cos^2\chi + \frac{3}{8} f_4 \cos^4\chi + \frac{5}{16} f_6 \cos^6\chi + \frac{35}{128} f_8 \cos^8\chi + \frac{63}{256} f_{10} \cos^{10}\chi + \cdots \quad \textit{Equation 2-5}$$

The first six terms of f_{2b} can be found by fitting Equation 2-5 to the experimental intensity in Figure 2.7B. These terms are then used to calculate approximated terms of $\langle \cos^2\beta \rangle$ and $\langle \cos^4\beta \rangle$ according to Equation 2-6 and Equation 2-7 (29). It is worth noting that Equation 2-6 and Equation 2-7 are adapted to only consider the first six terms of the intensity expansion from Equation 2-5, whilst the original equations by Davidson *et al.* technically consider b to ∞ (20, 29).

$$\langle \cos^2 \beta \rangle \approx \frac{\sum_0^5 \frac{f_{2b}}{2b+3}}{\sum_0^5 \frac{f_{2b}}{2b+1}} \qquad \textit{Equation 2-6}$$

$$\langle \cos^4 \beta \rangle \approx \frac{\sum_0^5 \frac{f_{2b}}{2b+5}}{\sum_0^5 \frac{f_{2b}}{2b+1}} \qquad \textit{Equation 2-7}$$

Lastly, Equation 2-6 and Equation 2-7 can be input into the equations for $\langle P_2 \rangle$ and $\langle P_4 \rangle$, which were given in Equation 2-1 and Equation 2-2. The methodology outlined here will be used in this work to determine the order parameters of anisotropic LCEs. Further information regarding the determination of order parameters with X-ray Scattering can be found in the following sources (19, 20, 29).

2.4.2 Raman Spectroscopy

Polarized Raman Spectroscopy (PRS) is an inelastic scattering technique that can be used to identify the vibrational modes and characterise the bonds present within a material. The mode that corresponds to the phenyl breathing (Raman shift of 1606 cm^{-1}) is often used to determine the order parameters, $\langle P_2 \rangle$ and $\langle P_4 \rangle$, for uniaxial nematic liquid crystalline systems (22, 30). This technique utilises a methodology outlined by Southern *et al.* (31) that has been previously demonstrated to effectively measure the order parameters, $\langle P_2 \rangle$ and $\langle P_4 \rangle$, for liquid crystalline materials (13, 30-37).

In brief, the order parameters can be extracted by the scattering intensity functions for the parallel and perpendicular polarizations (Equation 2-8 and Equation 2-9). These Equations are a function of the sample rotation (θ), the differential polarizability ratio (r), and the uniaxial order parameters, $\langle P_2 \rangle$ and $\langle P_4 \rangle$. Using these Equations, the depolarization ratio, $\frac{I_\perp}{I_\parallel}$, can be determined.

$$I_\parallel = \frac{1}{5} + \frac{4r}{15} + \frac{8r^2}{15} + \langle P_2 \rangle \left[\frac{1}{21}(3 + r - 4r^2)(1 + 3\cos 2\theta)\right] + \langle P_4 \rangle \left[\frac{1}{280}(1 - r)^2(9 + 20\cos 2\theta + 35\cos 4\theta)\right] \qquad \textit{Equation 2-8}$$

$$I_{\perp} = \frac{1}{15}(1-r)^2 + \langle P_2 \rangle \left[\frac{1}{21}(1-r)^2\right] + \langle P_4 \rangle \left[\frac{1}{280}(1-r)^2(3 - 35\cos 4\theta)\right]$$ *Equation 2-9*

By fitting the depolarization ratio, $\frac{I_{\perp}}{I_{\parallel}}$, as a function of the sample rotation, the differential polarizability ratio and the order parameters can be extracted, with the order parameters measured to an accuracy of 0.05 (35). An example of the depolarization ratio fitting can be seen in Figure 2.8.

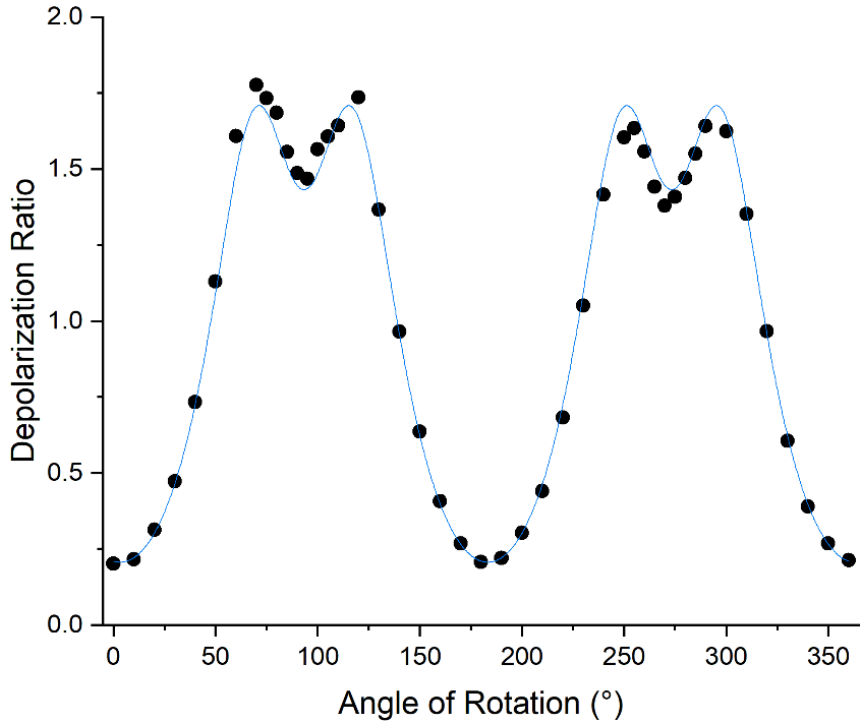

Figure 2.8. An example of a fitting of the depolarization ratio, $\frac{I_{\perp}}{I_{\parallel}}$, calculated from the ratio of Equation 2-8 and Equation 2-9 for a monodomain nematic LCE. Here, the fitting to the depolarization ratio gives parameters of $\langle P_2 \rangle = 0.54 \pm 0.05$, $\langle P_4 \rangle = 0.24 \pm 0.05$ and $r = -0.26 \pm 0.01$. This figure has been published by Cooper et al. (13).

2.5 The Optical Properties of Liquid Crystals

In this section, a background on the optical properties of liquid crystalline materials shall be provided, since the optical properties of LCEs will be later explored in Chapter 6.

An isotropic material, such as a disordered liquid, will exhibit a single refractive index, which is referred to as the isotropic refractive index, n_{iso}. However, due to the anisotropic nature of an aligned liquid crystalline material, there are two distinct refractive indices that are known as the ordinary and extraordinary refractive indices, n_o and n_e, respectively. In this work, the extraordinary refractive index is parallel to the director ($\vec{n}$), whereas the ordinary refractive index is perpendicular to the director ($\vec{n}$). A schematic of the ordinary and extraordinary axes can be seen in Figure 2.9 for a nematic phase.

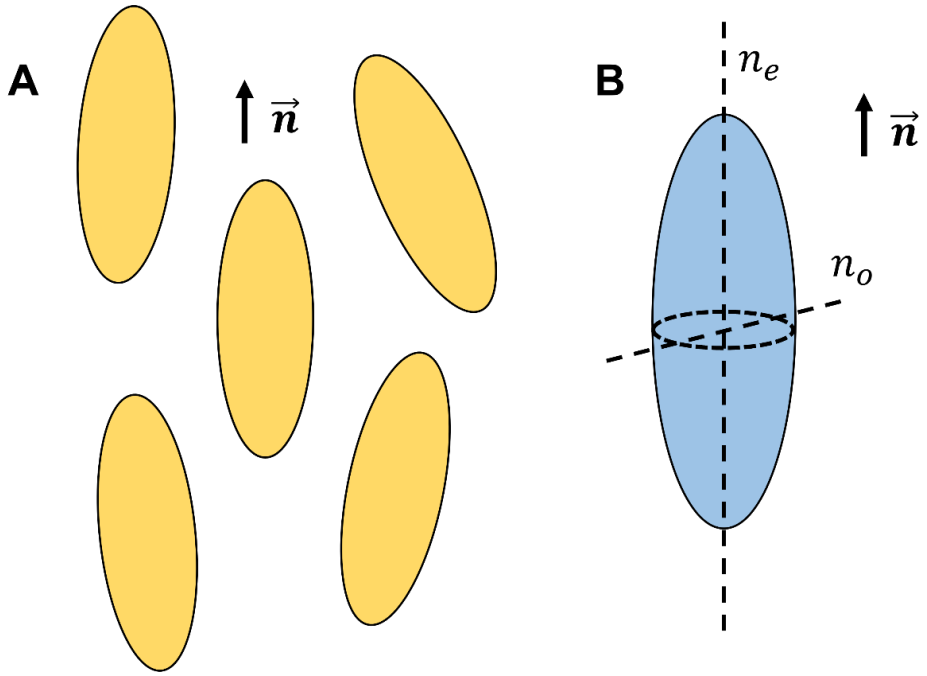

Figure 2.9. (A) A schematic to demonstrate the orientation of mesogens (yellow rods) in a nematic liquid crystalline phase, with the average orientation represented by the director, $\vec{n}$. (B) The indicatrix of the optical properties of this nematic phase, with the ordinary and extraordinary refractive indices annotated, n_o and n_e, respectively. The extraordinary refractive index is aligned along the director of the material, whilst the ordinary refractive index is orthogonal to the extraordinary refractive index.

For the liquid crystals relevant to this thesis, an anisotropic phase will have a greater extraordinary refractive index, such that $n_e > n_o$. The difference between these refractive indices is known as the birefringence, Δn, and therefore takes a positive

value for the materials used in this work. The relation for the birefringence is shown in Equation 2-10 below. (1)

$$\Delta n = n_e - n_o \qquad \textit{Equation 2-10}$$

Another optical property of an anisotropic material is the average refractive index, n_{av}, which is the geometrical average of the ordinary and extraordinary refractive indices and has been related by Vuks (38). This equation is given in Equation 2-11 below.

$$n_{av} = \sqrt{\frac{({n_e}^2 + 2{n_o}^2)}{3}} \qquad \textit{Equation 2-11}$$

Indeed, the refractive indices of any material are temperature-dependent, whether driven by density changes or otherwise. For liquid crystalline materials, particularly of low molar mass, a unique behaviour with temperature is observed. Figure 2.10 shows an example of the behaviour of the refractive indices of a nematic liquid crystal, known as 5CB, as it undergoes an increase in temperature. Whilst the material is in the nematic phase, we clearly observe a large decrease in the extraordinary index and a small increase in the ordinary index. The average refractive index also decreases throughout the temperature increase of the nematic phase. At the cusp of the phase transition, we observe a discontinuous change in the refractive indices and only a single refractive index, n_{iso}, above the transition. This transition is at ~ 308 K and is indicated with a dashed line in Figure 2.10.

The birefringence of the nematic 5CB (Equation 2-10) will decrease with an increasing temperature, until the nematic-to-isotropic transition at which the birefringence discontinuously reduces to zero. This behaviour is attributed to the reduction in the order parameter (previously shown in Figure 2.5), and allows the birefringence to be a measure of the order parameter, $\langle P_2 \rangle$. (23)

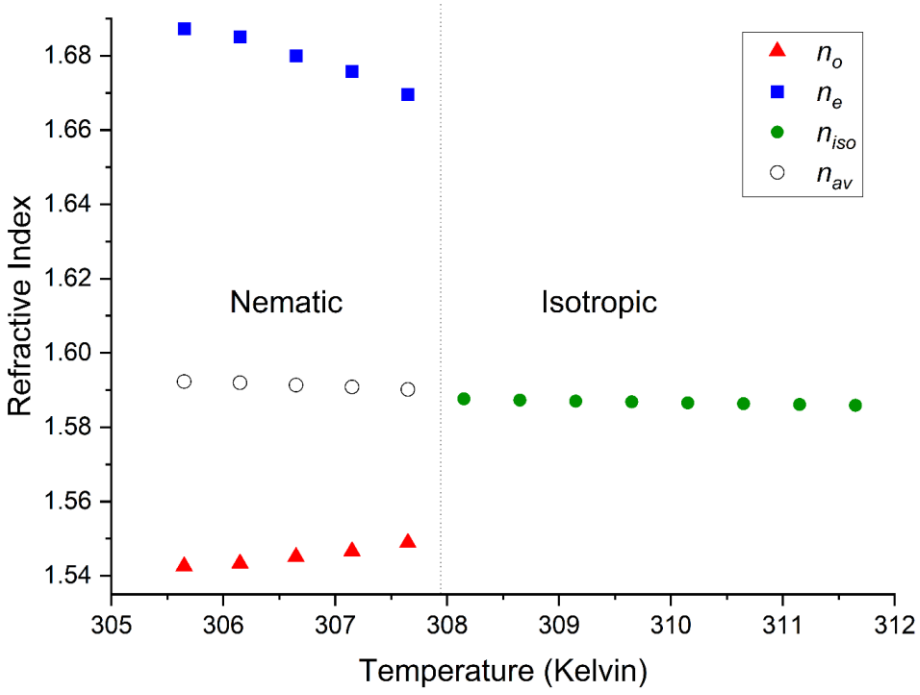

Figure 2.10. The refractive indices of a low molar mass liquid crystal (5CB) during a nematic-to-isotropic transition. In the nematic phase, the ordinary (n_o – red triangles) and extraordinary (n_e – blue squares) refractive indices are directly measured and, according to Equation 2-11, can be used to measure the average refractive index (n_{av} – empty circles). In the isotropic phase, solely the isotropic refractive index can be measured (n_{iso} – green circles). A dashed line has been added at the nematic-to-isotropic transition temperature (~ 308K) as a guide for the eye.

This section has provided a background on the relevant optical properties to this thesis; however, the anisotropic optical properties of liquid crystals have been well established previously and further background information can be accessed in textbooks (1, 26, 39).

2.6 Polymeric Networks: Measuring The Modulus

So far, we have predominantly introduced background relevant to liquid crystals and liquid crystalline materials. We shall now briefly introduce some polymer theory which shall be relevant to the Liquid Crystalline Elastomers that are used within this work. Before we outline some of the key principles, a good background of polymeric materials and their thermal characteristics can be accessed in a number of textbooks (18, 40, 41).

When investigating amorphous polymeric materials, a glass transition can be readily seen by changes in the material behaviour. In the schematic below, the

moduli and the loss tangent of an LCE are shown for a limited temperature range over the glass transition.

The loss modulus describes the viscous behaviour of the material, whereas the storage modulus quantifies how solid the material is. The loss tangent, also known as $\tan \delta$, is the ratio of the loss modulus over the storage modulus. The magnitudes of the loss modulus and the loss tangent are used to quantify the energy dissipation of a material, with good dissipation evidenced by a greater loss modulus than storage modulus, and an accordingly high loss tangent. Clearly, the greatest dissipation is observed in the leathery region, in which the glass transition occurs. With DMTA, the glass transition temperature is generally measured using the peak in the loss tangent or the peak in the loss modulus. These methodologies shall be further outlined and compared in Chapter 4. (18, 41)

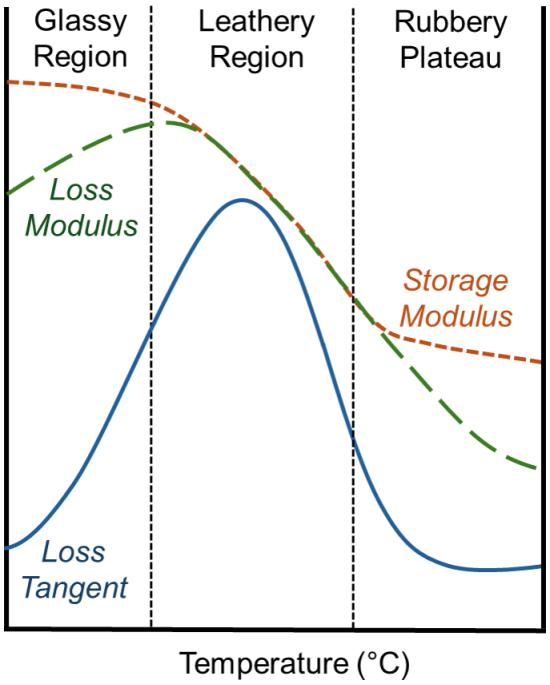

Figure 2.11. A schematic of the loss modulus (large green dashes) and the storage modulus (small orange dashes) of a polymeric network, such as a Liquid Crystalline Elastomer (LCE). The loss tangent, also known as $\tan \delta$ (blue curve), is the ratio of the moduli. This schematic is based on the author's results for Liquid Crystalline Elastomers using Dynamic Mechanical Thermal Analysis, and also using annotated diagrams in the following textbooks (18, 40).

2.7 Conclusion

In this chapter, we have reviewed the background science of liquid crystalline materials and have outlined the key principles to this thesis; the construction of

Liquid Crystalline Elastomers (LCEs), the phases and templates of LCEs, the material order parameters, the anisotropic refractive indices, the transition temperatures, and the moduli of polymeric networks. The background provided in this chapter shall be relevant throughout this thesis.

It is important to reiterate that the background provided in this chapter has been briefly given, since the relevant science is well established and well described elsewhere. The next chapter will build upon these principles by supplying the experimental methods used in this work. This includes the fabrication process of LCEs and the characterization of the various material properties.

2.8 References

1. Collings, P.J. and Goodby, J.W. *Introduction to Liquid Crystals : Chemistry and Physics, Second Edition.* Milton, UNITED KINGDOM: Taylor & Francis Group, 2019.
2. Vertogen, G. and de Jeu, W.H. *Thermotropic Liquid Crystals, Fundamentals.* Berlin: Springer-Verlag, 1988.
3. Ujiie, S. and Kato, T. Design and Synthesis of Side-Chain Liquid Crystal Polymers. In: J. W. Goodby, P. J. Collings, T. Kato, C. Tschierske, H. F. Gleeson and P. Raynes eds. *Handbook of Liquid Crystals*. 2014, pp.1-34.
4. Ujiie, S. and Orihara, H. Structure and Properties of Side Group Thermotropic Liquid Crystal Polymers. In: J. W. Goodby, P. J. Collings, T. Kato, C. Tschierske, H. F. Gleeson and P. Raynes eds. *Handbook of Liquid Crystals*. 2014, pp.1-23.
5. Finkelmann, H., Kock, H.-J. and Rehage, G. Investigations on liquid crystalline polysiloxanes 3. Liquid crystalline elastomers — a new type of liquid crystalline material. *Die Makromolekulare Chemie, Rapid Communications.* 1981, **2**(4), pp.317-322. Available from: https://doi.org/10.1002/marc.1981.030020413
6. Herbert, K.M., Fowler, H.E., McCracken, J.M., Schlafmann, K.R., Koch, J.A. and White, T.J. Synthesis and alignment of liquid crystalline elastomers. *Nature Reviews Materials.* 2021. Available from: https://doi.org/10.1038/s41578-021-00359-z

7. Camacho-Lopez, M., Finkelmann, H., Palffy-Muhoray, P. and Shelley, M. Fast liquid-crystal elastomer swims into the dark. *Nature Materials.* 2004, **3**(5), pp.307-310. Available from: https://doi.org/10.1038/nmat1118
8. Thomsen, D.L., Keller, P., Naciri, J., Pink, R., Jeon, H., Shenoy, D. and Ratna, B.R. Liquid Crystal Elastomers with Mechanical Properties of a Muscle. *Macromolecules.* 2001, **34**(17), pp.5868-5875. Available from: https://doi.org/10.1021/ma001639q
9. He, Q., Wang, Z., Wang, Y., Minori, A., Tolley, M.T. and Cai, S. Electrically controlled liquid crystal elastomer–based soft tubular actuator with multimodal actuation. *Science Advances.* 2019, **5**(10), p.eaax5746. Available from: https://doi.org/doi:10.1126/sciadv.aax5746
10. He, Q., Wang, Z., Song, Z. and Cai, S. Bioinspired Design of Vascular Artificial Muscle. *Advanced Materials Technologies.* 2019, **4**(1), p.1800244. Available from: https://doi.org/10.1002/admt.201800244
11. Feng, W., Broer, D.J. and Liu, D. Oscillating Chiral-Nematic Fingerprints Wipe Away Dust. *Advanced Materials.* 2018, **30**(11), p.1704970. Available from: https://doi.org/10.1002/adma.201704970
12. Mistry, D., Connell, S.D., Mickthwaite, S.L., Morgan, P.B., Clamp, J.H. and Gleeson, H.F. Coincident molecular auxeticity and negative order parameter in a liquid crystal elastomer. *Nature Communications.* 2018, **9**(1), p.5095. Available from: https://doi.org/10.1038/s41467-018-07587-y
13. Cooper, E.J., Reynolds, M., Raistrick, T., Berrow, S.R., Jull, E.I.L., Reshetnyak, V., Mistry, D. and Gleeson, H.F. Controlling the Optical Properties of Transparent Auxetic Liquid Crystal Elastomers. *Macromolecules.* 2024, **57**(5), pp.2030-2038. Available from: https://doi.org/10.1021/acs.macromol.3c02226
14. Jull, E.I.L., Mandle, R.J., Raistrick, T., Zhang, Z., Hine, P.J. and Gleeson, H.F. Toward In Silico Design of Highly Tunable Liquid Crystal Elastomers. *Macromolecules.* 2022, **55**(11), pp.4320-4330. Available from: https://doi.org/10.1021/acs.macromol.2c00587
15. Warner, M. and Terentjev, E.M. *Liquid crystal elastomers.* Oxford: Clarendon Press, 2003.

16. Disch, S., Schmidt, C., and Finkelmann, H. Nematic elastomers beyond the critical point. *Macromolecular Rapid Communications.* 1994, **15**, pp.303-310. Available from: https://doi.org/10.1002/marc.1994.030150402
17. Selinger, J.V., Jeon, H.G. and Ratna, B.R. Isotropic-Nematic Transition in Liquid-Crystalline Elastomers. *Physical Review Letters.* 2002, **89**(22), p.225701. Available from: https://doi.org/10.1103/PhysRevLett.89.225701
18. Menczel, J.D., Judovits, L., Prime, R.B., Bair, H.E., Reading, M. and Swier, S. Differential Scanning Calorimetry (DSC). In: *Thermal Analysis of Polymers*. 2009, pp.7-239.
19. Agra-Kooijman, D.M. and Kumar, S. X-Ray Scattering Investigations of Liquid Crystals. In: J. W. Goodby, P. J. Collings, T. Kato, C. Tschierske, H. F. Gleeson and P. Raynes eds. *Handbook of Liquid Crystals*. Second ed., 2014, pp.1-38.
20. Sims, M.T., Abbott, L.C., Richardson, R.M., Goodby, J.W. and Moore, J.N. Considerations in the determination of orientational order parameters from X-ray scattering experiments. *Liquid Crystals.* 2019, **46**(1), pp.11-24. Available from: https://doi.org/10.1080/02678292.2018.1455227
21. Sanchez-Castillo, A., Osipov, M.A. and Giesselmann, F. Orientational order parameters in liquid crystals: A comparative study of x-ray diffraction and polarized Raman spectroscopy results. *Physical Review E.* 2010, **81**(2), p.021707. Available from: https://doi.org/10.1103/PhysRevE.81.021707
22. Vij, J.K. Infrared and Raman Spectroscopy of Liquid Crystals. In: J. W. Goodby, P. J. Collings, T. Kato, C. Tschierske, H. F. Gleeson and P. Raynes eds. *Handbook of Liquid Crystals*. 2014, pp.1-44.
23. Gleeson, H.F., Southern, C.D., Brimicombe, P.D., Goodby, J.W. and Görtz, V. Optical measurements of orientational order in uniaxial and biaxial nematic liquid crystals. *Liquid Crystals.* 2010, **37**(6-7), pp.949-959. Available from: https://doi.org/10.1080/02678292.2010.488818
24. Haller, I. Thermodynamic and static properties of liquid crystals. *Progress in Solid State Chemistry.* 1975, **10**, pp.103-118. Available from: https://doi.org/10.1016/0079-6786(75)90008-4
25. Zannoni, C. Order Parameters and Orientational Distributions in Liquid Crystals. In: Samori, B. and Thulstrup, E.W. eds. *Polarized Spectroscopy of Ordered Systems*. Dordrecht: Springer Netherlands, 1988, pp.57-83.

26. Pelzl, G. Optical Properties of Nematic Liquid Crystals. In: J. W. Goodby, P. J. Collings, T. Kato, C. Tschierske, H. F. Gleeson and P. Raynes eds. *Handbook of Liquid Crystals*. 2014, pp.1-20.

27. Bragg, W.H. *X-rays and Crystal Structure.* London: G. Bell and Sons, Ltd, 1924.

28. Kratky, O. Zum Deformationsmechanismus der Faserstoffe, I. *Kolloid-Zeitschrift.* 1933, **64**(2), pp.213-222. Available from: https://doi.org/10.1007/BF01434162

29. Davidson, P., Petermann, D. and Levelut, A.M. The Measurement of the Nematic Order Parameter by X-ray Scattering Reconsidered. *Journal de Physique II.* 1995, **5**(1), pp.113-131. Available from: https://doi.org/10.1051/jp2:1995117

30. Zhang, Z. and Gleeson, H.F. Understanding liquid crystal order parameters deduced from different vibrations in polarised Raman spectroscopy. *Liquid Crystals.* 2019, **46**(2), pp.219-233. Available from: https://doi.org/10.1080/02678292.2018.1485980

31. Southern, C.D. and Gleeson, H.F. Using the full Raman depolarisation in the determination of the order parameters in liquid crystal systems. *The European Physical Journal E.* 2007, **24**(2), pp.119-127. Available from: https://doi.org/10.1140/epje/i2007-10223-3

32. Berrow, S.R., Mandle, R.J., Raistrick, T., Reynolds, M. and Gleeson, H.F. Toward Monodomain Nematic Liquid Crystal Elastomers of Arbitrary Thickness through PET-RAFT Polymerization. *Macromolecules.* 2024, **57**(11), pp.5218-5229. Available from: https://doi.org/10.1021/acs.macromol.4c00245

33. Berrow, S.R., Raistrick, T., Mandle, R.J. and Gleeson, H.F. Structure–Property Relationships in Auxetic Liquid Crystal Elastomers—The Effect of Spacer Length. *Polymers.* 2024, **16**(14), p.1957. Available from: https://www.mdpi.com/2073-4360/16/14/1957

34. Raistrick, T., Mandle, R.J., Zhang, Z., Tipping, P.J. and Gleeson, H.F. Order-disorder behavior in the ferroelectric nematic phase investigated via Raman spectroscopy. *Physical Review E.* 2024, **110**(4), p.044702. Available from: https://doi.org/10.1103/PhysRevE.110.044702

35. Raistrick, T., Zhang, Z., Mistry, D., Mattsson, J. and Gleeson, H.F. Understanding the physics of the auxetic response in a liquid crystal elastomer. *Physical Review Research.* 2021, **3**(2), p.023191. Available from: https://doi.org/10.1103/PhysRevResearch.3.023191

36. Wang, Z., Raistrick, T., Street, A., Reynolds, M., Liu, Y. and Gleeson, H.F. Direct Observation of Biaxial Nematic Order in Auxetic Liquid Crystal Elastomers. *Materials.* 2022, **16**(1). Available from: https://doi.org/10.3390/ma16010393

37. Zhang, Z., Panov, V.P., Nagaraj, M., Mandle, R.J., Goodby, J.W., Luckhurst, G.R., Jones, J.C. and Gleeson, H.F. Raman scattering studies of order parameters in liquid crystalline dimers exhibiting the nematic and twist-bend nematic phases. *Journal of Materials Chemistry C.* 2015, **3**(38), pp.10007-10016. Available from: https://doi.org/10.1039/C5TC02174J

38. Vuks, M.F. Determination of the optical anisotropy of aromatic molecules from the double refraction of crystals. *Optics and Spectroscopy.* 1966, **20**.

39. Dunmur, D. Optical Properties of Liquid Crystals. In: J. W. Goodby, P. J. Collings, T. Kato, C. Tschierske, H. F. Gleeson and P. Raynes eds. *Handbook of Liquid Crystals*. 2014, pp.1-26.

40. Collins, E.A., Bareš, J. and Billmeyer, F.W. *Experiments in polymer science.* New York: Wiley, 1973.

41. Duncan, J. Principles and Applications of Mechanical Thermal Analysis. In: *Principles and Applications of Thermal Analysis*. 2008, pp.119-163.

Chapter 3 Experimental Techniques

A portion of the work in this chapter has previously been published in (1):

Emily J. Cooper, *et al*. "*Controlling the Optical Properties of Transparent Auxetic Liquid Crystal Elastomers"*. Macromolecules, 2024, **57**(5), 2030-2038.

Any experimental work that was not performed by the author, Emily Jane Cooper, will be stated in the text or the figure caption.

3.1 Introduction

In this thesis, we will investigate monodomain nematic, polydomain nematic, and isotopic LCEs and we will refer to these as different 'templates' of the material. This terminology reflects that each of these 'templates' has distinct ordering; as aforementioned in Section 2.2, the monodomain nematic has a director which acts across the whole material (a macroscopic director), the polydomain nematic has regions aligned along some director with a random orientation of each region across the material (no macroscopic director), and the isotopic has a random arrangement of the mesogens (no director). The main purpose of this terminology is therefore to distinguish between the polydomain nematic and monodomain nematic materials, since these templates are of the same phase.

Throughout literature, there are a plethora of alignment methods available for nematic LCEs which includes the use of mechanical alignment, surface layers, and the application of a field (electric, magnetic); the various alignment methodologies available has previously been reviewed by Herbert *et al.* (2). The ideal alignment technique for an LCE is contingent on the chemistry and synthesis used; for example, mechanical alignment requires a partial polymerization of the material, so that the material can be stretched and polymerized again to lock order into the system (2, 3). In this work, the alignment of monodomain nematic LCEs will be promoted using surface alignment layers and this methodology will be discussed.

The following chapter will detail all the experimental methods that are used within this thesis to characterise the formation of monodomain nematic, polydomain nematic, and isotropic LCE templates. Techniques that are used in this work will investigate the thermal, physical, and optical properties of the networks and the

results for each are given in later Chapters (Chapters 4 - 7) within the context of literature.

3.2 The Synthesis of LCEs

The following methodology used for templating the LCEs can produce good quality isotropic, polydomain nematic, and planar aligned monodomain nematic materials; with slight adaptions to this methodology, homeotropically aligned monodomain nematic LCEs (4), and smectic LCEs (5) can also be produced.

3.2.1 Composition

The LCEs used within this thesis are based on a composition of LCE that has been previously reported (1, 4-6). All the polymerized LCEs in this work comprise of mesogenic material (side group, crosslinker) and non-mesogenic material (side group, photoinitiator); a schematic of the network structure is shown in Figure 3.1A with the molecular structures of the components of the LCEs shown in Figure 3.1B. The non-mesogenic materials are the side group 2-ethylhexyl acrylate (EHA), and the photoinitiator methyl benzoylformate (MBF). The mesogenic material used includes the diacrylate crosslinker, 1,4-bis-[4-(6-acryloyloxyhexyloxy)benzoyloxy]-2-methylbenzene (RM82), and a monofunctional side group, 6-(4-cyano-biphenyl-4'-yloxy)hexyl acrylate (A6OCB).

An additional non-reactive mesogenic material, 4-cyano-4'-hexoxybiphenyl (6OCB), is included in the precursor mixture to extend the nematic phase prior to polymerisation, allowing high-quality, monodomain films to be produced; the 6OCB is washed from the final LCE. The RM82, A6OCB and 6OCB were supplied by Synthon Chemicals GmbH© (Bitterfeld-Wolfen, Germany), the EHA and MBF were supplied by Sigma-Aldrich© (Gillingham, U.K.).

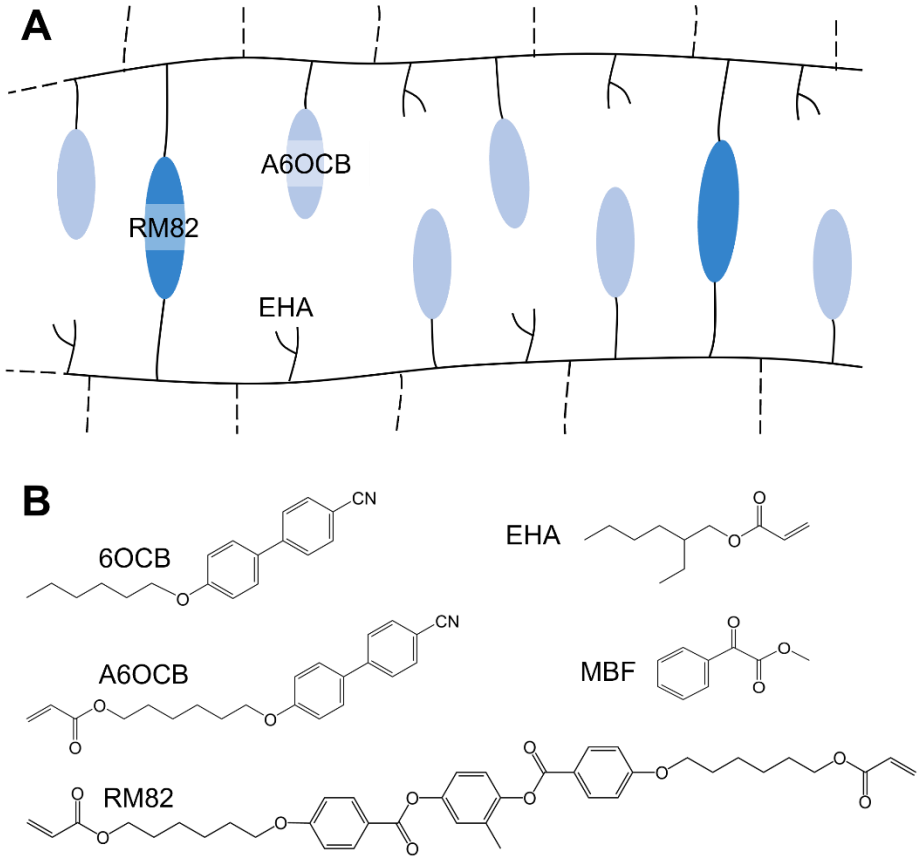

Figure 3.1. (A) A schematic of the acrylate-based side chain Liquid Crystalline Elastomer (LCE) family used in this work. The polyacrylate backbone is shown as a black, continuous line, the side-groups are non-mesogenic (EHA) and mesogenic (A6OCB), while the crosslinker is the diacrylate reactive mesogen (RM82). (B) The chemical structures of the components included in the LCE precursor mixture, with the additional mesogen, 6OCB, also shown. This figure has been published by Cooper et al. (1).

In this work, the composition of the LCEs was altered through the quantity of EHA added to the precursor mixture, thereby varying the mole percent (mol%) of the total mesogenic materials, RM82, A6OCB and 6OCB (the latter is washed from the final LCE). Specifically, the mol% ratio of RM82:A6OCB in the polymerized LCE remained constant (1:7), and the total mesogenic content for the LCEs was varied between 51 and 84 mol%.

We use a nomenclature that describes the nematic LCEs by their mol% of mesogenic content, so a nematic LCE with 62 mol% mesogenic content is referred to as nLCE-62 and an isotropic material of the same composition is referred to as iLCE-62. For reference, nLCE-62 was the starting material previously studied within this acrylate LCE family (1, 4-7).

Table 3-1. The compositions of the precursor mixtures and the polymerized LCEs used in this thesis. The mol% for each component in the precursor mixture and polymerized LCE changes due to the wash out of 6OCB. The compositions with an asterisk (*) indicates that these form phase separated nematic LCEs. The polymerized LCEs with mesogenic contents of 75 mol% and 84 mol% were synthesised by Matthew Reynolds. The polymerized LCE of 62 mol% mesogenic content was the starting material for this composition series; samples of this composition used within this work were also synthesised by Matthew Reynolds and Ethan Jull and credit will be given accordingly. A polymerized LCE of 80 mol% mesogenic content was not formed; only the precursor mixture for this composition was examined.

Mesogenic content of Polymerized LCE (± 1 mol%)	Composition									
	RM82		A6OCB		6OCB		EHA		MBF	
	Precursor	LCE	Precursor	LCE	Precursor	LCE	Precursor	LCE	Precursor	LCE
51*	3	6	22	44	50	Removed (during wash)	23	46	1	3
53*	3	7	23	47	51		22	44	1	3
56	3	7	23	49	52		20	41	1	3
59	3	8	24	52	54		17	37	1	3
62	4	8	24	54	55		16	35	1	3
64	4	8	25	56	56		15	33	2	3
66	4	8	25	58	56		13	30	2	4
67	4	8	25	59	57		12	29	2	4
72	4	9	26	63	58		10	25	2	4
75	4	9	27	65	59		9	21	2	4
80	4	10	27	70	61		6	16	2	4
84	4	11	28	73	62		5	12	2	4

A summary of all LCE compositions that are used in this thesis are shown in Table 3-1. The mol% of both the precursor mixture and the polymerized LCE is indicated, to reflect that the mol% of each component will change after the 6OCB is removed. The range of compositions shown in Table 3-1 reflects that there are formulation limitations to these materials for these investigations; the lower limit is dictated by phase separation, which was observed in nLCE-51 and nLCE-53, and the upper limit is dictated by the glass transition temperatures of the polymerized LCEs approaching room temperature. The glass transition temperatures results will be given later in Chapter 4.

The phase separation that is observed in LCEs of low mesogenic content is shown in Figure 3.2 and is compared to a well-formed monodomain nematic LCE (nLCE-

59). Clearly, nLCE-53 and nLCE-51 show different degrees of phase separation, with the lower mesogenic content LCE (nLCE-51) showing the greatest phase separation. The clear areas of nLCE-51 and nLCE-53 in Figure 3.2 are regions of nematic LCE. Investigations into the limitations of the monodomain nematic template are given in Sections 4.3 and 5.2.1.

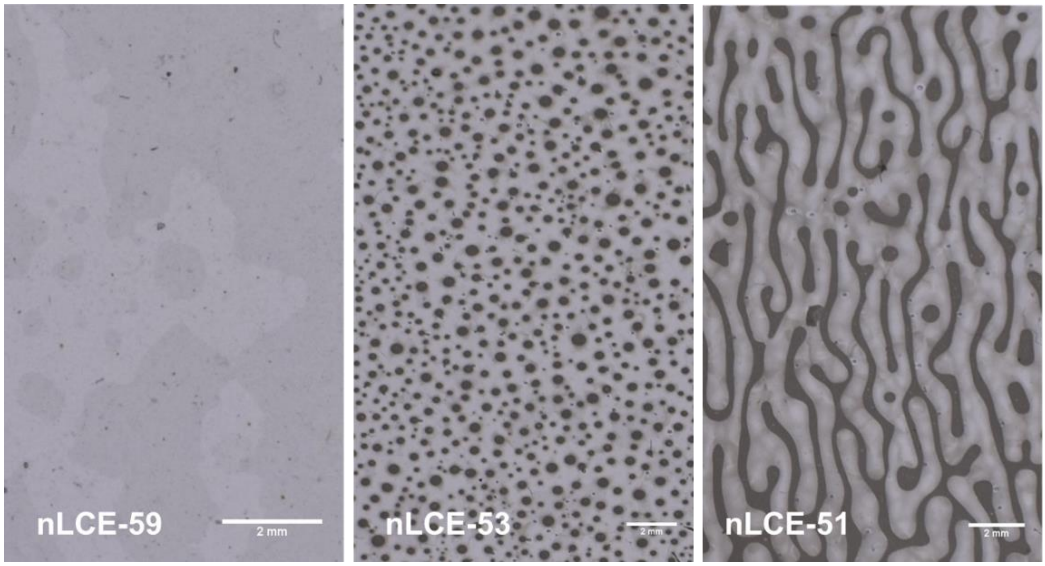

Figure 3.2. Images of the nematic LCEs with compositions of 59 mol%, 53 mol% and 51 mol% mesogenic content from left to right. The left-most image shows a uniform monodomain nematic LCE with excellent alignment and no phase separation, whereas the two samples on the right display different degrees of phase separation. The scale bars are all 2 mm in length. This figure is included in a publication by Cooper et al. (1).

3.2.2 Fabrication

In this work, moulds are required to fabricate the LCEs. The moulds are assembled using a 100 µm thick strip of Melinex® as a spacer between a glass substrate and a 250 µm Melinex® substrate, both coated with poly(vinyl alcohol) and rubbed. A schematic of this assembly can be seen in Figure 3.3. To make an LCE film, the precursor LCE mixture must first be made, starting with mixing the mesogenic materials for 5 minutes at 120°C. Once cooled to approximately 40°C, MBF and EHA are added *via* a pipette and the mixture is stirred for a further 2 minutes. The mixture is then filled into prepared moulds at 40°C, using the capillary effect. A diagram of this method is shown in Figure 3.3.

To achieve nematic LCEs, the filled mould then rests in the nematic phase at room temperature for 20 minutes to ensure good alignment prior to being irradiated with

a 2.5 mW/cm^2 UV light source for 2 hours. For isotropic LCEs, the material is instead held at an elevated temperature in the isotropic phase and then irradiated with UV light for two hours. The LCE is then removed from the mould and washed overnight in a methanol and dichloromethane mixture to remove the 6OCB. Following the overnight wash, the elastomer is then left at ambient conditions to dry by evaporation of the washing solvents.

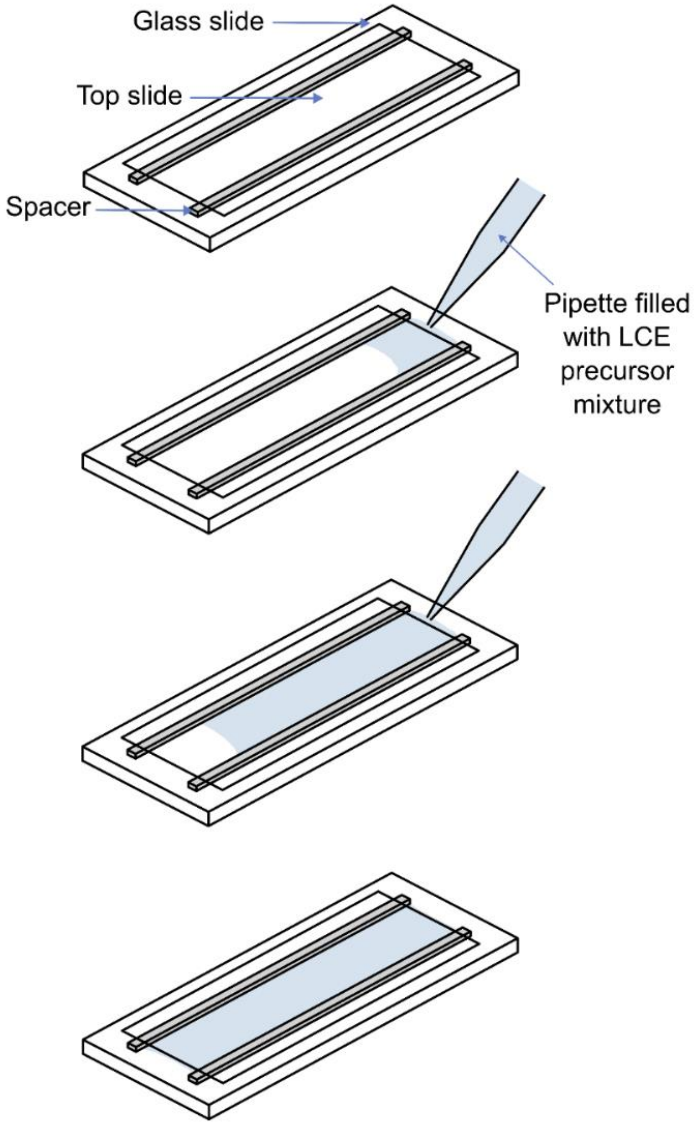

Figure 3.3. A schematic to show the assembled moulds consisting of the glass slide, spacers and the Melinex® slide on top. The top and bottom slides are coated with poly(vinyl alcohol) and rubbed. The precursor LCE mixture is added into the mould using a pipette and fills the mould via the capillary effect.

3.3 Thermal and Mechanical Analysis Techniques

In this section, we will describe the thermal and mechanical techniques that will be used in this thesis. These techniques will be described together since the mechanical properties are predominantly investigated with temperature.

The techniques of Differential Scanning Calorimetry (DSC) and Dynamic Mechanical Thermal Analysis (DMTA) will be outlined first in brief. Using both of these techniques, we can measure the glass transition temperatures of the polymerized LCEs. Each technique also offers additional insight; the nematic-to-isotropic transition temperatures of the precursor LCE mixtures can be measured with DSC, and the dissipative capabilities of the polymerized LCEs can be measured using DMTA. These techniques are widely known and used within the polymer community and a good overview of these techniques can be accessed in the following textbooks (8-11).

Then, we will discuss an in-house technique, known as the Microscope Elastomer Stress Strain Enclosure (MESSE), which enables the auxetic threshold of the monodomain nematic LCEs to be measured. This technique has been shown as effective in previous literature (4-6, 12). Lastly, we will demonstrate how the thermal shape change properties of the materials can be quantified using optical microscopy.

3.3.1 Differential Scanning Calorimetry (DSC)

In this work, Differential Scanning Calorimetry (DSC) was used to measure the transition temperatures of the precursor LCE mixtures and the polymerized LCEs. This technique measures the heat flow through a pan loaded with a sample, with respect to an empty pan. As aforementioned, a good description of this technique can be found in textbooks (9, 10, 13).

In this work, small quantities of material (5-10 mg) were inserted into the base of Tzero Aluminium pans and sealed with Tzero Aluminium lids. The filled pan and a reference pan were loaded into a TA Instruments™ Q20 with a RCS90 cooling system and measured for three cycles with a heating/cooling rate of 10˚C/minute. The nematic-to-isotropic transition temperature, T_{NI}, of the unpolymerized precursor mixtures was measured as the onset of the transition peak on cooling with

run cycles between 100°C and -60°C. The glass transition temperature, T_g, of the polymerized LCEs was determined from runs between 250°C and -40°C and measured as the inflection on cooling. Examples of both of these measurements are shown in Figure 3.4.

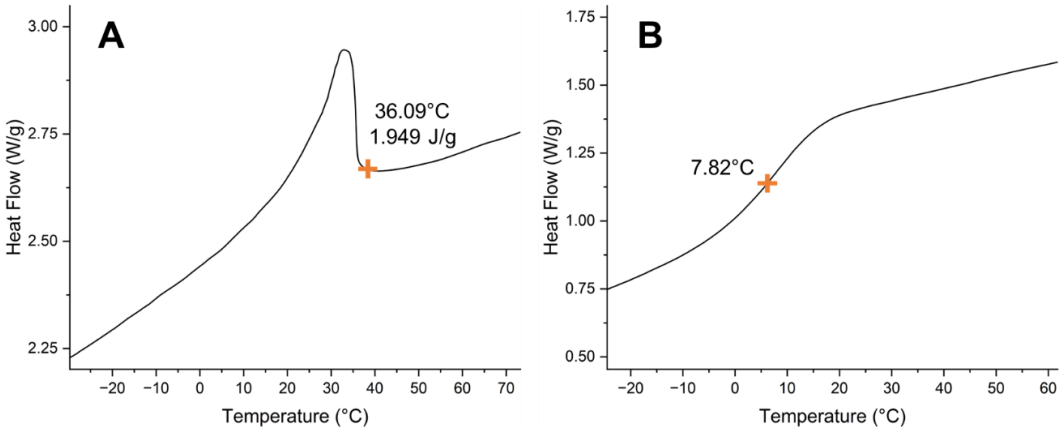

Figure 3.4. Examples of the DSC heat flow for measuring (A) the nematic-to-isotropic transition temperature (T_{NI}) of the unpolymerized precursor mixtures using the onset of the transition peak on cooling, and (B) the glass transition temperature (T_g) of the polymerized LCEs using the inflection on cooling. The approximate positions of the transition temperatures are indicated on the traces with orange crosses.

Clearly, Figure 3.4 demonstrates that DSC can measure a transition temperature to a precision of 0.01°C. When considering an average transition temperature measured between cycles, DSC can measure to a precision ~ 0.1°C. However, we must use an error that can account for the difference observed in the average transition temperatures between various materials of the same composition. Therefore, an error of ± 0.6°C is used, which was determined from the standard deviation of multiple average transition temperatures of the 62 mol% mesogenic content nematic LCE (nLCE-62); this error will be used for all the transition temperatures measured with DSC in this work. This error was calculated using results measured by the author (Emily Cooper), Zhenming Wang, and Stuart Berrow.

3.3.2 Dynamic Mechanical Thermal Analysis (DMTA)

DMTA is a widely used technique in the polymer science field for measuring the moduli of a material. Within this thesis, this technique is used to measure the glass transition temperatures and the moduli of the various compositions and templates of LCEs. As aforementioned, DMTA techniques have been well discussed

previously and further information is recommended in the following textbooks (8, 11).

Appropriate parameters need to be selected to investigate the loss and storage moduli and the ratio between these, known as the loss tangent. Crucially, certain parameters such as the oscillation strain, need to be selected such that the moduli are measured within the linear viscoelastic region (8). Therefore, the parameters used for this technique shall be outlined here.

All LCEs were compared using the same parameters as a control. Samples of 8-12 mm in length and 5 mm in width, were stacked to a thickness of ~ 200 μm and loaded into the film clamps of a TA Instruments™ DMA 850 connected to a liquid nitrogen dewar. Care was taken to ensure that the monodomain nematic LCEs were stacked along the same alignment axis. The samples were investigated using temperature ramps between 50°C to -10°C in 3 cycles at a rate of 2°C/min. The oscillation frequency was selected to be 1 Hz since this is a standard frequency used across literature and should also give a good comparison to the T_g values found with DSC (13). An oscillation strain of 0.07% was chosen since this was within the linear viscoelastic regime for the LCE; the oscillation strain for a monodomain nematic LCE is shown in Figure 3.5 at various temperatures.

Lastly, a temperature error of ± 1°C is used for the glass transition temperatures of all materials, which was determined using the standard deviation of results for monodomain nematic materials of the same composition (nLCE-62). This error was calculated based on transition temperatures that were measured by the author (Emily Cooper) and Aidan Street.

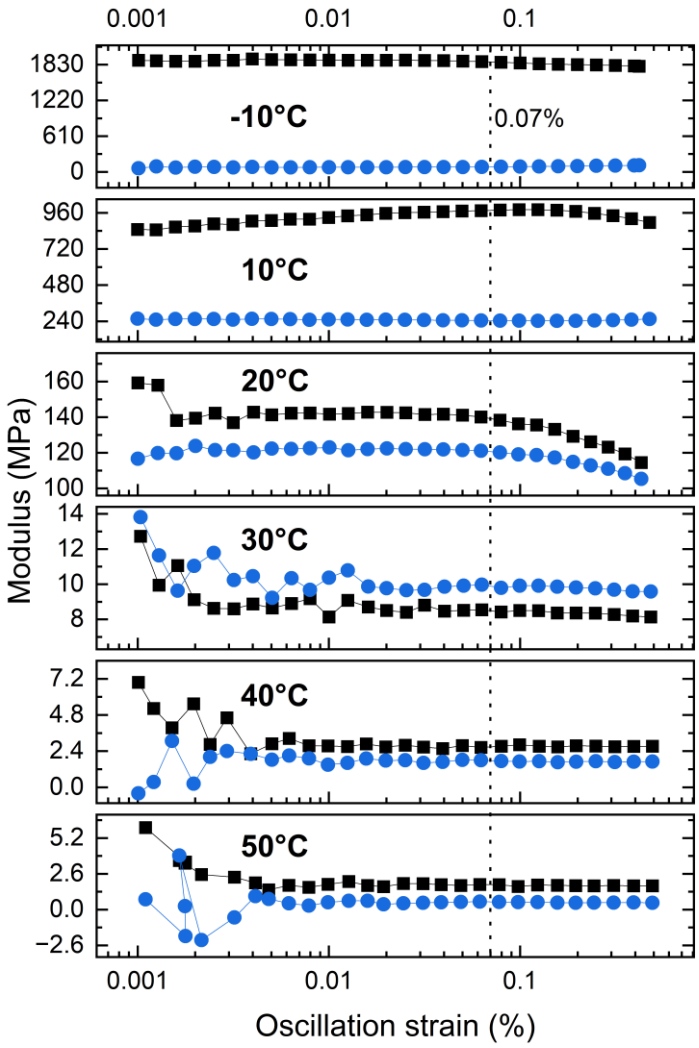

Figure 3.5. The storage (black squares) and loss (blue circles) modulus of a monodomain nematic LCE of 66 mol% mesogenic content for a varied oscillation strain at different temperatures. A dashed line is added at 0.07% oscillation strain as a guide for the eye, to show this parameter is suitable for the temperatures investigated. Note that the loss modulus is only greater than the storage modulus at 30°C.

3.3.3 Microscope Elastomer Stress Strain Enclosure (MESSE)

The Microscope Elastomer Stress Strain Enclosure (MESSE) is in-house equipment that is designed to investigate the auxetic response of the monodomain nematic templated LCEs that are investigated within this thesis. Results using this equipment have previously been reported in literature, which demonstrates that this methodology can effectively measure the auxetic response of these materials (4-6, 12). This equipment was originally designed by Mistry *et al.* (12, 14) to measure the auxetic response of a monodomain nematic material within this family of LCEs. Since then, this technique has been used to measure the auxetic response of other

LCE compositions within this family (4-6). The methodology for this technique can be accessed in each of these previous sources and will be outlined again below.

For this technique, small sample of monodomain nematic LCE were prepared with 2 mm width, 15 mm length, and 100 µm thickness, with the longest axis perpendicular to the director. A schematic of the experimental setup can be seen in Figure 3.6, showing a loaded and clamped LCE in the actuator arms, where the material was carefully loaded into the clamps to be flat but not strained. In this method, the actuator arms retreated in steps of 0.5 mm every 600 seconds, to ensure that the sample is sufficiently relaxed between the strain steps.

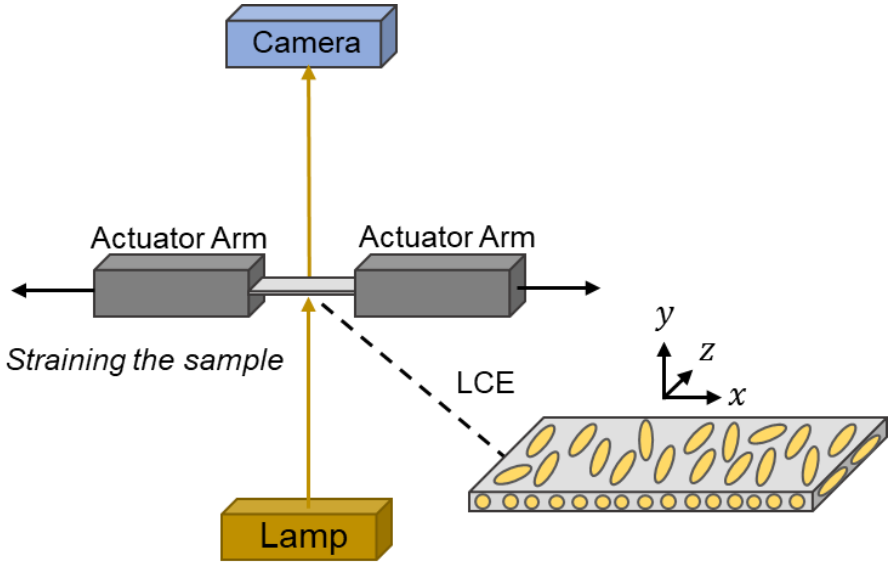

Figure 3.6. The in-house Microscope Elastomer Stress Strain Enclosure (MESSE), which can measure the auxetic response of the monodomain nematic LCEs. The LCEs are loaded and clamped into the actuator arms as shown.

All images were taken at the end of each strain step and the particle tracking was performed using Image J to measure the *x*- and *y*- axis strains of the sample, ε_x and ε_y, respectively. As shown in Figure 3.6, the *x*-axis is the length of the sample and the axis in which the strain is applied, the *y*-axis is the width of the material and is parallel to the director, and the *z*-axis is the thickness. According to Equation 3-1, the strain in the *z*-axis, ε_z, can then be calculated.

$$(\varepsilon_x + 1)(\varepsilon_y + 1)(\varepsilon_z + 1) = 1 \qquad \textit{Equation 3-1}$$

Images taken for the particle tracking are shown in Figure 3.7 for different strain steps. In this example, the strain threshold occurs at $\varepsilon_x \sim 0.49$, and therefore the material is auxetic the latter two images.

Figure 3.7. Images of a monodomain nematic LCE taken using MESSE. In this example, the strain threshold for an auxetic response is at ε_x ~ 0.49, and therefore the material is auxetic in the latter two images (26 and 40 steps). The scale bars are 1mm.

Figure 3.8A shows the applied strain in the *x*-axis against the resultant strain in the thickness axis and demonstrates that an auxetic response occurs at a threshold strain. To calculate the threshold strain for an auxetic response, the Poisson's Ratio relating to the axes of applied strain and the thickness must be calculated ($-\varepsilon_z/\varepsilon_x$). Polynomial fittings can be used to calculate the Poisson's Ratio of the material as in Figure 3.8A, which shows two example polynomial fittings which use 3rd order and 9th order terms. Clearly, the 9th order polynomial fitting gives an improved fitting to the data compared to 3rd order, however both will be demonstrated as effective for measuring the strain threshold.

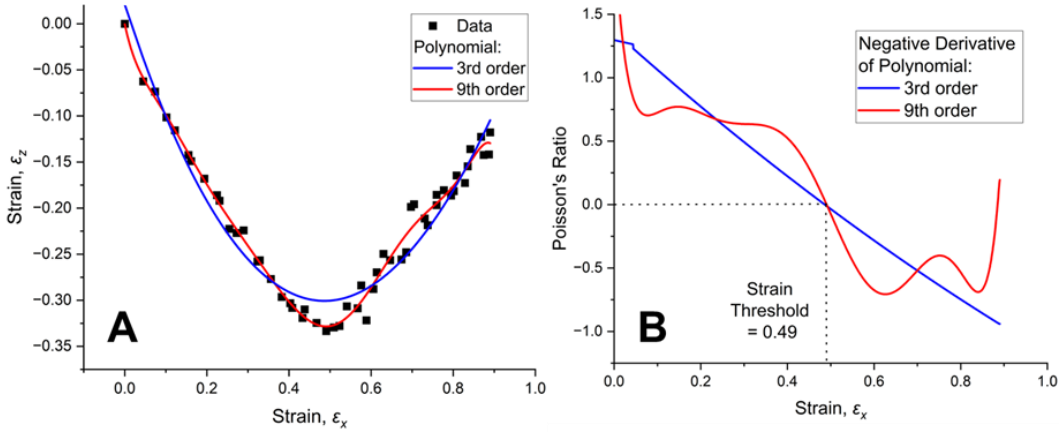

Figure 3.8. (A) A plot of the strain in the x- and z- axes, demonstrating that there is a threshold strain of the auxetic response. Two polynomial fittings have been applied to the experimental data in (A), which are of 3rd order and 9th order. (B) A plot of the Poisson's Ratio in the x-z plane of the material, calculated via a negative of the derivative of the polynomials found in (A). The strain threshold is calculated at the point where the Poisson's Ratio passes through zero in (B), and good agreement is seen between the derivatives of the 3rd and 9th order polynomials. In this example, the strain threshold is at ε_x ~ 0.49.

The negatives of the polynomial derivates, which were found in Figure 3.8A, give the Poisson's Ratio of the material in the x-z plane, as seen in Figure 3.8B. This enables the strain threshold to be measured as the strain in which the Poisson's Ratio is zero; in the example in Figure 3.8, the strain threshold is at $\varepsilon_x \sim 0.49$.

3.3.4 Thermal Shape Change

To investigate the shape change of the LCEs, small samples were placed on a glass slide covered with silicon oil, with the oil preventing any direct contact and sticking between the surfaces. The samples were cut with dimensions perpendicular (L_{perp}) and parallel (L_{para}) to the director for the monodomain nematic LCEs, however since there is no macroscopic director to the polydomain nematic LCEs, the samples were simply cut for orthogonal axes that will be denoted as L_x and L_y. The schematic in Figure 3.9 shows the thermal shape change observed for monodomain nematic LCEs.

The temperature across the sample was controlled using a Linkam THMSE600 control stage connected to a Linkam T95 controller. The hostage was placed on a Leica Microscope and images of the sample were taken every 5°C between room temperature (22°C) and 150°C. The thermal shape change was measured using ImageJ software to monitor the changes of the axes with temperature.

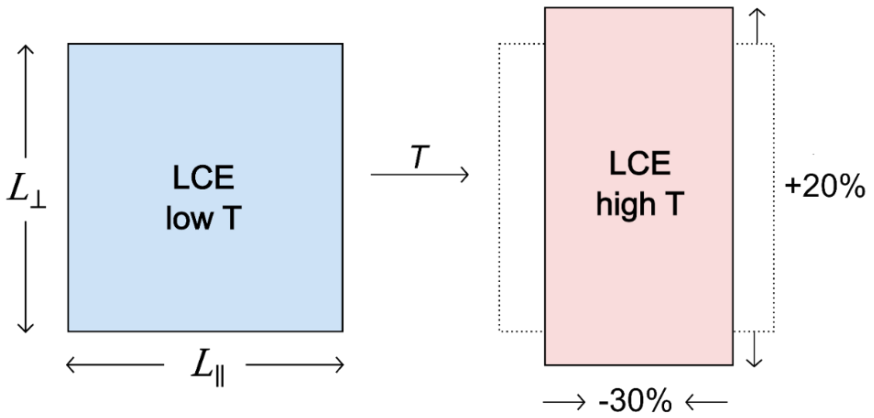

Figure 3.9. The thermal shape change of a monodomain nematic LCE is shown for an increase in temperature. Along the axis parallel to the director, there is an approximate 30% contraction in the length, whereas there is a 20% expansion in length along the axis perpendicular to the director.

3.4 Order Parameter Techniques

3.4.1 Raman Spectroscopy

In this work, Raman Spectroscopy is used to measure the order parameters of the monodomain nematic LCEs and the results are reported in Section 5.2. An overview of the relevant theory for this technique was provided in Section 2.4, so only information on the experimental method shall be addressed here.

A Renishaw™ inVia Raman Microscope with a 532nm solid state laser of 2.5mW power, was used to determine the Raman spectra of the LCE samples in a backscatter geometry. In this work, a 20x objective was used for all monodomain nematic LCEs, except for the phase separated LCEs (as seen in Figure 3.2), where a higher magnification 50x objective was required to ensure that measurements were performed only on the regions with nematic order.

The elastomer samples were placed onto a glass slide and fixed on the rotational stage of the Raman microscope, allowing measurements to be made at 5˚ - 10˚ intervals over a full 360˚ rotation of the sample. Intensity data were recorded with the analyser both parallel and perpendicular to the input light polarization, allowing a depolarization ratio to be calculated; the theory on this can be found in Section 2.4.2. The ~ 1606 cm^{-1} peak, corresponding to the breathing mode of the phenyl group, was selected for analysis as it has previously been shown to satisfy all the requirements for the determination of the order parameters of liquid crystals (15,

16). As discussed previously in Section 2.4.2, the scattering intensities for the parallel and perpendicular polarizations can then be used to determine the order parameters $\langle P_2 \rangle$ and $\langle P_4 \rangle$.

3.4.2 Small-Angle (SAXS) and Wide-Angle (WAXS) X-ray Scattering

Scattering methods such as light scattering and neutron scattering, are commonly used to reveal the structure of various materials. Indeed, scattering techniques have long been employed to identify the existence of long-range ordering and lattice structures of materials. An overview of the key principles of X-ray Scattering were provided in Section 2.4.1. Further information on the X-ray scattering of soft matter and liquid crystalline materials has been widely reported and can be found in the following textbooks (17-19).

In this thesis, just the monodomain nematic and isotropic templated LCEs will be experimentally investigated with X-ray Scattering. However, we will make comparisons to the results obtained by Berrow *et al.* (5), who recently templated similar composition acrylate-based LCEs into a smectic phase *via* the variation of the mesogenic side group spacer length. All the results for X-ray Scattering are reported in Chapter 5: the order parameters are given in Section 5.2.2, and the intermolecular spacings are detailed in Section 5.4.

3.4.2.i Experimental Setup

Small pieces of monodomain nematic and isotropic LCE films (roughly 5 mm x 5 mm and 100 μm in thickness) were mounted using Kapton tape onto a 4x5 holder for solids, with care taken to ensure that the monodomain nematic LCEs were being compared for the same director orientation. To provide a calibration for WAXS and SAXS, small quantities of lanthanum hexaboride (LaB_6) and silver behenate (AgBeh) were secured between pieces of Kapton tape and mounted onto the holder. Both LaB_6 (20) and AgBeh (21, 22) have well documented scattering features within the WAXS and SAXS regimes, respectively, and are widely used and accepted as scattering calibrants. Specifically, these materials are used to calibrate the sample to detector distance.

The filled sample holder was loaded within a vacuum controlled chamber of an Anton Paar™ SAXSPoint 5.0. The setup uses a copper source (1.5418 Å) and the

resultant scattering from the sample was detected using an Eiger2 R 1M at sample detector distances of 0.2 m and 0.053 m for SAXS and WAXS, respectively. All the data was collected with three average frames and a count time of 600 seconds. The monodomain nematic LCEs were investigated for two rotations to provide an insight into the material structure both perpendicular and parallel to the director. A schematic to demonstrate the setup is shown in Figure 3.10 and shows that the use of a beam stop prevents high intensity X-rays directly transmitted to the detector.

Lastly in this investigation, there was no specific temperature regulation across the LCE samples, however the temperature was monitored and measured to be between 28°C and 29°C for all scattering results.

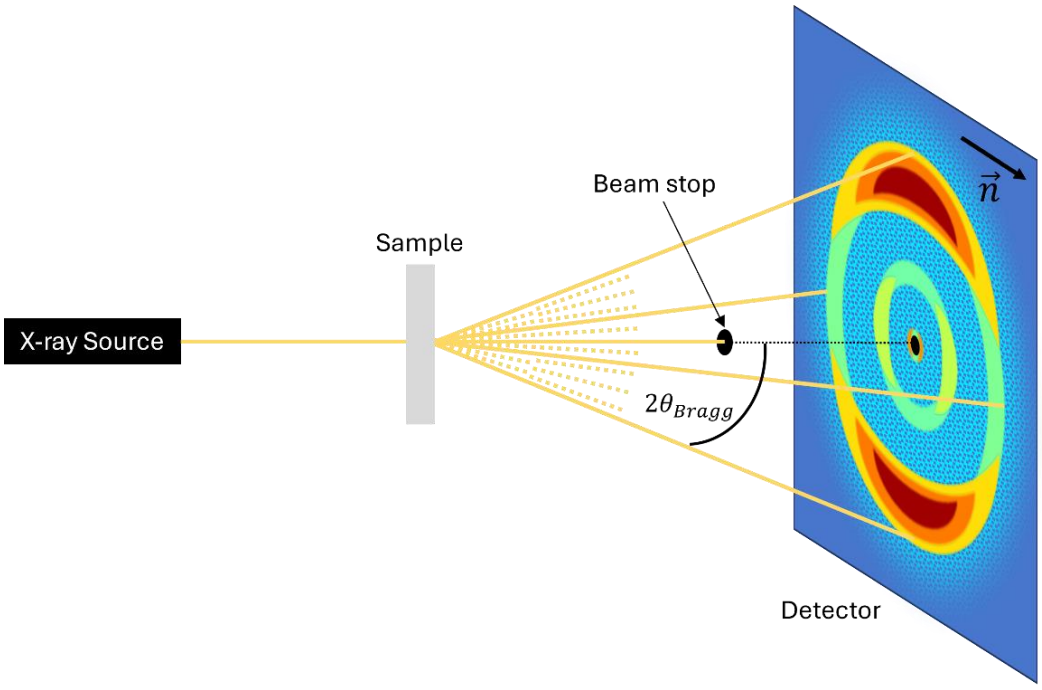

Figure 3.10. A schematic of Wide-Angle X-ray Scattering (WAXS) from an anisotropic sample onto a 2D detector. The director, $\vec{n}$, of the anisotropic sample is indicated on the detector. The scattering satisfies Bragg conditions, and the features appear at $2\theta_{Bragg}$.

The dimensions of a material during X-ray scattering are important, since the thickness will have an impact on the scattering intensity. Therefore, the average thickness of all the LCEs was measured using a micrometer and can be seen in Table 3-2 to vary between ~ 80 µm to ~ 140 µm for LCEs made with 100 µm thick moulds. The error in the average thickness of the material was determined by the standard deviation of the repeats.

A thickness of less than 100 µm is attributable to the shrinkage of the LCE during the wash out stages of the fabrication process, whereas an LCE thickness that is greater than the 100 µm spacers is due to a thicker application of the UVS 91 glue when constructing the mould. The sample thickness is later taken into consideration using a thickness normalised intensity in Section 5.4.2.

Next, we shall discuss how the X-ray Scattering data was analysed for information on the feature position, orientation, and the order parameters of the LCEs.

Table 3-2. The thicknesses of monodomain nematic and isotropic LCEs that were investigated using Wide-Angle and Small-Angle X-ray Scattering. An average thickness across the material is taken and the error in the thickness is calculated from the standard deviation of repeat measurements.

Template	**Mesogenic Content (± 1 mol%)**	**Thickness (± 2 µm)**
Monodomain Nematic	56	144
	62	89
	64	100
	67	115
	72	123
Isotropic	67	84
	72	120

3.4.2.ii Analysis of Features: Position and Orientation

The transformation and analysis of SAXS and WAXS data between real space and reciprocal space was performed using the *SAXSanalysis* program by Anton Paar™. The monodomain nematic template will be used as an example of the methodology, since the scattering of this template is more complex than the isotropic template.

As shown in Figure 3.11, the orientations parallel and perpendicular to the director of the monodomain nematic LCEs were considered during this investigation, to comprehend the complete scattering of the material. To investigate the scattering feature positions in reciprocal space (q, nm^{-1}), the intensity data was reduced as a function of the radial angle, φ, as shown for a monodomain nematic LCE in Figure 3.11. A data reduction of 150 to 200 data points proved to be effective for detecting each of the observable scattering features ($q \sim 1.5$ nm^{-1}, 5 nm^{-1}, 14 nm^{-1}) and to also detect fainter features.

Peak fittings were applied to the measured intensity, $I(\varphi)$, against q (nm^{-1}) to find the centre of each feature, before being converted to a real spacing (Å). The full width half maximum of particular features ($q \sim 1.5$ nm^{-1}) were also measured to provide a correlation length of the material, which will be addressed in Section 5.4.4.

Lastly, the scattering intensity extracted with this methodology was also converted into a thickness normalized intensity, by dividing the raw intensity with the thickness of the materials, which were given in Table 3-2. This was performed to directly compare the scattering irrespective of the sample dimensions.

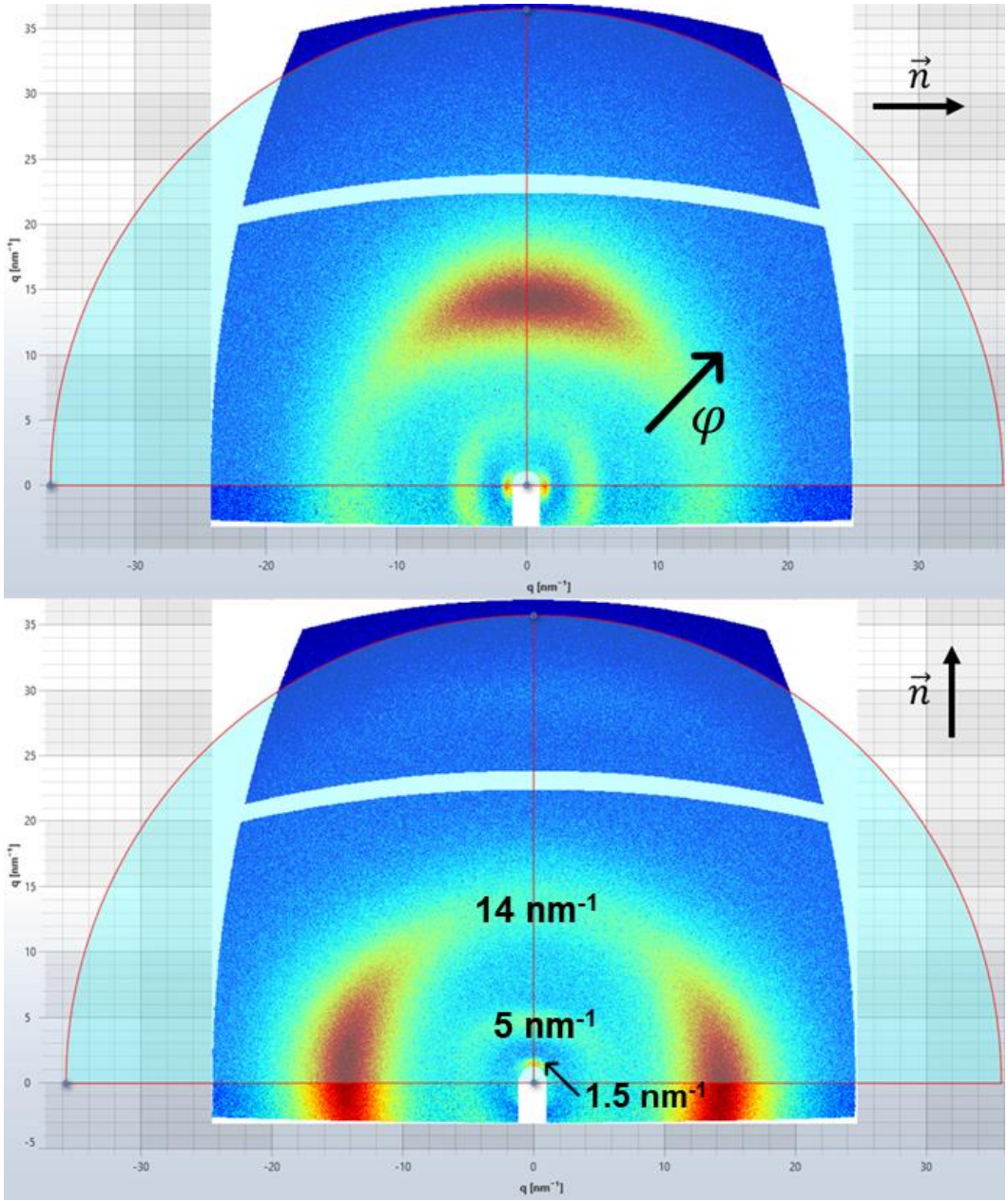

Figure 3.11. An example of the WAXS scattering of a monodomain nematic LCE for two different orientations of the director. The scattering intensity, $I(\varphi)$, is investigated in q (nm^{-1}) along the radial angle, φ (red-outlined light blue mask, in the shape of a 180° cone). The feature positions of the three observable scattering features are also indicated at q ~ 1.5 nm^{-1}, 5 nm^{-1}, 14 nm^{-1}. This was analysed using SAXSanalysis by Anton Paar™.

To determine the orientation of each scattering feature with respect to the director, the intensity across a narrow band around each feature was investigated as a function of the azimuthal angle, χ, as demonstrated in Figure 3.12 for the $q \sim 14\text{nm}^{-1}$ feature. This methodology is also used to measure the order parameter for the material using the $q \sim 14\text{nm}^{-1}$ feature, as explained in Section 2.4.1.

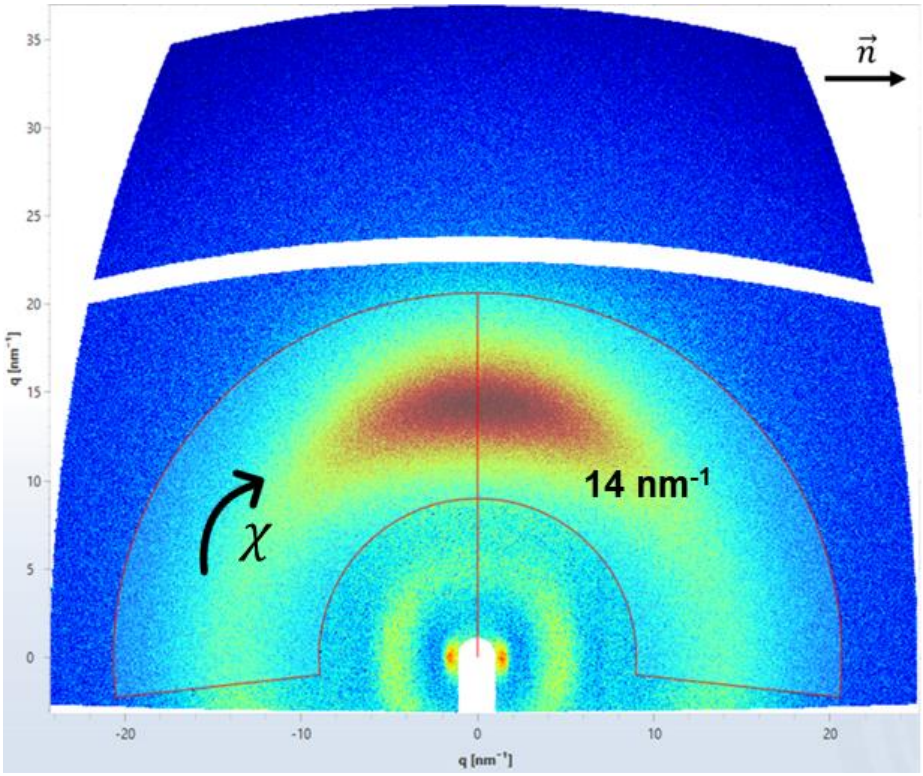

Figure 3.12. An example of the WAXS scattering of a monodomain nematic LCE in q (nm^{-1}). The scattering intensity, $I(\chi)$, is investigated along the azimuthal angle, χ (red-outlined light blue mask), for the anisotropic feature at q ~ 14 nm^{-1}. This was analysed using SAXSanalysis by Anton Paar™.

3.4.2.iii The Order Parameters

To extract an order parameter for the monodomain nematic LCEs, the feature at q ~ 14 nm^{-1}, which is measured with WAXS, is used; this feature is attributable to ~ 4.4 Å side-to-side spacing within the system.

Firstly, the *SAXSanalysis* program by Anton Paar™ was used to reduce the intensity data of this feature, $I(\chi)$, as shown above in Figure 3.12. A custom python script was written to enable the order parameters to be extracted, and the relevant theory was provided in Section 2.4.1.

To determine the error in the order parameters with this methodology, the Kratky fitting parameters were varied to determine the parameter limits that still allow for a good fitting to the intensity, $I(\chi)$. A series of good fittings are demonstrated in Figure 3.13, and it was found that the fitting parameter limits gave a variation in the order parameters of up to ± 0.03.

In Figure 3.13, the Kratky fittings to the azimuthal intensity, $I(\chi)$, are shown for data reductions, or data binning, between 25 and 200 data points. Clearly, the level

of binning has little effect on the order parameters that are measured using this methodology; $\langle P_2 \rangle$ shows a small reduction of 0.01, which is within the experimental error ($\pm$ 0.03), and $\langle P_4 \rangle$ shows no variation.

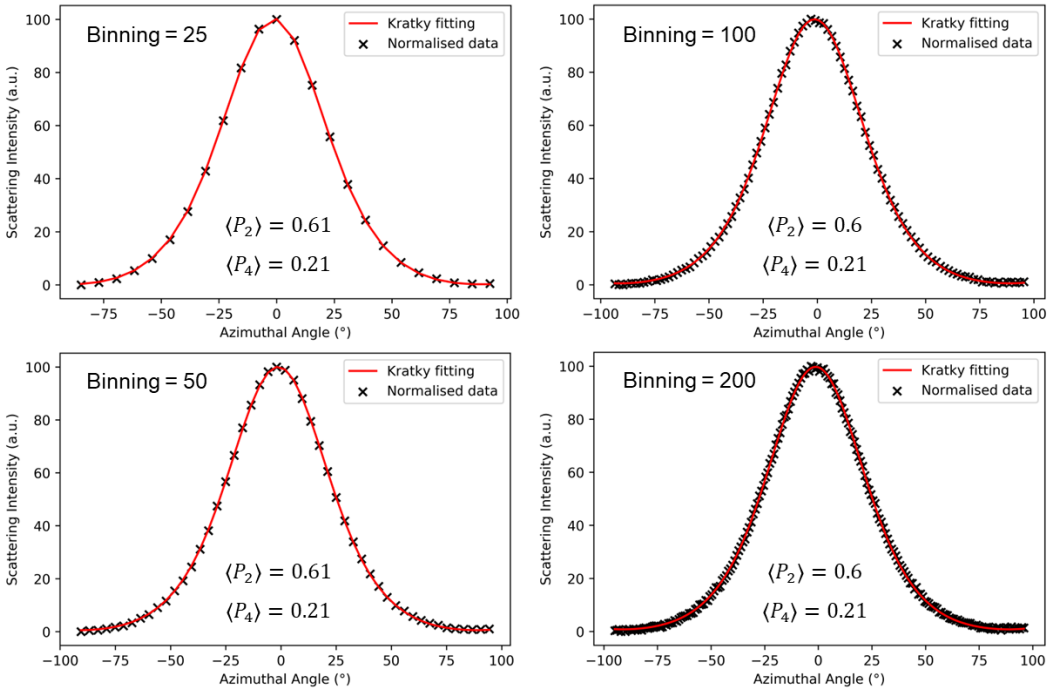

Figure 3.13. Fittings of the Kratky method (red line) to the experimental data of the q ~ 14 nm^{-1} feature (black crosses) for a monodomain nematic LCE of 62 mol% mesogenic content (nLCE-62) with varied amounts of data binning: 25, 50, 100, 200. The order parameters $\langle P_2 \rangle$ and $\langle P_4 \rangle$ show no variation outside of the experimental error of ± 0.03.

3.5 Optical Techniques

In Chapter 6, the optical properties of these material are explored. These investigations delve into the role of composition on the optical performance of monodomain nematic and isotropic LCEs, and how these can be tuned. Two optical methods were used to measure the refractive indices and the birefringence within this work: Abbé Refractometry and Spectroscopy. These techniques will be described below.

3.5.1 Abbé Refractometry

Undoubtedly, the most accurate methodology used to determine the refractive indices of liquid crystals is *via* an Abbé Refractometer, a technique which has been widely used for low molar mass materials at temperatures below ~80˚C. Refractometry techniques are also often used for measuring the refractive index of transparent plastics (23) and descriptions on this technique can be seen in previous literature, such as by de Angelis *et al.* (24).

Abbé Refractometry was similarly used by Broer *et al.* (25, 26) to study densely crosslinked liquid crystalline networks but this technique had not been used for LCEs until the work that is presented in this thesis, which has been published by Cooper *et al.* (1). The fact that the method requires a large (~ 1.5 cm by 3.5 cm), uniform, highly transparent area means that it can only be used with relatively large, well-aligned, monodomain samples, as are obtained for our LCEs with the fabrication techniques described in Section 3.2.

In fact, the acrylate-based LCEs considered in this work have a ~ 94% transparency at 589 nm, which was previously measured using Transmission Spectroscopy (1) and will be shown in Section 6.2. The transparency of our LCEs therefore enabled measurements of temperature-dependent refractive indices using a 60/ED Abbé Refractometer by Bellingham and Stanley™ and a Neslab™ RTE-4 refrigerated circulating bath.

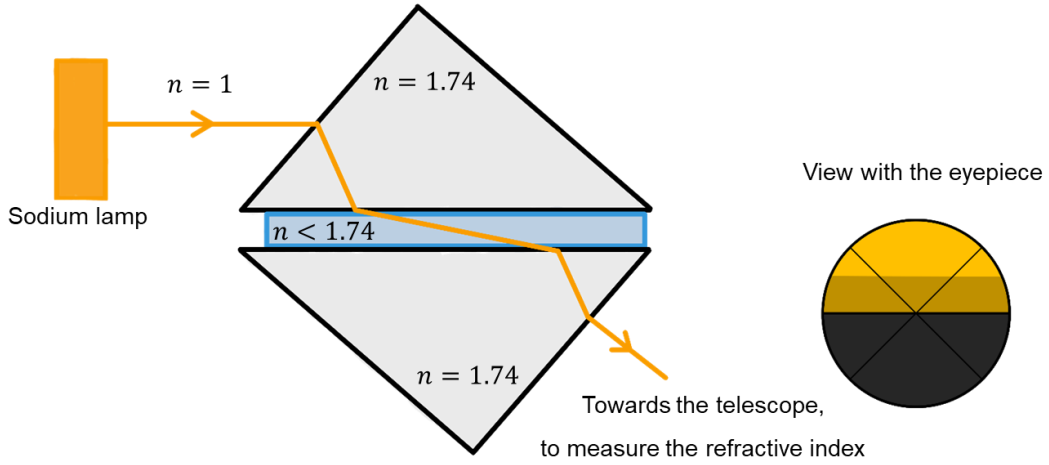

Figure 3.14. A schematic showing the light emitted from a sodium lamp (589 nm) that passes through an Abbé Refractometer to measure the refractive indices of a sample. The machine is limited to measuring materials with a refractive index, $n < 1.74$.

The Abbé Refractometer operates by determining the critical angle for total internal reflection of the sample with respect to a reference prism and is often used for studying the refractive indices of transparent liquids and solids (24). The LCEs were placed on the prisms of the Abbé Refractometer, with care taken to ensure good contact and the illumination was provided by a sodium lamp of wavelength 589 nm; a schematic of the Abbé Refractometer is shown in Figure 3.14. The refractive indices, n_o and n_e were measured at reducing temperature intervals of ~ 2°C between 55°C to 25°C. Multiple measurements were taken at each temperature, to calculate an average of each refractive index value with an error calculated from the standard deviation.

3.5.2 Reflection and Transmission Spectroscopy

During the Spectroscopy measurements, an Oceanview™ Spectrometer was connected to an Olympus™ microscope in either a reflection or transmission configuration. The Reflection and Transmission Spectroscopy results are given later in Section 6.2 and are both published by Cooper *et al.* (1). In the following section, the methodology for these shall be briefly described.

Reflection Spectroscopy was employed to determine the refractive index of poly(2-ethylhexyl acrylate), referred to here as pEHA. The pEHA material was made by Stuart Berrow. The Reflection Spectroscopy was conducted on a thin (~ 9 µm) film of pEHA contained between sealed glass slides. The methodology used here has been described in detail elsewhere (27).

In brief, the glass separation of the cell was measured with an accuracy of 0.1 μm and the gap was then filled with pEHA. The material's refractive index was determined with an accuracy of ~ 2% by fitting to the reflection spectrum (27). Specifically, this involved an in-house fitting program, known as the '*Reflection Spectrum Fitting Program'* that was developed over the years by Nick Roberts (2003), Hyung Guen Yoon (2008), and Paul Brimicombe (2009) and allows a fitting to the spectrum of a sample whilst considering various parameters such as the refractive indices, the thickness of the device and the presence of any alignment layers.

To determine the refractive index of the pEHA, the cell was held at 25.4°C using a Linkam™ LTS 350 hot stage connected to a Linkam™ TMS 93 temperature controller; this temperature was chosen to allow comparison to the average refractive index data of the monodomain nematic LCEs from the Abbé Refractometer.

The transmission spectra of a monodomain nematic LCE (nLCE-62, synthesised by Ethan Jull) was measured by Ethan Jull using the above methodology in a transmission configuration of the microscope. The data was corrected for the light losses due to Fresnel reflections by Ethan Jull and Helen Gleeson.

3.6 Density with Aqueous Glycerol Solutions.

In this work, a range of varied weight percent (wt.%) glycerol in water solutions were used to determine a precise density of the LCEs, in a similar method to Liu *et al.*, who documented the density change of cholesteric films in salt brine (28, 29). The density results are presented in Section 5.5, and the experimental procedure will be given below.

Although a simple calculation of density *via* measuring the mass and volume of the LCE could be used, this was found to lead to relatively large error (7% error) for small samples of LCEs (< 0.5 cm in length and width, thickness of ~ 100 μm and mass ~ 1 mg) and suggests that this simplistic method requires larger samples of LCEs than were readily available for an accurate determination of the density.

Aqueous glycerol solutions are a good candidate to measure the density of LCEs, since the temperature-dependent density of varied wt.% glycerol solutions (0 wt.% to 100 wt.%) are well known experimentally to a high precision (0.01% error)

around room temperature (15°C – 30°C) and have also been well theoretically modelled (0.07% error) within this temperature range (30, 31). Additionally, the LCEs demonstrate no sign of swelling in the aqueous glycerol solutions, so there is no influence of swelling on the density results. Another benefit of using the glycerol solutions is that small and irregularly shaped samples of LCE can be used to measure the density to a good precision (1% error).

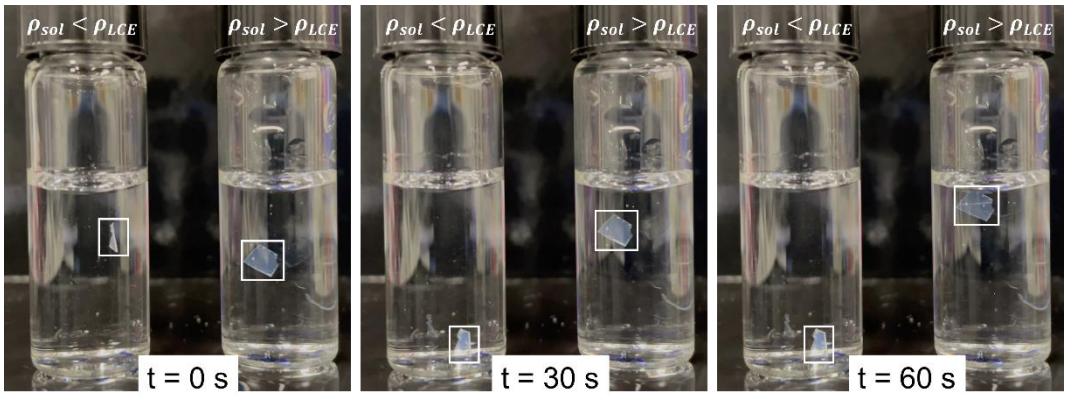

Figure 3.15. Two small samples of a monodomain nematic LCE (of the same composition) in vials of different wt.% glycerol solutions, shown over 60 seconds to sink in the glycerol solution with a lower density, and float in the glycerol solution with a higher density. The density of the LCE (ρ_{LCE}) is therefore between the densities of these solutions (ρ_{sol}). White boxes are added around the samples as a guide for the eye.

A series of aqueous glycerol solutions in steps of 5 wt.% were prepared, between 40 and 70 wt.%. The density of each glycerol solution was known using the calculated densities by Volk and Kähler (31), who calculated the densities of glycerol solutions between 0 wt.% and 100 wt.%, to the nearest 1 wt.% and 1°C (31).

The densities of the LCEs were established by the behaviour of the LCE within each solution at room temperature (21°C). Figure 3.15 demonstrates two small samples of the same LCE which sink or float in the lower and higher wt.% glycerol solution, respectively. The LCE therefore has a density between those of the glycerol solutions, so an average density of these solutions is used to provide a density of the LCE, in g/cm^3. An error in the density of ± 0.01 g/cm^3 was determined, by considering the error in the temperature and the concentration of the solution.

Lastly, the test seen in Figure 3.15 was repeated a few times to ensure a consistent behaviour of the LCE in the solutions; the presence of air bubbles on the surface of the LCE will lead to an incorrect density that is lower than the actual density.

3.7 References

1. Cooper, E.J., Reynolds, M., Raistrick, T., Berrow, S.R., Jull, E.I.L., Reshetnyak, V., Mistry, D. and Gleeson, H.F. Controlling the Optical Properties of Transparent Auxetic Liquid Crystal Elastomers. *Macromolecules.* 2024, **57**(5), pp.2030-2038. Available from: https://doi.org/10.1021/acs.macromol.3c02226
2. Herbert, K.M., Fowler, H.E., McCracken, J.M., Schlafmann, K.R., Koch, J.A. and White, T.J. Synthesis and alignment of liquid crystalline elastomers. *Nature Reviews Materials.* 2021. Available from: https://doi.org/10.1038/s41578-021-00359-z
3. Küpfer, J. and Finkelmann, H. Nematic liquid single crystal elastomers. *Die Makromolekulare Chemie, Rapid Communications.* 1991, **12**(12), pp.717-726. Available from: https://doi.org/10.1002/marc.1991.030121211
4. Wang, Z., Raistrick, T., Street, A., Reynolds, M., Liu, Y. and Gleeson, H.F. Direct Observation of Biaxial Nematic Order in Auxetic Liquid Crystal Elastomers. *Materials.* 2022, **16**(1). Available from: https://doi.org/10.3390/ma16010393
5. Berrow, S.R., Raistrick, T., Mandle, R.J. and Gleeson, H.F. Structure–Property Relationships in Auxetic Liquid Crystal Elastomers—The Effect of Spacer Length. *Polymers.* 2024, **16**(14), p.1957. Available from: https://www.mdpi.com/2073-4360/16/14/1957
6. Berrow, S.R., Mandle, R.J., Raistrick, T., Reynolds, M. and Gleeson, H.F. Toward Monodomain Nematic Liquid Crystal Elastomers of Arbitrary Thickness through PET-RAFT Polymerization. *Macromolecules.* 2024, **57**(11), pp.5218-5229. Available from: https://doi.org/10.1021/acs.macromol.4c00245
7. Moorhouse, T. and Raistrick, T. Sub-Micron Diffractive Optical Elements Facilitated by Intrinsic Deswelling of Auxetic Liquid Crystal Elastomers. *Advanced Optical Materials.* 2024, **12**(24), p.2400866. Available from: https://doi.org/10.1002/adom.202400866

8. Duncan, J. Principles and Applications of Mechanical Thermal Analysis. In: *Principles and Applications of Thermal Analysis*. 2008, pp.119-163.
9. Gabbott, P. A Practical Introduction to Differential Scanning Calorimetry. In: *Principles and Applications of Thermal Analysis*. 2008, pp.1-50.
10. Gabbott, P. Fast Scanning DSC. In: *Principles and Applications of Thermal Analysis*. 2008, pp.51-86.
11. Chartoff, R.P., Menczel, J.D. and Dillman, S.H. Dynamic Mechanical Analysis (DMA). In: *Thermal Analysis of Polymers*. 2009, pp.387-495.
12. Mistry, D., Connell, S.D., Mickthwaite, S.L., Morgan, P.B., Clamp, J.H. and Gleeson, H.F. Coincident molecular auxeticity and negative order parameter in a liquid crystal elastomer. *Nature Communications.* 2018, **9**(1), p.5095. Available from: https://doi.org/10.1038/s41467-018-07587-y
13. Menczel, J.D., Judovits, L., Prime, R.B., Bair, H.E., Reading, M. and Swier, S. Differential Scanning Calorimetry (DSC). In: *Thermal Analysis of Polymers*. 2009, pp.7-239.
14. Mistry, D. *Synthetic lenses for the ageing eye: a motivation for developing the mechanical applications of Liquid Crystal Elastomers*. PhD thesis, University of Leeds, 2018.
15. Zhang, Z., Panov, V.P., Nagaraj, M., Mandle, R.J., Goodby, J.W., Luckhurst, G.R., Jones, J.C. and Gleeson, H.F. Raman scattering studies of order parameters in liquid crystalline dimers exhibiting the nematic and twist-bend nematic phases. *Journal of Materials Chemistry C.* 2015, **3**(38), pp.10007-10016. Available from: https://doi.org/10.1039/C5TC02174J
16. Raistrick, T., Zhang, Z., Mistry, D., Mattsson, J. and Gleeson, H.F. Understanding the physics of the auxetic response in a liquid crystal elastomer. *Physical Review Research.* 2021, **3**(2), p.023191. Available from: https://doi.org/10.1103/PhysRevResearch.3.023191
17. Stribeck, N. *X-ray scattering of soft matter.* Berlin: Springer, 2007.
18. Agra-Kooijman, D.M. and Kumar, S. X-Ray Scattering Investigations of Liquid Crystals. In: J. W. Goodby, P. J. Collings, T. Kato, C. Tschierske, H. F. Gleeson and P. Raynes eds. *Handbook of Liquid Crystals*. Second ed., 2014, pp.1-38.
19. Richards, R.W. *Scattering methods in polymer science.* New York: Ellis Horwood, 1995.

20. National Institute of Standards and Technology. *Standard Reference Material® 660a Certificate.* 2000. Available from: https://www.nist.gov/srm

21. Huang, T.C., Toraya, H., Blanton, T.N. and Wu, Y. X-ray powder diffraction analysis of silver behenate, a possible low-angle diffraction standard. *Journal of Applied Crystallography.* 1993, **26**(2), pp.180-184. Available from: https://doi.org/10.1107/S0021889892009762

22. Blanton, T.N., Huang, T.C., Toraya, H., Hubbard, C.R., Robie, S.B., Louër, D., Göbel, H.E., Will, G., Gilles, R. and Raftery, T. JCPDS—International Centre for Diffraction Data round robin study of silver behenate. A possible low-angle X-ray diffraction calibration standard. *Powder Diffraction.* 1995, **10**(2), pp.91-95. Available from: https://doi.org/10.1017/S0885715600014421

23. Kasarova, S.N., Sultanova, N.G. and Nikolov, I.D. Temperature dependence of refractive characteristics of optical plastics. *Journal of Physics: Conference Series.* 2010, **253**(1), p.012028. Available from: https://doi.org/10.1088/1742-6596/253/1/012028

24. de Angelis, M. and Tino, G.M. Optical Instruments. In: Bassani, F., Liedl, G.L. and Wyder, P. eds. *Encyclopedia of Condensed Matter Physics*. Oxford: Elsevier, 2005, pp.159-175.

25. Broer, D.J., Hikmet, R.A.M. and Challa, G. In-situ photopolymerization of oriented liquid-crystalline acrylates, 4. Influence of a lateral methyl substituent on monomer and oriented polymer network properties of a mesogenic diacrylate. *die Makromolekulare Chemie.* 1989, **190**(12), pp.3201-3215. Available from: https://doi.org/10.1002/macp.1989.021901218

26. Broer, D.J., Lub, J. and Mol, G.N. Synthesis and photopolymerization of a liquid-crystalline diepoxide. *Macromolecules.* 1993, **26**(6), pp.1244-1247. Available from: https://doi.org/10.1021/ma00058a007

27. Yoon, H.G. and Gleeson, H.F. Accurate modelling of multilayer chiral nematic devices through the Berreman 4 × 4 matrix methods. *Journal of Physics D: Applied Physics.* 2007, **40**(12), p.3579. Available from: https://doi.org/10.1088/0022-3727/40/12/006

28. Liu, D., Bastiaansen, C.W.M., den Toonder, J.M.J. and Broer, D.J. Light-Induced Formation of Dynamic and Permanent Surface Topologies in Chiral–Nematic Polymer Networks. *Macromolecules.* 2012, **45**(19), pp.8005-8012. Available from: https://doi.org/10.1021/ma301628h

29. Liu, D. and Broer, D.J. New insights into photoactivated volume generation boost surface morphing in liquid crystal coatings. *Nature Communications.* 2015, **6**(1), p.8334. Available from: https://doi.org/10.1038/ncomms9334

30. Bosart, L.W. and Snoddy, A.O. Specific Gravity of Glycerol. *Industrial & Engineering Chemistry.* 1928, **20**(12), pp.1377-1379. Available from: https://doi.org/10.1021/ie50228a032

31. Volk, A. and Kähler, C.J. Density model for aqueous glycerol solutions. *Experiments in Fluids.* 2018, **59**(5), p.75. Available from: https://doi.org/10.1007/s00348-018-2527-y

Chapter 4 Altering the Physical Properties of LCEs *via* Phase Templating and Composition.

A portion of the work in this chapter has previously been published in (1):

Emily J. Cooper, *et al*. "*Controlling the Optical Properties of Transparent Auxetic Liquid Crystal Elastomers"*. Macromolecules, 2024, **57**(5), 2030-2038.

Any experimental work that was not performed by the author, Emily Jane Cooper, will be stated in the text or the figure caption.

4.1 Introduction

There are a range of proposed functions for Liquid Crystalline Elastomers (LCEs), covering areas such as soft robotics and mechanical actuators (2-4), self-cleaning materials (5), biomimetic and biological devices (6-8), impact resistant devices (9, 10) and sensors (11, 12). When considering the potential of a specific material for an application, a thorough knowledge of the material's response to stimuli such as temperature and strain is essential. For instance, a commercial polymeric material will have the following properties documented (13):

i. thermal (melting temperature, glass transition temperature, coefficient of linear thermal expansion),
ii. mechanical (Poisson's ratio, moduli),
iii. physical (density),
iv. optical (refractive indices, transparency).

Throughout this chapter, we shall focus on the thermal and mechanical properties of a series of LCEs. The thermal property of the glass transition temperature, T_g, will be measured with various methodologies, including the enthalpic change seen with Differential Scanning Calorimetry (DSC), and the peak in the loss modulus, the peak in the loss tangent, and an average of these, all measured using Dynamic Mechanical Thermal Analysis (DMTA). We will then demonstrate that the T_g measured from each of these methodologies agrees well with previous trends in literature for these methods (14) and for polymeric materials (15).

In this chapter, we will first explore the thermal and mechanical responses of acrylate based LCEs, since many of the potential applications for LCEs discussed

above, require a temperature-dependent response of the material. This work will be split into two investigations, the first of which will consider the impact of templating on the material properties and the second will examine the role of composition on the properties of monodomain nematic LCEs.

Nematic LCEs, particularly polydomain nematic, have previously been shown to be effective energy dissipators (9, 10, 16). Therefore, we will investigate three distinct templates of LCEs for comparison: monodomain nematic, polydomain nematic, and isotropic. Specifically, we will be using one LCE composition during the templating investigations, known as LCE-62 (62 mol% mesogenic content), whose thermal and mechanical properties have been formerly reported (1, 17-20). Here, we will compare results for the glass transition temperature, T_g, measured using DSC and DMTA methodologies and compare these with previous reports for the same material (1, 18, 19). Then, the moduli and the loss tangent of the templates will be measured using DMTA, which will show an effective dissipation of each template.

Following this, we will investigate how the materials can be optimized for applications, such as impact resistance, through the modification of the composition. Section 4.3 will solely use the monodomain nematic LCE template, since only this template of the three previously considered exhibits an auxetic response and has therefore been more widely investigated within this family of materials (1, 17-23). As outlined in Section 3.2.1, the overall mesogenic content of the monodomain nematic LCEs was systematically varied using a fixed mol% ratio of RM82:A6OCB (1:7). Using a wide range of LCE compositions (76 to 93 mol% mesogenic content for precursor LCE mixtures and 56 to 72 mol% mesogenic content for polymerized LCEs), we will demonstrate that an increase in the mesogenic content leads to an increase in the transition temperatures. This trend has been previously reported in literature due to an increase in the mesogenic content, the liquid crystalline content, and the crosslinking density (1, 24, 25).

We will also focus on three monodomain nematic LCEs which exhibit an optimal dissipation around room temperature, to compare the applicability of these materials for dissipation purposes: nLCE-62, nLCE-66, and nLCE-72. We will also consider the auxetic response of these materials to fully comprehend their

dissipative capabilities. Lastly, we will demonstrate that two monodomain nematic LCEs, of low and high mesogenic content, fail to exhibit an auxetic response and the causes for this will be discussed.

4.2 The Impact of Templating on the Thermal and Dissipative Behaviour

A comprehensive understanding of the importance of phase templating to the material properties is essential for the design of applications. Previously, the templates within this family of acrylate LCEs have each demonstrated unique intrinsic behaviours, with the isotropic LCEs lending themselves to be good candidates for strain sensors (11) and the monodomain nematic LCEs exhibiting auxetic behaviour (17-19, 21-23) that shows good potential for impact resistance and could prove useful as laminates for impact resistant glass (1). However, there are no prior reports on the polydomain nematic LCEs, due to the opacity limiting the applications of this template.

Indeed, LCEs have already been anticipated to be excellent candidates for enhancing the impact resistance of protective gear (9, 10, 16) and it is easy to see the rationale for recommending LCEs, with their good flexibility and useful energy dissipation. Therefore, in this section we will explore the thermal and dissipative properties for a variety of templates of the acrylate-based family of LCEs. The dissipation has previously been reported for the monodomain nematic (18) and isotropic (25) LCEs within this family, however a direct comparison between these templates and the polydomain nematic and has not yet been explored.

During this first section, we will determine the glass transition temperatures, the dissipative properties, and the thermal shape changes for LCEs of different templates. For clarity, this initial templating investigation will be conducted using a single composition of 62 mol% mesogenic content, which will be polymerized into monodomain nematic, polydomain nematic, and isotropic LCEs.

4.2.1 Heat Flow and the Glass Transition Temperature with DSC

First, we will study the variations of the DSC heat flow traces over a wide temperature range for the three templates of polymerized LCEs. This is an

important start to the investigation for three purposes: (i) understanding the effect of templating on the overall thermal behaviour of these materials, (ii) searching for a T_{NI} in the nematic LCEs, and (iii) measuring the T_g of all three LCE templates.

The DSC traces are plotted in Figure 4.1 against the weight normalised heat flow (W/g) for monodomain nematic, polydomain nematic and isotropic LCEs of the same composition. The traces in Figure 4.1 are taken from the second cooling and heating cycles for each of the LCEs, which were loaded into pans with weights between 5.6 - 6.5 mg. We shall discuss the role of templating on the general thermal behaviour seen on the DSC traces across the wide temperature range (-50°C to 250°C) of the heating and cooling cycles, before moving onto the measurement of the glass transition temperatures.

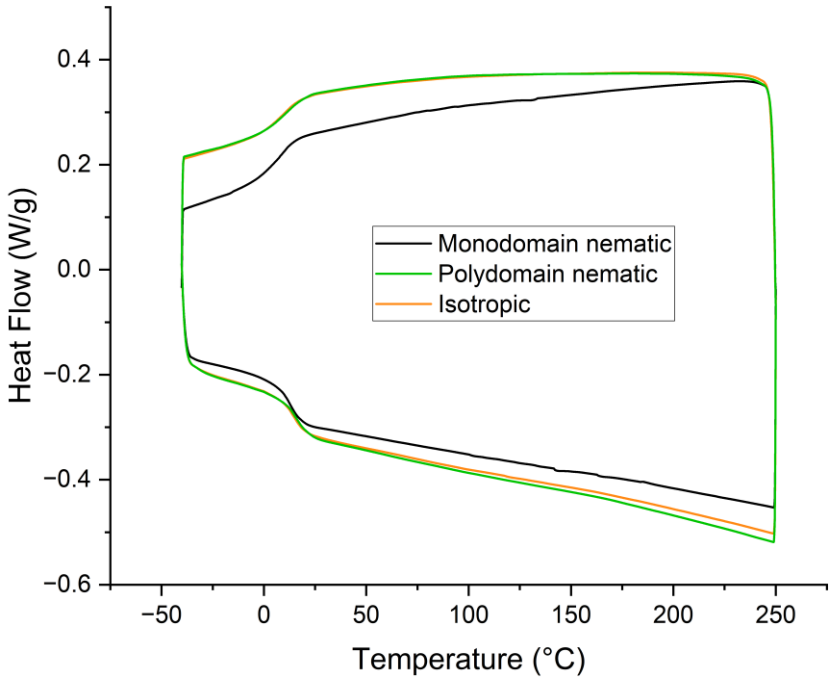

Figure 4.1. The weight normalised heat flow (W/g) of monodomain nematic (black), polydomain nematic (green) and isotropic (orange) LCEs of the same composition (62 mol% mesogenic content), measured using heating and cooling cycles at 10°C/min between - 50°C and 250°C.

In Figure 4.1, the traces of the polydomain nematic and isotropic LCEs demonstrate similar heat flow curves across both heating and cooling, signifying that the overall thermal behaviour of a polydomain nematic LCE is comparable to an isotropic LCE within this family. In addition, the thermal behaviour of the monodomain nematic LCE in Figure 4.1 is clearly distinct from the polydomain nematic and isotropic LCEs, with the former demonstrating a heat flow that continuously changes on

cooling (top half of trace in Figure 4.1) at temperatures above the glass transition temperature. In contrast, the polydomain nematic and isotropic LCEs demonstrate a heat flow that begins to plateau at temperatures above the glass transition.

We shall now discuss the glass transition temperatures that were found using Figure 4.1 and measured to be (9.4 ± 0.6)°C, (11.2 ± 0.6)°C, and (10.5 ± 0.6)°C for the monodomain nematic, polydomain nematic, and isotropic LCEs, respectively. Indeed, a difference in the T_g is expected between each templating; Jull *et al.* have previously demonstrated that the T_g is consistently higher for isotropic LCEs when compared to monodomain nematic LCEs. This was shown using acrylate based LCEs, similar to the materials investigated within this thesis, and a ~ 9°C higher T_g for isotropic LCEs was attributed to a higher degree of polymerization (25).

Similar to the work by Jull *et al.* (25), our results demonstrate a ~ 1°C higher T_g for an isotropic LCE, when compared to the monodomain nematic LCE. We do however observe a T_g for the polydomain nematic LCE that is slightly higher than the T_g for the isotropic LCE, but within the bounds of experimental error. Thus, the higher T_g for the polydomain nematic and isotropic LCEs suggests a similar degree of polymerization for these templates, which are both significantly higher degrees of polymerization than the monodomain nematic LCE.

Lastly, there are interesting features on the trace of the monodomain nematic LCE in Figure 4.1, that appear as small fluctuations in the heat flow to an otherwise smooth trace, at temperatures between ~ 100°C - 200°C. It is tempting to interpret these as an indication of a T_{NI}, however the temperature at which these small changes to the curve appear are not reproduceable between cycles or between samples and could be due to other effects such as delamination of the material from the base of the pan. We therefore observe no evidence of a T_{NI} in the monodomain nematic LCE. Additionally, we observe no evidence of a T_{NI} in the polydomain nematic template, which instead appears to exhibit an isotropic-like thermal behaviour. Therefore, we will now investigate the thermal shape changing properties of the monodomain and polydomain nematic LCEs to determine whether these indeed display different average thermal behaviour.

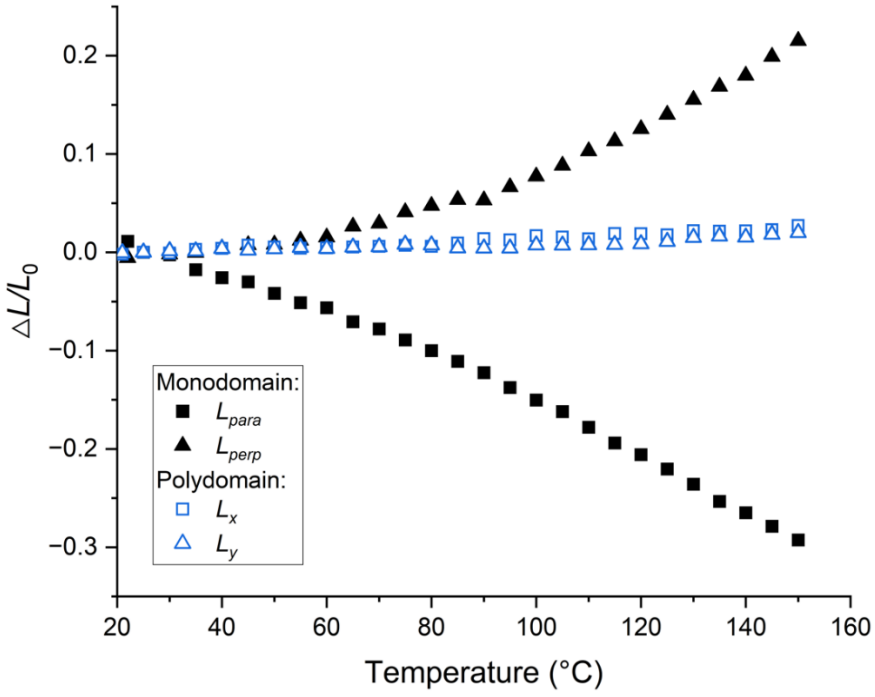

Figure 4.2. The thermal shape changes of the monodomain and polydomain nematic LCEs between 22°C and 150°C. This is measured for axes perpendicular (black triangle) and parallel (black square) to the director for the monodomain nematic LCE, and are measured for orthogonal axes, L_x (empty blue square) and L_y (empty blue triangle) for the polydomain nematic LCE.

The LCE shape change was measured using small samples placed on a small amount of silicon oil covering a glass slide, and according to the method given in Section 3.3.4. These samples were cut with dimensions perpendicular (L_{perp}) and parallel (L_{para}) to the director for the monodomain nematic LCEs, however since there is no macroscopic director to the polydomain nematic LCEs, the sample was simply cut for orthogonal axes that will be denoted as L_x and L_y.

Figure 4.2 shows the relative length change ($\Delta L/L_0$) along each axis of the monodomain nematic and polydomain nematic LCEs, where L_0 is simply defined as the length of each axis at 25°C. We can clearly see that the monodomain nematic LCE exhibits a large anisotropic shape change upon heating, with a contraction parallel and an expansion perpendicular to the original director; this behaviour is expected for monodomain nematic LCEs (26). Furthermore, this observed large shape change is most likely responsible for the small features seen in the DSC of the monodomain nematic LCE in Figure 4.1 which are likely due to sample delamination.

Interestingly, in Figure 4.2 the polydomain nematic LCE exhibits an isotropic behaviour that can be simply attributed to the thermal expansion of the material. This further highlights the disparity in the thermal behaviour between these nematic templates and supports that the average thermal behaviour of the polydomain nematic template is identical to the isotropic template.

4.2.2 Comparing the Dissipation of the Templates with DMTA

As aforementioned in Sections 2.6 and 3.3.2, one can probe the storage and loss modulus of a material using DMTA, with the ratio of the loss modulus over the storage modulus providing the loss tangent (also known as $tan\,\delta$). It is well accepted that the magnitudes of the loss modulus and the loss tangent quantify the energy dissipation of a material, with good dissipation evidenced by a greater loss modulus than storage modulus, and a consequently high loss tangent (27). In fact, nematic LCEs have undoubtedly been demonstrated to be effective dissipators with reports of the loss tangent magnitude of up to ~ 1.5 (10, 16), and reports of broad peaks of the loss tangent due to T_g and T_{NI} (28, 29).

In this section, we will again use a single composition (62 mol% mesogenic content) to consider the temperature-dependent dissipative capabilities of the monodomain nematic, polydomain nematic, and isotropic templates. The moduli and the loss tangent for each of these templates will be investigated over a temperature window of - 10°C to 50°C, to concentrate on the material properties at room temperature and approximately 30°C either side. Here, the templates are only investigated along one axis, since DMTA on these materials was predominantly employed for a single measure of the T_g per template. Therefore, the axis perpendicular to the director for the monodomain nematic LCE was selected since this axis is of particular interest during other investigations and will later be explored under strain to exhibit an auxetic behaviour of the material.

The temperature-dependent loss and storage moduli for each template are shown in Figure 4.3. Each template demonstrates similar magnitudes of moduli, with however, the nematic templates showing slightly higher loss moduli than the isotropic template. However, the key difference between the templates in Figure 4.3 is a shift of the moduli with temperature, which is attributable to the difference in

the glass transition temperatures; the T_g of each template will later be measured and compared.

For all the templates, there are two temperature regions of interest for the moduli. Firstly, the peak of the loss modulus for each template in Figure 4.3 is below room temperature (between 0°C – 10°C) and this can be used as a measure of the T_g. Secondly, we can clearly see that the loss modulus exceeds the storage modulus between a window of roughly 10°C – 25°C for these templates. This signifies that the viscous nature of these materials is greater than the elastic nature within this temperature range and should correspond to a large loss tangent. The loss tangent for these templates will now be explored.

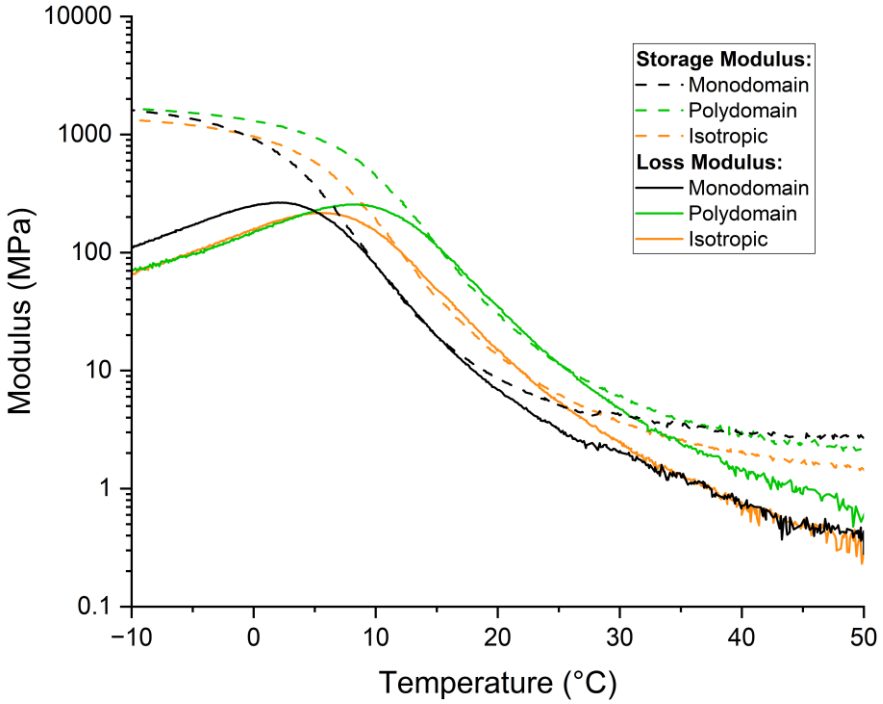

Figure 4.3. The storage (dash lines) and the loss moduli (solid lines) measured using DMTA between -10°C and 50°C at 2°C/min for three LCE templates: isotropic (orange), polydomain nematic (green) and monodomain nematic (black), with the latter probed perpendicular to the director. Each template contains 62 mol% mesogenic content.

The loss tangent for the three templates can be seen in Figure 4.4 between -10°C and 50°C, and we indeed observe a peak of the loss tangent between the temperatures of ~ 10°C – 25°C. In fact, we see the magnitude of the loss tangent exceeding a value of 1, which has been previously reported for the monodomain nematic LCE (18). The existence of a high loss tangent indicates that these materials are good candidates for impact resistance devices operating at ambient

temperatures. Furthermore, the peak of the loss tangent can be a measure for the T_g, which will be measured and discussed in the following section.

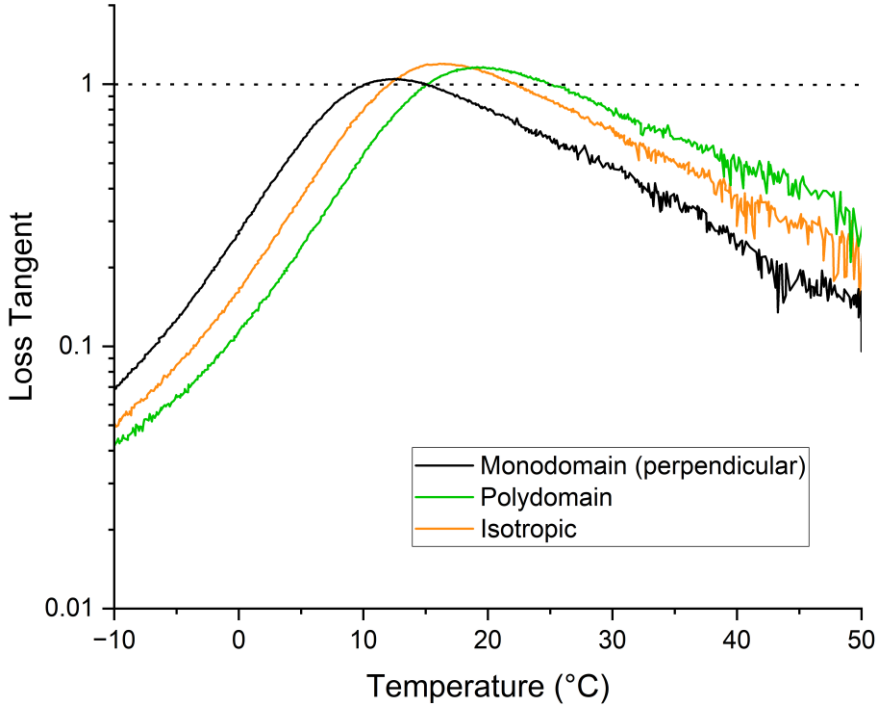

Figure 4.4. The peaks of the loss tangent ($\tan\delta$) measured using DMTA between -10°C and 50°C at 2°C/min for three LCE templates of isotropic (orange), polydomain nematic (green) and monodomain nematic (black), with the latter probed perpendicular to the director. All these LCEs contain 62 mol% mesogenic content. A black dotted line is provided as a guide for the eye at a loss tangent of 1.

As aforementioned, previous literature for LCEs have reported a broad shoulder of the loss tangent due to T_g and T_{NI} (28, 29) and reported a high maximum of the loss tangent (~ 1.5) for polydomain nematic LCEs (10, 16). However, the nematic LCEs investigated in this thesis do not show a T_{NI} with film clamp DMTA (investigated to 50°C) or DSC (investigated to 250°C) and only exhibit one loss tangent peak (due to T_g) with DMTA. However, there is evidence to suggest that investigating these materials in a shear configuration can provide further insight, with shoulders appearing on the loss tangent (30). Nevertheless, this family of LCEs are unique compared to other liquid crystalline networks due to the auxetic behaviour in the monodomain nematic template, which is not simply accounted for using solely DMTA experiments. This will be later explored in Section 4.3.3.

In the following section, the glass transition temperatures will be measured using DMTA (Figure 4.3 and Figure 4.4) and compared to DSC (Figure 4.1).

4.2.3 Comparing the Glass Transition Between Techniques.

In Section 4.2.1, we measured the glass transition temperature for three different LCE templates of the same composition, using Differential Scanning Calorimetry (DSC). Dynamic Mechanical Temperature Analysis (DMTA) on these materials was also investigated in the previous section (4.2.2) and it was mentioned that this technique can be used to measure the glass transition temperature. In fact, DMTA is frequently used within the polymer science field, where the peak of the loss modulus or the peak of the loss tangent are both suitable measures for the T_g (27). Using these methods, the loss modulus provides a T_g that represents an onset of the transition, whereas the peak in the loss tangent measures a T_g at a higher temperature and during the transition (14, 27).

Another measure of the T_g that has been suggested is using an average of the loss modulus T_g and the loss tangent T_g; Achorn *et al.* (15) previously demonstrated using polystyrene and polyurethane networks that an average T_g using DMTA is closer to the T_g that is measured by DSC. There is admittedly no theoretical basis for this average and therefore this measure will only be used for comparison purposes.

Therefore, in this section we will measure the glass transition temperature using the loss modulus, the loss tangent, and provide an average of these. This will enable a detailed comparison between the three values of T_g from DMTA to the T_g from DSC. We will begin this investigation by discussing the results for the loss modulus and the loss tangent, followed by an overall comparison between the methodologies. A summary of the glass transition temperatures for each methodology can be seen in Table 4-1 and a comparison of the measured T_g's between the techniques is shown in Figure 4.5.

Table 4-1. The glass transition temperature, T_g, of monodomain nematic, polydomain nematic, and isotropic LCEs, measured using DMTA (the loss modulus, the loss tangent, and an average) and using DSC.

	Glass Transition Temperature, T_g			
Template of LCE	**DSC (± 0.6 °C)**	**DMTA: Loss Mod. (± 1 °C)**	**DMTA: Loss Tan. (± 1 °C)**	**DMTA: Average (± 1 °C)**
Nematic (monodomain)	9.4	2	12	7
Nematic (polydomain)	11.2	8	19	14
Isotropic	10.5	6	16	11

We will first address the variation of the T_g between the methodologies, before comparing the T_g of the templates. In Figure 4.5 is it clear that measuring the peak of the loss tangent consistently offers the highest glass transition temperatures, and measuring the peak of the loss modulus is consistently the lowest. Indeed, there will always be a difference in the T_g measured using the loss modulus and the loss tangent (14), and here we observe the loss modulus T_g ubiquitously reported ~ 10°C lower than the loss tangent T_g (see Table 4-1).

In between the glass transition temperatures that were measured using the loss tangent and the loss modulus, we observe similar T_g's for the average DMTA and DSC methods, which is in agreement to previous literature that investigated the T_g of polystyrene and polyurethane (15). Despite no theoretical basis for the average T_g measured with DMTA, this clearly defines a T_g closer to that measured using DSC and is therefore a useful measure for comparison.

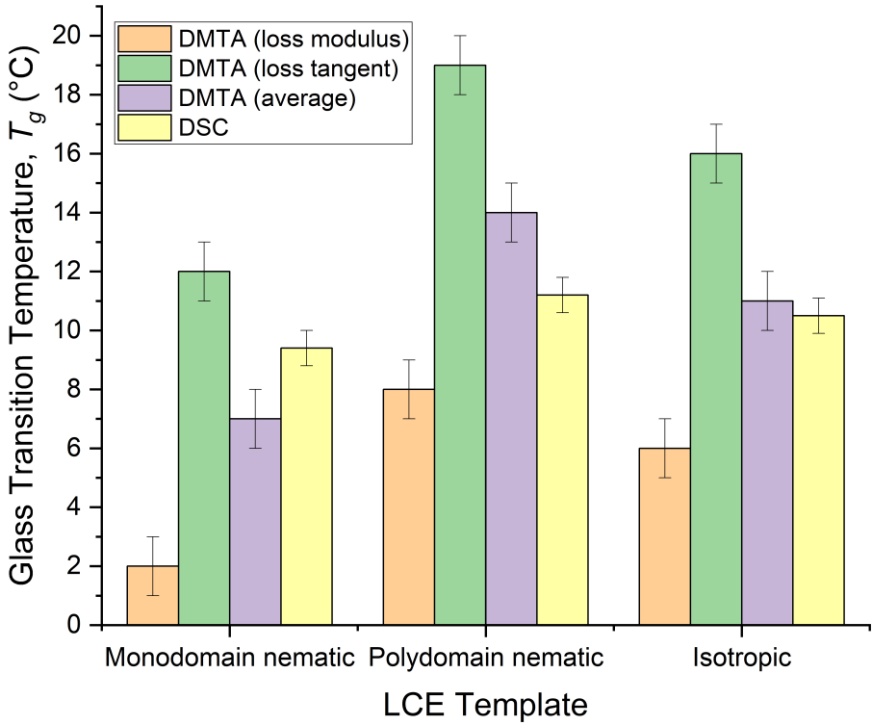

Figure 4.5. A comparison of the glass transition temperatures measured using different techniques for three different templates of LCEs: monodomain nematic, polydomain nematic, and isotropic. The techniques used to measure the T_g's include the peak of the loss modulus from DMTA (orange), the peak of the loss tangent from DMTA (green), the average DMTA (purple), and the inflection of T_g from DSC (yellow).

We will now compare the T_g measured for the different LCE templates in Figure 4.5. We consistently observe that the polydomain nematic template has the highest T_g, followed by the isotropic LCE, then the monodomain nematic LCE. Jull *et al.* previously examined similar compositions of monodomain nematic and isotropic LCEs and demonstrated that isotropic LCEs have a higher T_g due to a greater degree of polymerization (25). Although polydomain nematic LCEs were not considered in their investigation, our results rather interestingly infer that polydomain nematic LCEs may have an even higher degree of polymerization than isotropic LCEs. This further adds to the prior notion that the thermal behaviour of the polydomain nematic LCEs within this family is akin to the isotropic LCEs (discussed in Section 4.2.1) and these are altogether different in the overall thermal behaviour from the monodomain nematic LCEs. Now that the thermal behaviour of the LCE templates has been established, we will now focus on the impact of plasticizer content on the thermal and mechanical behaviour of the monodomain nematic LCEs.

4.3 The Impact of Composition on the Thermal and Mechanical Behaviour

Understanding the thermal behaviour of a material is vital for its application within a particular temperature window. This is a recurring subject throughout this thesis, with investigations into many of the temperature-dependent properties of this family of LCEs. For example, the glass transition temperature of an LCE will impact the temperature window over which it can be used for applications that require a rubbery material.

The following section will explore how these transition temperatures can be tuned *via* the mesogenic content of an LCE, to provide a wider range of materials that are suited to a range of temperatures. In this work, solely the monodomain nematic LCE will be investigated, since it is with this template that an auxetic behaviour is observed.

4.3.1 Transition Temperatures with DSC

In a similar manner to the preceding work on LCE templating, the following section will investigate the transition temperatures using DSC and DMTA, with however, a focus on understanding the impact of composition on a single templating; monodomain nematic LCEs.

Using a range of compositions, DSC was used to directly measure the T_{NI} of the precursor LCE mixtures and the T_g of the polymerized LCEs; a summary of the results can be seen in Table 4-2. Later, DMTA will be used to measure the T_g for polymerized LCEs and the results of the glass transition temperatures from both DSC and DMTA will be compared.

Table 4-2. The nematic-to-isotropic transition temperatures (T_{NI}) of the precursor LCE mixtures and the glass transition temperatures (T_g) for the corresponding polymerized monodomain nematic LCEs. The mol% mesogenic content of the precursor mixture and corresponding polymerized LCE is shown; note that the precursors have a higher mesogenic content due to the presence of 6OCB, which is washed from the polymerized LCE. These results have been published by Cooper et al. (1).

Mesogenic Content (± 1 mol %)		**Transition Temperatures (± 0.6 °C)**	
Precursor Mixture	**Polymerized LCE**	T_{NI} of Precursor Mixture	T_g of Polymerized Nematic LCE
76	56	27.5	1.7
78	59		5.0
80	62	34.9	9.4
82	64		7.9
83	66	38.6	9.7
84	67	42.4	13.1
88	72	45.7	16.3
91	80	50.5	
93	84	55.9	

As aforementioned, it is imperative to know the T_{NI} of the precursor LCE mixture to ensure polymerization in the correct phase (nematic or isotropic). Figure 4.6 shows the T_{NI} for the precursor mixtures over the range of mesogenic content studied (76 – 93 mol%). As a reminder, these precursor LCE mixtures have a higher mesogenic content than the corresponding polymerized LCEs, since these contain approximately 50 - 60 mol% of 6OCB which is washed out of the polymerized LCEs. Prior explanation of the synthesis of the LCEs can be accessed in Section 3.2.2.

Figure 4.6 shows the T_{NI} of the precursor mixtures and the T_g of the corresponding polymerized monodomain nematic LCEs. For all composition shown, the precursor mixtures have a T_{NI} above room temperature, which enables the synthesis of nematic LCEs at room temperature. For the polymerized and washed LCEs, the T_g for all composition shown are below room temperature (between ~ 2°C and 16°C), and so these materials will be in a rubbery state at room temperature. There is a difference of approximately ~ 25°C to 30°C between the T_{NI} of the precursor LCE mixture and the T_g of the polymerized LCE.

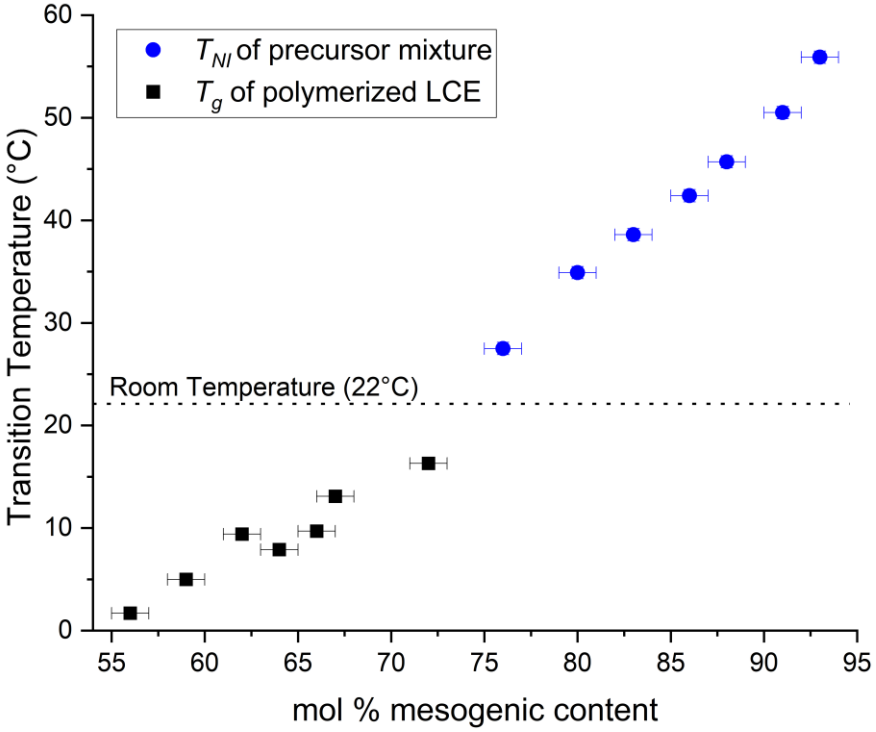

Figure 4.6. The nematic-to-isotropic transition temperatures (T_{NI}) of the precursor LCE mixtures (blue circles) and the glass transition temperatures (T_g) of the polymerized nematic LCEs (black squares) all measured for varied mesogenic content. The precursor mixtures include 6OCB within the mesogenic content, which is later washed from the polymerized LCE, hence the higher mesogenic content for the precursor mixtures. All transition temperatures are measured using Differential Scanning Calorimetry (DSC) to an accuracy of 0.6°C. These results have been published by Cooper et al. (1).

As would be expected (1, 24), the precursors with a greater mesogenic content (which includes the non-reactive 6OCB) show higher values of T_{NI}. Since all the nematic LCEs were polymerised in the nematic phase at room temperature, this therefore means that for LCEs with a higher mesogenic content, their network was formed deeper into the nematic phase.

Figure 4.6 shows the transition temperatures for the precursor mixtures and the polymerized LCEs, which all show an approximately linear increase with mesogenic content. The linear dependence of T_{NI} on the mol% of mesogenic content can be understood from Maier Saupe theory (31-33) as follows (1, 34). It is known that $T_{NI} = \frac{4.55\,U(T_{NI})}{k_B}$, where $U(T_{NI})$ describes the magnitude of the anisotropic part of the intermolecular interaction; this is temperature-independent in Maier Saupe theory. It is reasonable to assume that the intermolecular interaction parameter $U(T_{NI})$ is a linear function of the mole fraction of mesogenic content.

Then, from $T_{NI} = \frac{4.55\ U(T_{NI})}{k_B}$, the nematic-to-isotropic transition temperature, T_{NI}, should also be a linear function of the mole fraction of mesogenic content, which is supported by Figure 4.6. This linear relation between T_{NI} and the liquid crystalline content of a network has also been previously reported Barnes *et al.* (24). This theory was provided by Victor Reshetnyak and is published in Cooper *et al.* (1).
Similarly, the T_g of the polymerized LCEs demonstrates an approximately linear increase with mesogenic content. The trend of an increased T_g with an increased mesogenic content in Figure 4.6 can be understood in two ways. Firstly, the materials with lower mesogenic content contain a greater fraction of EHA. As pEHA (poly-EHA) has a T_g of ~ -69°C (35), increased amounts of EHA can be expected to lower the glass transition temperature of the LCE. Secondly, in this system, an increase in quantities of EHA also slightly decreases the mol% of the crosslinking group RM82 (see Table 3-1 in Section 3.2.1), thus increasing the mobility of the network and lowering the material's T_g. There are reports in literature of this linear dependence between the T_g and the liquid crystalline content (1) and for crosslinker density (25).

As aforementioned, the glass transition temperature can also be measured with alternative methodologies including the peak of the loss modulus or the peak of the loss tangent, both found using DMTA. Next, we will compare the dissipative properties using DMTA, before extracting the glass transition temperatures from DMTA and comparing these to the T_g measured with DSC above.

4.3.2 The Impact of Composition on the Dissipation

Earlier, we established that the monodomain nematic template exhibits good dissipative capabilities. The purpose of the following work is to tune the dissipative properties of the monodomain nematic LCEs, *via* the mesogenic content within the network. Here, we will investigate three compositions: 62 mol% (which was investigated in Section 4.2.2), 66 mol%, and 72 mol% mesogenic content. These materials were chosen, since each of these LCEs have just been investigated using DSC and are expected to show good dissipation around room temperature.

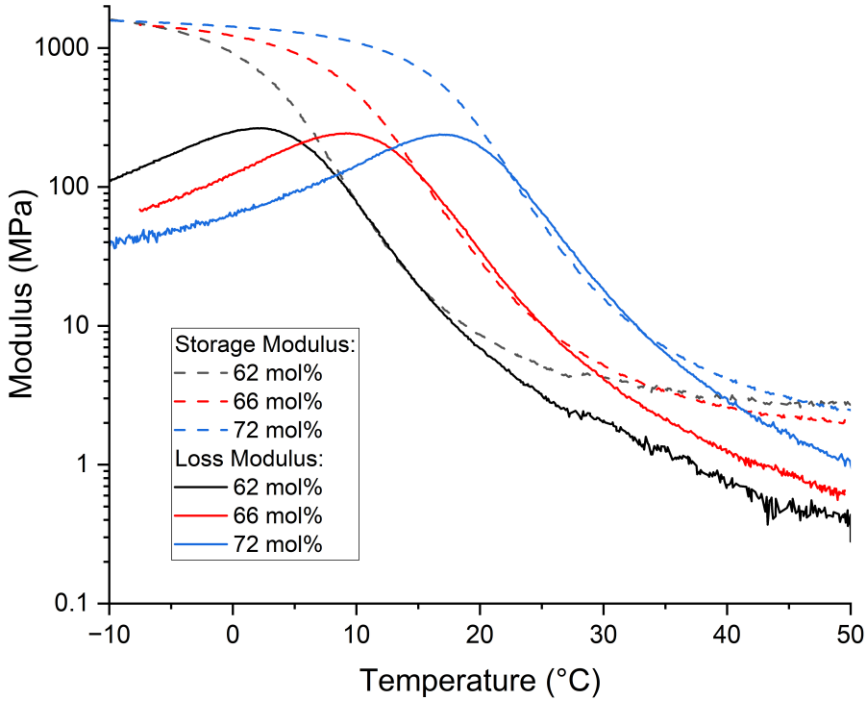

Figure 4.7. The storage modulus (dashed line) and loss modulus (solid line) of monodomain nematic LCEs measured using DMTA between -10°C and 50°C at 2°C/min, with mesogenic contents of 62 mol% (black), 66 mol% (red), and 72 mol% (blue). All samples have been investigated perpendicular to the director.

Figure 4.7 shows the storage and the loss moduli for three compositions of the monodomain nematic LCEs. For the compositions investigated, we clearly see comparable magnitudes for the loss and the storage moduli; the key difference in Figure 4.7 is the shift in temperature due to the glass transition temperature. In fact, we see that nLCE-72 has a near maximum loss modulus at room temperature (peak at 17°C), suggesting this material could be the most effective dissipator at room temperature. To fully compare the dissipative capabilities of these materials, the loss tangent needs to be examined, which compares the ratio of the loss and storage moduli.

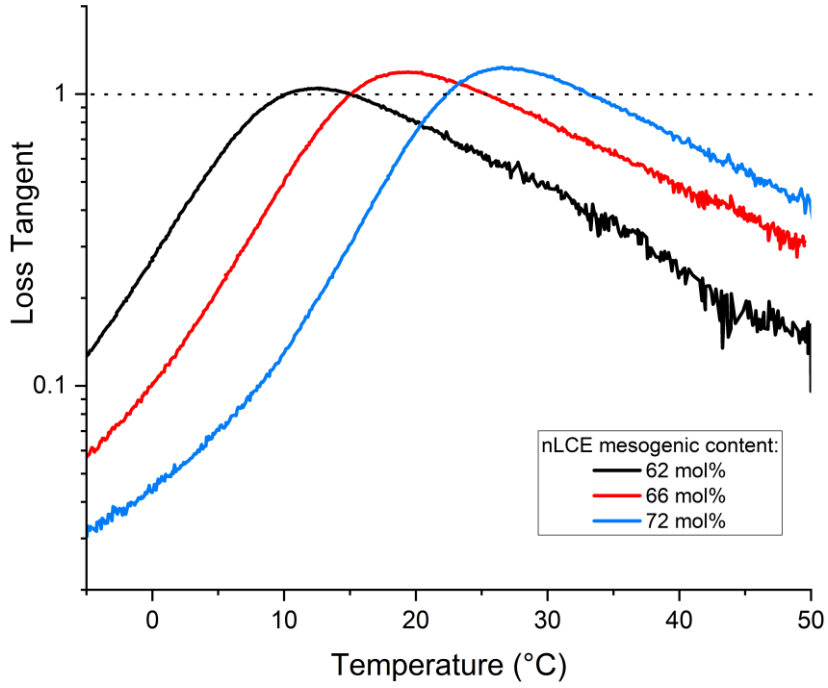

Figure 4.8. The dissipative measure, loss tangent (tanδ) measured using DMTA between -10°C and 50°C at 2°C/min for three monodomain nematic LCE compositions: 62 mol% (black), 66 mol% (red), and 72 mol% (blue) mesogenic content, which were all probed perpendicular to the director. A black dotted line is provided as a guide for the eye at a loss tangent of 1.

The loss tangent is shown in Figure 4.8; all compositions demonstrate good dissipation and a loss tangent magnitude greater than 1, which has also been reported for the nLCE-62 previously (18). We observe a trend of an increase in the magnitude of the loss tangent, occurring at higher temperatures, for a greater mesogenic content. In fact, the greatest magnitude of the loss tangent is seen for nLCE-72 (at 27°C), which suggests that this material demonstrates the best overall dissipation capabilities. Interestingly, nLCE-66 displays near maximum dissipation around room temperature (loss tangent peak at 19°C), and therefore lends itself to be the best candidate as a room temperature dissipator.

As aforementioned, these monodomain nematic LCEs exhibit a unique auxetic behaviour which could be an additional mechanism for impact resistance. To understand how these materials can dissipate energy, we should also look at the onset of the auxetic response of these materials, and how this may be tuned with composition. Therefore, we will now investigate the auxetic behaviour for these three compositions and two further compositions we have previously investigated using DSC, which will represent the outer formulation limits of the nematic LCEs.

4.3.3 The Impact of Composition on the Auxetic Behaviour

The monodomain nematic materials within this family of acrylate based LCEs exhibit a unique 'auxetic' behaviour, where above some threshold of applied strain, the material thickens along an axis orthogonal to both the applied strain and the original director. Specifically, these materials are defined as partially auxetic since the thickening occurs along only one axis (21, 36). Prior work on the auxetic nature of these materials has been conducted and can accessed in a number of papers (17-19, 21, 22) and theses (36, 37). In these previous studies, the underlying cause of the auxetic response has been investigated (17, 21, 22) and the effects of alignment, phase and composition on the auxetic response has been recorded (17-19).

In an investigation by Wang *et al.* (17), the auxetic response of planar and homeotropic monodomain nematic LCEs were investigated, using LCEs of one composition (62 mol% mesogenic content); they recorded a strain threshold of the auxetic response for LCEs of planar (ε_x~ 0.58 ± 0.05) and homeotropic (ε_x~ 0.56 ± 0.05) alignment. Similarly, Berrow *et al.* (18) investigated the effect of the polymerization methodology on monodomain nematic LCEs and demonstrated that an alternative polymerization technique had no effect on the threshold strain of the auxetic response (for the two polymerization routes, they found a threshold of ε_x ~ 0.51 ± 0.05 and ε_x ~ 0.56 ± 0.05).

In further studies, Berrow *et al.* (19) demonstrated that the strain threshold of the monodomain nematic LCEs can in fact be tuned by varying the mesogenic side group component, whilst using a fixed mesogenic ratio of the LCE (62 mol% mesogenic content). They recorded the strain threshold for an LCE with 6OCB as ε_x ~ 0.56 ± 0.05, which agreed with the previous studies on this composition (17, 18), and they also found that the strain threshold could be slightly decreased to ε_x ~ 0.52 ± 0.05 for LCEs containing a side group of A4OCB (19). Interestingly, Berrow *et al.* did not observe an auxetic response in LCEs that exhibited a 'smectic-like' behaviour (19); this observation will be particularly relevant to our discussion.

In this investigation we will measure the auxetic response for a wide range of compositions at room temperature (22 °C), for five monodomain nematic LCEs with 56, 62, 64, 66, and 72 mol% mesogenic content. The in-house equipment used to conduct these measurements is known as the Microscope Elastomer Stress Strain

Enclosure (MESSE) and prior information on this technique can be found in Section 3.3.3

Figure 4.9 plots the strain in the axis of the thickness against the strain in the axis of the applied strain and allows us to observe the threshold strain for the auxetic response in monodomain nematic LCEs (17-19, 22). The threshold strains for all the LCEs are recorded in Table 4-3 and were calculated with polynomial fittings to find the Poisson's Ratio, as detailed in Section 3.3.3. The auxetic threshold data for the LCEs of 56 mol%, 62 mol%, and 64 mol% mesogenic content were collected by Stuart Berrow.

The threshold strain measured here for the 62 mol% mesogenic content LCE is a little low at $\varepsilon_x \sim 0.49 \pm 0.05$ but within the bounds of experimental error of the previous threshold strains that have been reported between $\varepsilon_x \sim 0.51 - 0.58$ (17-19). Intriguingly, in Table 4-3 we do see some evidence of a positive trend between the threshold strain and the mesogenic content of an LCE, however, more data is required for confirmation of a trend. We know that a change in the threshold strain with composition is indeed possible and was previously reported by Berrow *et al.,* with however a general decrease in the strain threshold seen for an increase in the side group spacer length from 4 to 6; this behaviour was attributed to the difference between the temperature of the experiment and the T_g of the material (19). In fact, we demonstrated previously (Figure 4.5) that the variation of the mesogenic content of nematic LCEs impacts the glass transition temperature, so it is probable that any trend in the threshold strain here is also influenced by the relative temperature to the T_g.

Interestingly, Berrow *et al.* (19) did not see an auxetic response at room temperature for mesogenic side group spacer lengths of 3, 7, 8, and 9; the LCE with a spacer length of 3 did not reach an auxetic threshold before the sample failed at a high strain (~ 120 %), whereas the longer spacer lengths of 7, 8, and 9 failed at low strains without exhibiting an auxetic response (~ 40 %). Crucially, here we did not observe an auxetic response for two materials which are at either end of the range of compositions investigated: nLCE-56 and nLCE-72. The reason behind a failed auxetic response is different for each material and so will each be discussed separately and within the context of the previous findings by Berrow *et al.* (19).

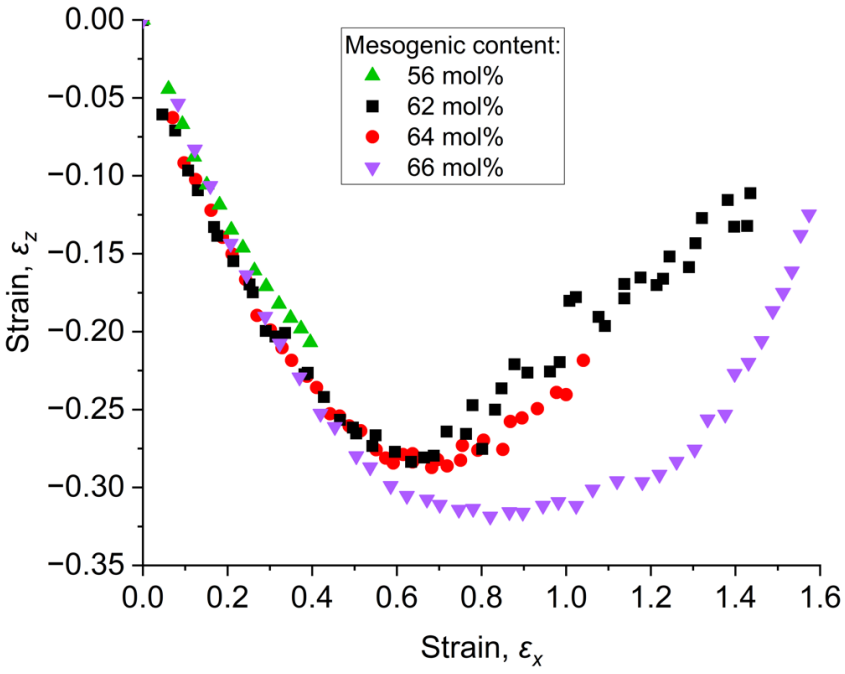

Figure 4.9. The auxetic behaviour of monodomain nematic LCEs within this acrylate family, shown for the strain in the direction of the sample thickness, ε_z, against the strain along the axis of the applied strain, ε_x. The auxetic threshold is seen to increase for the LCEs with increasing mesogenic content. The data for the LCEs of 56 mol% (green triangles), 62 mol% (black squares) and 64 mol% (red circles) mesogenic content was measured by Stuart Berrow.

We shall first discuss the failure of nLCE-56 in Figure 4.9. Interestingly, the T_g of this material is the lowest of all LCE compositions investigated and Berrow *et al.* showed that performing the threshold strain experiments at temperatures much higher than a material's T_g results in a lower strain threshold for auxetic behaviour (19). Following this argument, the auxetic response of this material at 22°C should occur at lower strains than the other materials investigated – however we see instead a failure of the material at low strains (~ 40%). To test whether an auxetic response for this material is achievable, the threshold strain should ideally be investigated at lower temperatures (below room temperature), however this is not possible to accomplish with the current experimental setup. In Section 3.2.1, it was shown that nematic LCEs with a lower mesogenic content exhibit various degrees of phase separation which places a limitation on the formation of a nematic phase; it is plausible that the failure of nLCE-56 is unconnected to the temperature of the experiment and is instead due to the material being too close to the formulation limitations of the nematic phase to successfully exhibit an auxetic response.

Table 4-3. The threshold strain for an auxetic response in monodomain nematic LCEs between 56 and 72 mol% mesogenic content was measured using the Microscope Elastomer Stress Strain Enclosure (MESSE). nLCE-56 and nLCE-72 did not exhibit an auxetic response before the materials failed. The data for nLCE-56, nLCE-62 and nLCE-64 were collected by Stuart Berrow.

Mesogenic Content of nLCE (± 1 mol %)	Threshold Strain (± 0.05)
56	N/A
62	0.49
64	0.52
66	0.63
72	N/A

Now, we shall discuss the material nLCE-72, which failed at even lower strains and the data were therefore not plotted in Figure 4.9. We have seen previously within this chapter that this material has shown good dissipative properties around room temperature (a high loss tangent in Figure 4.8) and so the material's failure at a low strain is surprising. Interestingly, Berrow *et al.* (19) attributed the failure of their materials at low strain to be due to a 'smectic-like' behaviour, showing that the auxetic nature is indeed limited to just monodomain nematic materials. We remain speculative about the cause of the failure of the auxetic response in nLCE-56 and nLCE-72, with a need to investigate the phases of these materials.

4.3.4 Comparing the Glass Transition Between Techniques.

We shall now return to the measurements of the glass transition temperature for each of the monodomain nematic LCEs of varied mesogenic content. A comparison between the glass transition temperatures that are measured using DMTA and the glass transition temperature measured from DSC can be seen in Figure 4.10, with a summary of all the T_g's in Table 4-4. Here we see an increase in the glass transition temperature for an increase in the mesogenic content, across all methodologies.

Table 4-4. The glass transition temperatures (T_g) for monodomain nematic LCEs of varied composition and measured using DMTA (from the loss modulus, the loss tangent, and an average) and using DSC.

	Glass Transition Temperature, T_g			
Composition of LCE	**DSC (± 0.6 °C)**	**DMTA: Loss Mod. (± 1 °C)**	**DMTA: Loss Tan. (± 1 °C)**	**DMTA: Average (± 1 °C)**
62	9.4	2	12	7
66	8.6	9	19	14
72	16.6	17	27	22

Lastly, we shall discuss the differences in the glass transition temperatures measured using the different techniques. Unsurprisingly, we once again observe that measurements of the glass transition temperature are highest when considering the peak of the loss tangent (DMTA). Converse to our previous findings, here we observe that the T_g for DSC varies between the samples, such that the DSC agrees best with the average DMTA for nLCE-62, but the DSC agrees best with the loss modulus for nLCE-66 and nLCE-72. In fact, we see that the T_g measured with DSC is the smallest across the methodologies for nLCE-66 and nLCE-72.

However, the variation in the agreement of the DSC to either the average DMTA or the loss modulus is not a concern; the average glass transition temperature using DMTA has no theoretical basis, and it was merely suggested previously (15) as a useful measure for comparison between DMTA and DSC.

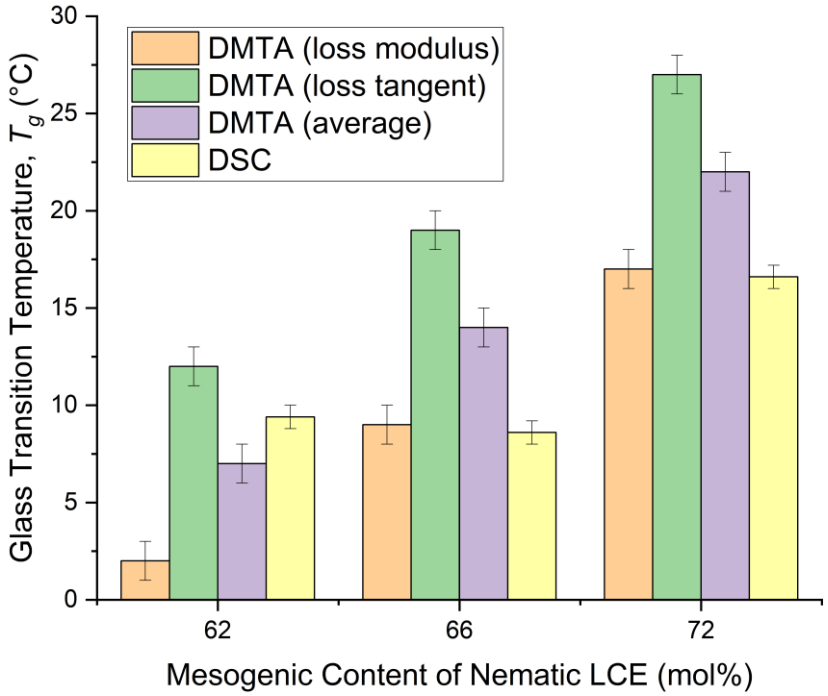

Figure 4.10. A comparison of the glass transition temperatures measured using different techniques for three different compositions of monodomain nematic LCEs: 62%, 66%, and 72% mesogenic content. The techniques used to measure the T_g include the peak of the loss modulus from DMTA, the peak of the loss tangent from DMTA, an average of these and finally the T_g measured with DSC.

4.4 Summary

Throughout this chapter, we have stressed the importance in understanding the thermal behaviour of a material within temperature windows that are relevant to potential applications. Indeed, LCEs have previously been shown to generally possess good energy dissipation around room temperature (9, 16), making these materials suitable for use in protective clothing (9, 10, 16). Furthermore, the family of LCEs that are investigated within this thesis are distinct in their ability to exhibit an auxetic response, which makes these particularly interesting candidates for impact resistant devices.

The work in this chapter has explored the role of templating and composition on the thermal and dissipative properties of a family of acrylate based LCEs, using Differential Scanning Calorimetry (DSC), Dynamic Mechanical Temperature Analysis (DMTA) and in-house equipment referred to as the Microscope Elastomer Stress Strain Enclosure (MESSE). A summary of all the results shall be provided accordingly.

A particular focus here was the glass transition temperature (T_g) of the LCEs and the various techniques that can measure this. In this work, the techniques of Differential Scanning Calorimetry (DSC) and Dynamic Mechanical Thermal Analysis (DMTA) were employed. Furthermore, three measures of the glass transition temperature with DMTA were used: the loss modulus peak, the loss tangent peak, and an average of these, which were then compared to the glass transition temperature measured with DSC. The DMTA loss tangent method consistently measured the largest transition temperature, as expected between the DMTA methods (14). Despite no theoretical basis for the DMTA average, there was some fair agreement observed between DSC and the average, particularly in the templating study. However, we also observed good agreement for DSC and the loss modulus in the composition studies.

We have demonstrated that DSC offers an interesting insight into the behaviour of the templates, revealing that the polydomain nematic and isotropic LCEs have astoundingly similar thermal behaviour across a wide temperature range and are clearly unalike from the general thermal behaviour seen for the monodomain nematic LCE. This distinct difference in the behaviour of the nematic templates was also established through observing an anisotropic and isotropic thermal shape change of the monodomain and polydomain templates, respectively.

We have measured the glass transition temperature for each of the templates using DSC and DMTA (using the loss modulus, loss tangent, and an average). These studies showed that the polydomain nematic LCE has the highest glass transition temperature, followed by the isotropic LCE and lastly, the monodomain nematic LCE. Previously, Jull *et al.* (25) found that an isotropic LCE had a higher degree of polymerization, ergo a higher transition temperature, when compared to a monodomain nematic LCE. Following this argument, we have evidence to suggest that the polydomain nematic LCE is capable of a slightly higher degree of polymerization than the isotropic LCE; to verify this, molecular simulation investigation would be necessary. Using DMTA, each template exhibited good dissipative capabilities, with a loss tangent > 1 around room temperature. However, only the monodomain nematic template displays an auxetic response and so the investigation into composition was limited to the monodomain nematic template.

To investigate the role of composition on the thermal properties of monodomain nematic LCEs, the nematic-to-isotropic transition temperatures (T_{NI}) of the precursor LCE mixtures and the glass transition temperatures of the corresponding polymerized LCEs was considered. For the range of compositions investigated using DSC, it was demonstrated that all precursor LCE mixtures have a T_{NI} above room temperature (lowest measured T_{NI} was 27.5°C for 76 mol% mesogenic content of precursor LCE mixture), which enables room temperature polymerization of the nematic templates. The T_g of the corresponding polymerized LCEs all demonstrated a T_g below room temperature (highest measured T_g was 16.3°C for nLCE-72); guaranteeing that all nematic LCEs are in a rubbery state at room temperature. Both transition temperatures ensure that a monodomain nematic material can be easily polymerized at room temperature and is then effective for rubbery applications at room temperature. Lastly, we observed an increase in both transition temperatures investigated with an increase in the mesogenic content, for all techniques used, and the trend is in line with previous literature with varying liquid crystalline content and crosslinker density of LCEs (24, 25).

The dissipative and auxetic properties of monodomain nematic LCEs were also investigated. Using DMTA, the dissipative capabilities of three materials (nLCE-62, nLCE-66, and nLCE-72) were focused on since these demonstrated maximum dissipation in the loss tangent around room temperature. In fact, nLCE-72 showed the highest dissipation out of these materials, however this maximum in dissipation was reached above room temperature (27°C); the material that provided the best dissipation at room temperature was nLCE-66 (peak at 19°C). However, to decide on the ideal composition for impact resistance, we must also consider the auxetic behaviour of these materials.

Through measurement of the threshold strain across the range of nLCE compositions, we see that nLCE-62 has the lowest threshold strain ($\varepsilon_x \sim 0.49$) which is within experimental error of previous reported strain thresholds for this composition (17-19), and therefore can more readily provide dissipation. We also observe an intriguing paradox; the nLCE with the greatest mesogenic content investigated (nLCE-72) had proved to have the greatest dissipation capabilities with DMTA but does not exhibit an auxetic behaviour. Likewise, an auxetic response was not observed with the lowest mesogenic content investigated (nLCE-56).

The present discussion has suggested that nLCE-56 and nLCE-72 may be at either end of the formulation limitations for a monodomain nematic LCE that can exhibit an auxetic response (at room temperature). We know from Section 3.2.1, that monodomain nematic LCEs cannot be formed with a mesogenic content lower than nLCE-56, because phase separation is observed; however, could there be an inadequate monodomain nematic phase for nLCE-56 to exhibit auxetic behaviour? The failure of nLCE-72 to exhibit an auxetic response is also intriguing. Berrow *et al.* (19) reported that a failed auxetic response within this family of acrylate LCEs was for materials that demonstrated a 'smectic-like' behaviour.

Clearly, the ordering of these materials must be investigated to understand the formulation limits of the monodomain nematic template of these acylate LCEs. Therefore, the next chapter, Chapter 5, will delve into the ordering of these LCEs and will also explore the network structure for each of these materials.

4.5 References

1. Cooper, E.J., Reynolds, M., Raistrick, T., Berrow, S.R., Jull, E.I.L., Reshetnyak, V., Mistry, D. and Gleeson, H.F. Controlling the Optical Properties of Transparent Auxetic Liquid Crystal Elastomers. *Macromolecules.* 2024, **57**(5), pp.2030-2038. Available from: https://doi.org/10.1021/acs.macromol.3c02226
2. He, Q., Wang, Z., Song, Z. and Cai, S. Bioinspired Design of Vascular Artificial Muscle. *Advanced Materials Technologies.* 2019, **4**(1), p.1800244. Available from: https://doi.org/10.1002/admt.201800244
3. Sun, D., Zhang, J., Li, H., Shi, Z., Meng, Q., Liu, S., Chen, J. and Liu, X. Toward Application of Liquid Crystalline Elastomer for Smart Robotics: State of the Art and Challenges. *Polymers.* 2021, **13**(11). Available from: https://doi.org/10.3390/polym13111889
4. Camacho-Lopez, M., Finkelmann, H., Palffy-Muhoray, P. and Shelley, M. Fast liquid-crystal elastomer swims into the dark. *Nature Materials.* 2004, **3**(5), pp.307-310. Available from: https://doi.org/10.1038/nmat1118
5. Feng, W., Broer, D.J. and Liu, D. Oscillating Chiral-Nematic Fingerprints Wipe Away Dust. *Advanced Materials.* 2018, **30**(11), p.1704970. Available from: https://doi.org/10.1002/adma.201704970

6. Bera, T., Malcuit, C., Clements, R.J. and Hegmann, E. Role of Surfactant during Microemulsion Photopolymerization for the Creation of Three-Dimensional Liquid Crystal Elastomer Microsphere Spatial Cell Scaffolds. *Frontiers in Materials.* 2016, **3**(31). Available from: https://doi.org/10.3389/fmats.2016.00031

7. Sharma, A., Neshat, A., Mahnen, C.J., Nielsen, A.d., Snyder, J., Stankovich, T.L., Daum, B.G., LaSpina, E.M., Beltrano, G., Gao, Y., Li, S., Park, B.-W., Clements, R.J., Freeman, E.J., Malcuit, C., McDonough, J.A., Korley, L.T.J., Hegmann, T. and Hegmann, E. Biocompatible, Biodegradable and Porous Liquid Crystal Elastomer Scaffolds for Spatial Cell Cultures. *Macromolecular Bioscience.* 2015, **15**(2), pp.200-214. Available from: https://doi.org/10.1002/mabi.201400325

8. Hussain, M., Jull, E.I.L., Mandle, R.J., Raistrick, T., Hine, P.J. and Gleeson, H.F. Liquid Crystal Elastomers for Biological Applications. *Nanomaterials.* 2021, **11**(3), p.813. Available from: https://doi.org/10.3390/nano11030813

9. Guo, H., Terentjev, A., Saed, M.O. and Terentjev, E.M. Momentum transfer on impact damping by liquid crystalline elastomers. *Scientific Reports.* 2023, **13**(1), p.10035. Available from: https://doi.org/10.1038/s41598-023-37215-9

10. Clarke, S.M., Tajbakhsh, A.R., Terentjev, E.M., Remillat, C., Tomlinson, G.R. and House, J.R. Soft elasticity and mechanical damping in liquid crystalline elastomers. *Journal of Applied Physics.* 2001, **89**(11), pp.6530-6535. Available from: https://doi.org/10.1063/1.1368177

11. Mistry, D., Nikkhou, M., Raistrick, T., Hussain, M., Jull, E.I.L., Baker, D.L. and Gleeson, H.F. Isotropic Liquid Crystal Elastomers as Exceptional Photoelastic Strain Sensors. *Macromolecules.* 2020, **53**(10), pp.3709-3718. Available from: https://doi.org/10.1021/acs.macromol.9b02456

12. Li, L., Bai, H., Dong, X., Jiang, Y., Li, Q., Wang, Q., Yuan, N. and Ding, J. Flexible Capacitive Sensors Based on Liquid Crystal Elastomer. *Langmuir.* 2023, **39**(35), pp.12412-12419. Available from: https://doi.org/10.1021/acs.langmuir.3c01593

13. Campo, E.A. 1 - Polymeric Materials and Properties. In: Campo, E.A. ed. *Selection of Polymeric Materials*. Norwich, NY: William Andrew Publishing, 2008, pp.1-39.

14. Whitcomb, K. *Measurement of Glass Transition Temperatures by Dynamic Mechanical Analysis and Rheology.* [Online]. TA Instruments. Available from: https://www.tainstruments.com/applications-notes/

15. Achorn, P.J. and Ferrillo, R.G. Comparison of thermal techniques for glass transition measurements of polystyrene and cross-linked acrylic polyurethane films. *Journal of Applied Polymer Science.* 1994, **54**(13), pp.2033-2043. Available from: https://doi.org/10.1002/app.1994.070541305

16. Mistry, D., Traugutt, N.A., Sanborn, B., Volpe, R.H., Chatham, L.S., Zhou, R., Song, B., Yu, K., Long, K.N. and Yakacki, C.M. Soft elasticity optimises dissipation in 3D-printed liquid crystal elastomers. *Nature Communications.* 2021, **12**(1), p.6677. Available from: https://doi.org/10.1038/s41467-021-27013-0

17. Wang, Z., Raistrick, T., Street, A., Reynolds, M., Liu, Y. and Gleeson, H.F. Direct Observation of Biaxial Nematic Order in Auxetic Liquid Crystal Elastomers. *Materials.* 2022, **16**(1). Available from: https://doi.org/10.3390/ma16010393

18. Berrow, S.R., Mandle, R.J., Raistrick, T., Reynolds, M. and Gleeson, H.F. Toward Monodomain Nematic Liquid Crystal Elastomers of Arbitrary Thickness through PET-RAFT Polymerization. *Macromolecules.* 2024, **57**(11), pp.5218-5229. Available from: https://doi.org/10.1021/acs.macromol.4c00245

19. Berrow, S.R., Raistrick, T., Mandle, R.J. and Gleeson, H.F. Structure–Property Relationships in Auxetic Liquid Crystal Elastomers—The Effect of Spacer Length. *Polymers.* 2024, **16**(14), p.1957. Available from: https://www.mdpi.com/2073-4360/16/14/1957

20. Moorhouse, T. and Raistrick, T. Sub-Micron Diffractive Optical Elements Facilitated by Intrinsic Deswelling of Auxetic Liquid Crystal Elastomers. *Advanced Optical Materials.* 2024, **12**(24), p.2400866. Available from: https://doi.org/10.1002/adom.202400866

21. Raistrick, T., Zhang, Z., Mistry, D., Mattsson, J. and Gleeson, H.F. Understanding the physics of the auxetic response in a liquid crystal elastomer. *Physical Review Research.* 2021, **3**(2), p.023191. Available from: https://doi.org/10.1103/PhysRevResearch.3.023191

22. Mistry, D., Connell, S.D., Mickthwaite, S.L., Morgan, P.B., Clamp, J.H. and Gleeson, H.F. Coincident molecular auxeticity and negative order parameter in a liquid crystal elastomer. *Nature Communications.* 2018, **9**(1), p.5095. Available from: https://doi.org/10.1038/s41467-018-07587-y

23. Mistry, D., Morgan, P.B., Clamp, J.H. and Gleeson, H.F. New insights into the nature of semi-soft elasticity and "mechanical-Fréedericksz transitions" in liquid crystal elastomers. *Soft Matter.* 2018, **14**(8), pp.1301-1310. Available from: https://doi.org/10.1039/C7SM02107K

24. Barnes, M., Cetinkaya, S., Ajnsztajn, A. and Verduzco, R. Understanding the effect of liquid crystal content on the phase behavior and mechanical properties of liquid crystal elastomers. *Soft Matter.* 2022, **18**(27), pp.5074-5081. Available from: https://doi.org/10.1039/D2SM00480A

25. Jull, E.I.L., Mandle, R.J., Raistrick, T., Zhang, Z., Hine, P.J. and Gleeson, H.F. Toward In Silico Design of Highly Tunable Liquid Crystal Elastomers. *Macromolecules.* 2022, **55**(11), pp.4320-4330. Available from: https://doi.org/10.1021/acs.macromol.2c00587

26. Broer, D.J. and Mol, G.N. Anisotropic thermal expansion of densely cross-linked oriented polymer networks. *Polymer Engineering & Science.* 1991, **31**(9), pp.625-631. Available from: https://doi.org/10.1002/pen.760310902

27. Chartoff, R.P., Menczel, J.D. and Dillman, S.H. Dynamic Mechanical Analysis (DMA). In: *Thermal Analysis of Polymers*. 2009, pp.387-495.

28. Traugutt, N.A., Volpe, R.H., Bollinger, M.S., Saed, M.O., Torbati, A.H., Yu, K., Dadivanyan, N. and Yakacki, C.M. Liquid-crystal order during synthesis affects main-chain liquid-crystal elastomer behavior. *Soft Matter.* 2017, **13**(39), pp.7013-7025. Available from: https://doi.org/10.1039/C7SM01405H

29. Luo, C., Chung, C., Traugutt, N.A., Yakacki, C.M., Long, K.N. and Yu, K. 3D Printing of Liquid Crystal Elastomer Foams for Enhanced Energy Dissipation Under Mechanical Insult. *ACS Applied Materials & Interfaces.* 2021, **13**(11), pp.12698-12708. Available from: https://doi.org/10.1021/acsami.0c17538

30. Street, A., Mistry, D., Mattsson, J. and Gleeson, H.F. The Gripping Case of Geometry-Dependent Adhesion in Monodomain Liquid Crystal Elastomers. *Paper in Preparation.* 2025.

31. Maier, W. and Saupe, A.Z. Eine einfache molekulare Theorie des nematischen kristallinflüssigen Zustandes. *Naturforsch.* 1958, **13a**, pp.564-566.
32. Maier, W. and Saupe, A.Z. Eine einfache molekular-statistische Theorie der nematischen kristallinflüssigen Phase. Teil 1[1]. *Naturforsch.* 1959, **14a**, pp.882–889.
33. Maier, W. and Saupe, A.Z. Eine einfache molekular-statistische Theorie der nematischen kristallinflüssigen Phase. Teil II. *Naturforsch.* 1960, **15a**, pp.287–292.
34. de Gennes, P.G. and Prost, J. *The Physics of Liquid Crystals.* Oxford University Press, 1993.
35. Makhlouf, A.S.H. ed. *Handbook of Smart Coatings for Materials Protection.* Amsterdam: Woodhead Publishing Limited, 2014.
36. Raistrick, T. *Understanding the mechanical behaviour of novel liquid crystal elastomers*. PhD thesis, University of Leeds, 2022.
37. Mistry, D. *Synthetic lenses for the ageing eye: a motivation for developing the mechanical applications of Liquid Crystal Elastomers*. PhD thesis, University of Leeds, 2018.

Chapter 5 The Order and Structure of Liquid Crystalline Elastomers

A proportion of the order parameter work in this chapter has previously been published in (1):

Emily J. Cooper, *et al*. "*Controlling the Optical Properties of Transparent Auxetic Liquid Crystal Elastomers"*. Macromolecules, 2024, **57**(5), 2030-2038.

Figures that have been published will be stated in the caption. Any experimental work that was not performed by the author, Emily Jane Cooper, will be stated in the text or the figure caption.

5.1 Introduction

The overarching aim throughout this thesis is to understand the physics of a family of acrylate based LCEs, in order to provide design rules for the fabrication of these materials and to optimise their properties for specific applications. A complete comprehension of the physics behind these auxetic materials will be achieved through the characterization of the mechanical, optical, and thermal properties of a series of LCEs with varied compositions.

The role of composition on the liquid crystalline network properties, such as the transition temperatures and the order parameters, has been shown in literature with the control of the crosslinker density (2-5), the concentration of mesogenic components (1, 6), and the use of different mesogenic components (7, 8). In the previous chapter, we sought to understand the impact of both templating and composition on the thermal, mechanical, and dissipative properties of the network. This chapter will predominantly focus on understanding the underlying order and structure that is locked into the LCEs upon polymerization and how these are influenced by compositional changes of the network.

In this chapter, the order parameters of monodomain nematic LCEs are measured with Raman Spectroscopy and X-ray Scattering and will largely show a good agreement in $\langle P_2 \rangle$, however some deviation in $\langle P_4 \rangle$. Furthermore, we will generally observe good agreement of the order parameters measured with Raman Spectroscopy to a commonly used mean field theory, but the order parameters

measured with X-ray Scattering will be seen to be lower than the theory; this finding is similar to previous reports across other liquid crystalline systems (9-12).

We will then demonstrate that the thermal shape change of the monodomain nematic LCEs shows good agreement with the expected shape change using the temperature-dependent order parameter, in line with previous literature (13). Lastly, X-ray scattering is used to identify the structure of these materials and will show the existence of several scattering features aligned parallel and perpendicular to the director. The mesogenic content of the LCEs will be shown to have an influence on the overall network structure and the scattering intensity. Interestingly, a reduction in the network spacings with an increased mesogenic content of the LCEs was detected. These results signify a closer packing of the network and correspond to a measurable increase in density of ~ 4% for a 16 mol% increase in mesogenic content.

5.2 The Order Parameters

5.2.1 The Formulation Limitations of Nematic LCEs

Raman Spectroscopy has frequently been used to determine the order parameters for this family of sidechain acylate LCEs and has been instrumental in describing their highly ordered nature (1, 14-16). A complete description of this technique can be accessed in Sections 2.4 and 3.4.1.

For LCEs polymerised in the nematic phase (nLCEs), the magnitude of the resultant order parameters is expected to be dependent on both the material formulation and the temperature (with respect to T_{NI}) at which the system was polymerised; the latter being consistent with Broer *et al.*'s findings for glassy liquid crystalline networks (17). To explore this, we first consider how the order parameters of the nLCEs vary with composition over a wide range of mesogenic content, using Raman Spectroscopy to provide formulation limitations for the nematic LCEs.

The order parameters, $\langle P_2 \rangle$ and $\langle P_4 \rangle$, were determined using Raman Spectroscopy for monodomain nematic LCEs of varied mesogenic content and were all measured at room temperature (22 ± 1°C). In Figure 5.1, the order parameters are seen to increase with an increase in the mesogenic content. This is consistent with a greater difference between the polymerisation temperature and the precursor LCE

mixture's T_{NI} (higher mesogenic content results in a higher T_{NI} - as shown in Section 4.3). All measured order parameters can be found in Table 5-2, which also includes order parameters that are later measured using an alternative technique of X-ray Scattering.

The order parameter data in Figure 5.1 can be explained in detail by considering an analogy with the more commonly explored temperature dependence that is described by well-known Onsager type models, such as the Haller model (18). The Haller model was introduced in Section 2.4 and a recap of the Haller model equation is given in Equation 5-1.

$$\langle P_2 \rangle = \left(1 - \frac{T}{T^*}\right)^{\tau} \qquad \textit{Equation 5-1}$$

In Equation 5-1, T is the temperature, T^* is a critical temperature, typically just above T_{NI}, and τ is an exponent fitting constant. A similar approach can be invoked that describes how the scalar order parameter depends on the concentration, c, of a non-mesogenic component,

$$\langle P_2 \rangle = A \times \left(1 - \frac{c}{c^*}\right)^{\tau} \qquad \textit{Equation 5-2}$$

where $c^*$is a critical concentration above which the system is isotropic, τ is an exponent fitting constant, and A is the upper limit of the order parameter for a maximum mesogenic content LCE (0 mol% EHA). Such a model has been similarly used by Barbero *et al.* to describe the dependence of order in liquid crystal systems undergoing a cis-trans isomerisation of azobenzene groups (19). We have adapted the approach by Barbero *et al.* and use Equation 5-2 to analyse the dependence of the monodomain nematic LCE order parameters, $\langle P_2 \rangle$ and $\langle P_4 \rangle$, on the concentration of the non-mesogenic groups. In our approach, the parameter A physically corresponds to the order parameter that an LCE with no EHA content (i.e., 100% mesogenic content), would be expected to have.

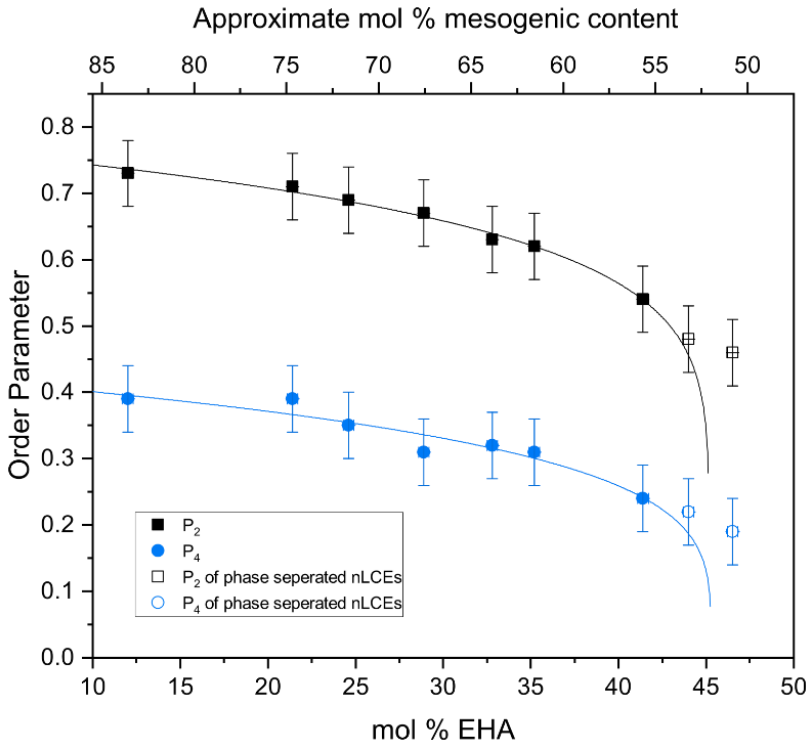

Figure 5.1. The order parameters of monodomain nematic LCEs (nLCEs) plotted both as a function mol% of non-mesogenic component, EHA, (lower axis) and the approximate mol% of mesogenic content (upper axis). The fit to the data uses Equation 5-2 and is applied to only data where no phase separation was observed (< 45 mol% EHA). The nLCE-75 and nLCE-84 materials used above were synthesised by Matthew Reynolds.

As discussed previously (see Section 3.2.1), there is a lower limit of mesogenic content in the monodomain nematic LCEs, below which phase separation is observed; these are indicated in Figure 5.1 with open symbols. The adapted Haller fittings in Figure 5.1 were only performed using the LCEs that did not exhibit phase separation. The parameters A, c^* *and* τ found from fitting Equation 5-2 to $\langle P_2 \rangle$ and $\langle P_4 \rangle$ against mol. % EHA as in Figure 5.1, are given in Table 5-1. Interestingly, the fits to both $\langle P_2 \rangle$ and $\langle P_4 \rangle$ provide a consistent value for the critical concentration, c^* of 45 mol% EHA (55 mol% mesogenic content), which is in excellent agreement with the experimental observation that nLCEs fabricated with a mesogenic content below ~ 55 mol% exhibit phase separation (seen for nLCE-51 and nLCE-53).

Table 5-1. The fitting parameters, A, c^*, and τ, for both $\langle P_2 \rangle$ and $\langle P_4 \rangle$ according to Equation 5-2 (the fittings are shown in Figure 5.1).This data has been published by Cooper et al. (1).

	Fitting Parameters		
Order Parameter	A	c^*	τ
$\langle P_2 \rangle$	0.77 ± 0.01	45 ± 1	0.14 ± 0.02
$\langle P_4 \rangle$	0.42 ± 0.03	45 ± 5	0.2 ± 0.1

For a Haller fitting to a temperature-dependent order parameter (Equation 5-1), the fitting exponent, τ, is typically found to be within a narrow range (0.17-0.23) for various materials (18). As shown in Table 5-1, the adapted Haller fitting for concentration (Equation 5-2) gives values for the exponent of $\tau = 0.14 \pm 0.02$ for $\langle P_2 \rangle$ and $\tau = 0.2 \pm 0.1$ for $\langle P_4 \rangle$. Interestingly, we observe similar values for the exponent (τ) of the adapted Haller model when compared to the Haller model, despite the different independent variables used.

Lastly, the values of $\langle P_2 \rangle$ and $\langle P_4 \rangle$ for the standard and phase separated monodomain nematic LCEs can be compared to Maier-Saupe theory (20-24), which is a frequently used mean field theory for liquid crystalline materials. The well-formed monodomain nematic LCEs (filled black squares) can be seen in Figure 5.2 to demonstrate a good agreement to Maier-Saupe theory (green line), particularly for the materials with higher order parameters. However, we do observe some deviation from the mean field theory in the phase separated LCEs with lower order parameters (empty squares).

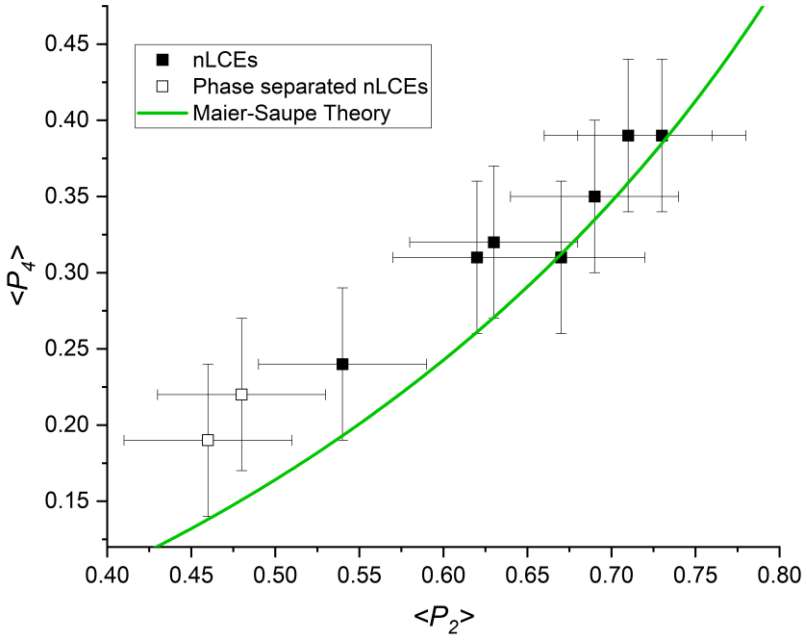

Figure 5.2. A comparison of the order parameters, $\langle P_2 \rangle$ and $\langle P_4 \rangle$, measured using Raman Spectroscopy for monodomain nematic LCEs (filled black squares) and phase separated nematic LCEs (empty black square). The nematic LCEs demonstrate a good agreement to Maier-Saupe theory (20-24). For reference, nLCE-51 can be seen as the leftmost data point, nLCE-84 is the rightmost data point. nLCE-75 and nLCE-84 were synthesised by Matthew Reynolds. The Maier-Saupe theory fitting was provided by Thomas Raistrick. This figure has been published by Cooper et al. (1).

5.2.2 A Comparison of Raman Spectroscopy and X-ray Scattering

In this thesis so far, we have measured the order parameters of monodomain nematic LCEs using only Raman Spectroscopy. However, the technique of X-ray scattering is also often used for measuring the order parameters of liquid crystalline materials and polymeric networks and is capable of effectively quantifying both $\langle P_2 \rangle$ and $\langle P_4 \rangle$ (11). The detailed method to extract the order parameters from Wide-Angle X-ray Scattering (WAXS) is described in Section 2.4.1 and the experimental technique is provided in Section 3.4.2. In brief, the order parameter is extracted using the Kratky method (12, 25) fitted to the scattering intensity of the anisotropic feature at a reciprocal space of $q \sim 14$ nm^{-1}.

The order parameters extracted from Raman Spectroscopy and X-ray Scattering techniques should hypothetically agree however, discrepancies arise in practice depending on the methodology used. Previously, Sanchez-Castillo *et al.* (11) compared the order parameters extracted for 5CB using Raman Spectroscopy and

X-ray Scattering and found both of these techniques demonstrated a good agreement for values of $\langle P_2 \rangle$ to the mean field theory of Maier-Saupe (20-22), however they observed deviations in the behaviour of $\langle P_4 \rangle$ (11). Hence, we shall compare the order parameters of monodomain nematic LCEs determined using both Raman Spectroscopy and WAXS, which is a comparison that has not previously been reported for LCEs to the best of this author's knowledge.

To enable a comparison between these techniques, a range of monodomain nematic LCEs were selected between 56 and 72 mol% mesogenic content. Due to time constraints for WAXS, we investigated a smaller range of LCE compositions than were previously investigated with Raman Spectroscopy; thus, the LCEs with a higher mesogenic content (nLCE-75 and nLCE-84) are excluded from the comparison of these techniques. Additionally, this investigation will not include the phase separated LCEs, due to the difficulty in ensuring that only the transparent (monodomain nematic) region is probed with the X-ray beam.

The WAXS on the LCEs was conducted within a vacuum chamber at temperatures recorded to be between 28°C and 29°C, whereas Raman Spectroscopy was undertaken at room temperature (22 ± 1°C). Therefore, before comparing the order parameters measured using these techniques, the effect of temperature on the order parameters needs to be characterized using a single material (nLCE-62). Using only Raman Spectroscopy, since this technique is easier to investigate with temperature control in our laboratories, $\langle P_2 \rangle$ was recorded to decrease by 0.04 and $\langle P_4 \rangle$ by 0.02 for a 5°C temperature increase (25°C to 30°C), which are both within the accepted experimental error of ± 0.05. Therefore, we can determine that relatively small deviations in temperature are accounted for within the order parameter error whilst around room temperature.

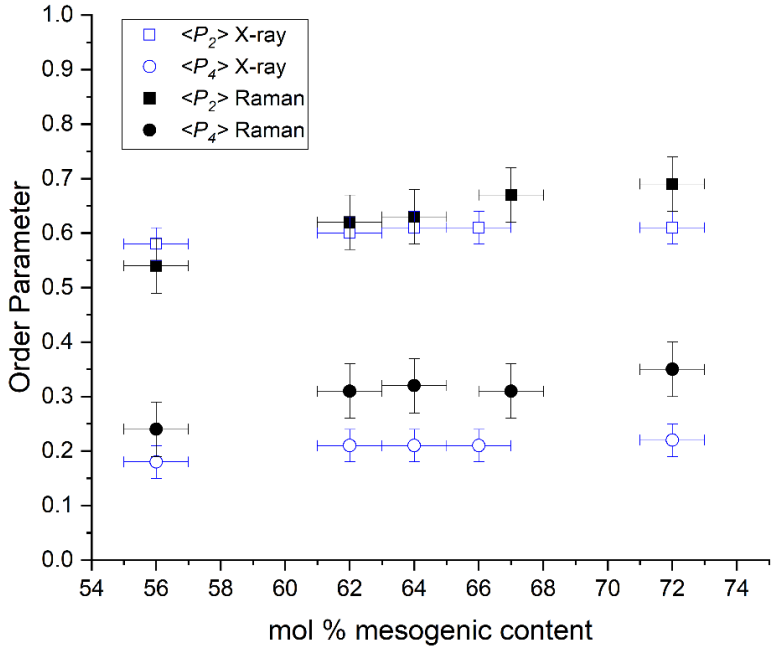

Figure 5.3. A comparison of the order parameters, $\langle P_2 \rangle$ and $\langle P_4 \rangle$, measured using Raman Spectroscopy and WAXS (X-ray) for monodomain nematic LCEs. There is a good agreement between $\langle P_2 \rangle$ measured with Raman Spectroscopy and WAXS, however we observe consistently lower $\langle P_4 \rangle$ with WAXS. The Raman Spectroscopy data has been published previously by Cooper et al. (1).

In Figure 5.3, the order parameters measured with Raman Spectroscopy and WAXS demonstrate a good agreement between $\langle P_2 \rangle$, albeit with slightly lower values generally measured with WAXS. However, a clear deviation is seen between these techniques for $\langle P_4 \rangle$. In fact, the $\langle P_2 \rangle$ and $\langle P_4 \rangle$ values deduced from WAXS are lower than the values found with Raman Spectroscopy by up to 0.08 in $\langle P_2 \rangle$ and 0.13 in $\langle P_4 \rangle$.

Since we have determined that the temperature difference between the methodologies has a negligible impact on the measured order parameters, the significantly lower values of $\langle P_4 \rangle$ in WAXS must therefore have an alternative cause; we will now turn to literature to obtain a solution. Previous comparisons of Raman Spectroscopy and WAXS have shown that $\langle P_4 \rangle$ is consistently measured lower with WAXS and this trend is pronounced across a range of liquid crystalline materials and phases (9-12).

The values of $\langle P_2 \rangle$ against $\langle P_4 \rangle$ for both techniques can be plotted and compared to the Maier-Saupe theory in a temperature-independent way (20-24), in a similar manner to Raistrick *et al.* (9). Investigating the order parameters in this manner highlights that the order parameters measured using WAXS fall below the Maier-

Saupe theory with systematically lower values of $\langle P_4 \rangle$ (Figure 5.4). Nevertheless, both techniques still demonstrate a good agreement to Maier-Saupe theory, as shown in Figure 5.4.

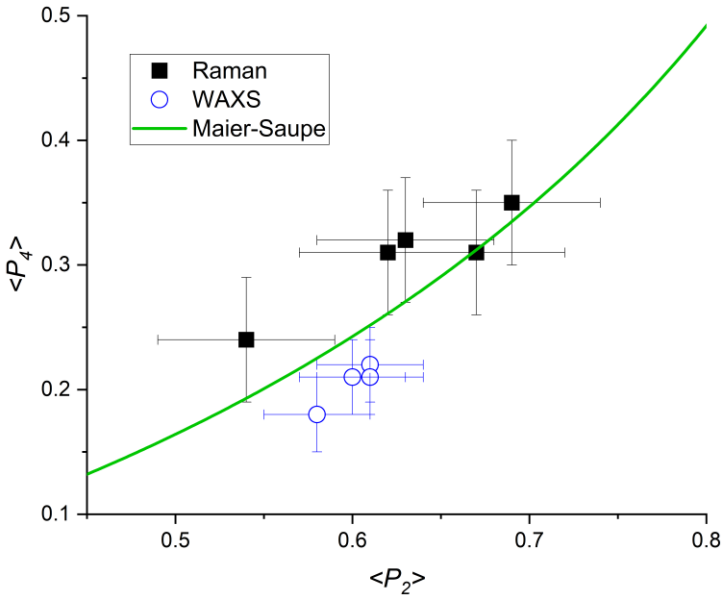

Figure 5.4. A comparison of the order parameters, $\langle P_2 \rangle$ and $\langle P_4 \rangle$, measured for monodomain nematic LCEs using Raman Spectroscopy (filled black squares) and Wide-Angle X-ray Scattering, WAXS (empty blue circles). The order parameters measured with Raman Spectroscopy and WAXS demonstrate good agreement to Maier-Saupe theory (green line) (20-24). Only four WAXS data points are observable, since nLCE-64 and nLCE-66 have the same values of $\langle P_2 \rangle$ and $\langle P_4 \rangle$. The Maier-Saupe theory fitting was provided by Thomas Raistrick. The Raman Spectroscopy data has previously been published by Cooper et al. (1).

A summary of all the order parameters measured using Raman Spectroscopy and X-ray Scattering throughout this section are summarised in Table 5-2 below. This table includes the monodomain nematic LCEs whose order parameters can be compared between both techniques (56 - 72 mol% mesogenic content), as well as the phase separated LCEs (nLCE-51 and nLCE-53) that were investigated solely with Raman Spectroscopy.

In the next section of this chapter, we will compare the order parameter $\langle P_2 \rangle$ to the thermal shape change of the monodomain nematic LCEs, to further reveal the relationship between the order parameter, the observed thermal shape change, and the glass transition temperature.

Table 5-2. The measured order parameters, $\langle P_2 \rangle$ and $\langle P_4 \rangle$, for monodomain nematic LCEs of varied mesogenic content using Raman Spectroscopy and X-ray Scattering techniques. The nLCE-51 and nLCE-53 exhibited phase separation and so were excluded from the X-ray Scattering study. nLCE-75 and nLCE-84 were synthesised by Matthew Reynolds. The Raman Spectroscopy data has been published by Cooper et al. (1).

Mesogenic Content of nLCEs (± 1 mol %)	**Raman Spectroscopy (± 0.5)**		**X-ray Scattering (± 0.3)**	
	$\langle P_2 \rangle$	$\langle P_4 \rangle$	$\langle P_2 \rangle$	$\langle P_4 \rangle$
51	0.46	0.19		
53	0.48	0.22		
56	0.54	0.24	0.58	0.18
62	0.62	0.31	0.6	0.21
64	0.63	0.32	0.61	0.21
66			0.61	0.21
67	0.67	0.31		
72	0.69	0.35	0.61	0.22
75	0.71	0.39		
84	0.73	0.39		

5.3 The Thermal Shape Change of LCEs

The shape changing properties of a liquid crystalline network to a temperature stimulus have often been reported in accompaniment to the measurement of material properties such as the order parameter and the phase transition behaviour (2, 8, 13, 26-28). In fact, the thermal shape change response of a liquid crystalline network observed above T_g is well-understood to be related to the order parameter of the network. Broer *et al.* (13) have previously shown that the thermal shape change can be predicted from the temperature-dependent order parameter.

In this section, we will ascertain the role of the mesogenic content on the thermal shape change and tease out further information about the temperature-dependent order of these materials. The thermal response of these LCEs is investigated below and compared to the predicted response using the measured order parameters.

5.3.1 The Role of the Glass Transition Temperature

Previously in Section 4.3, the influence of the composition on the physical and thermal properties of LCEs was explored with a focus on three monodomain nematic LCEs (nLCE-62, nLCE-66, and nLCE-72), since these materials demonstrated optimal mechanical properties (large peaks in the loss tangent) around room temperature. We will now investigate the thermal shape change properties of these three LCEs, using small samples with dimensions perpendicular (L_{perp}) and parallel (L_{para}) to the director and placed on a small amount of silicon oil covering a glass slide.

This investigation is like the previous study in Section 4.2.1 (Figure 4.2), in which the thermal shape changes of a monodomain nematic LCE and a polydomain nematic LCE of the same composition were compared. The full methodology can be found in Section 3.3.4

The relative length changes, $\Delta L/L_0$, perpendicular and parallel to the director for the LCEs are shown in Figure 5.5, where L_0 is defined as the length along the axis at 25°C (13). Similar to existing literature (2, 8, 13, 26-28), we observe anisotropic changes to the material dimensions due to a loss of order along the director, which manifests as a decrease in length parallel and an increase in length perpendicular to the director.

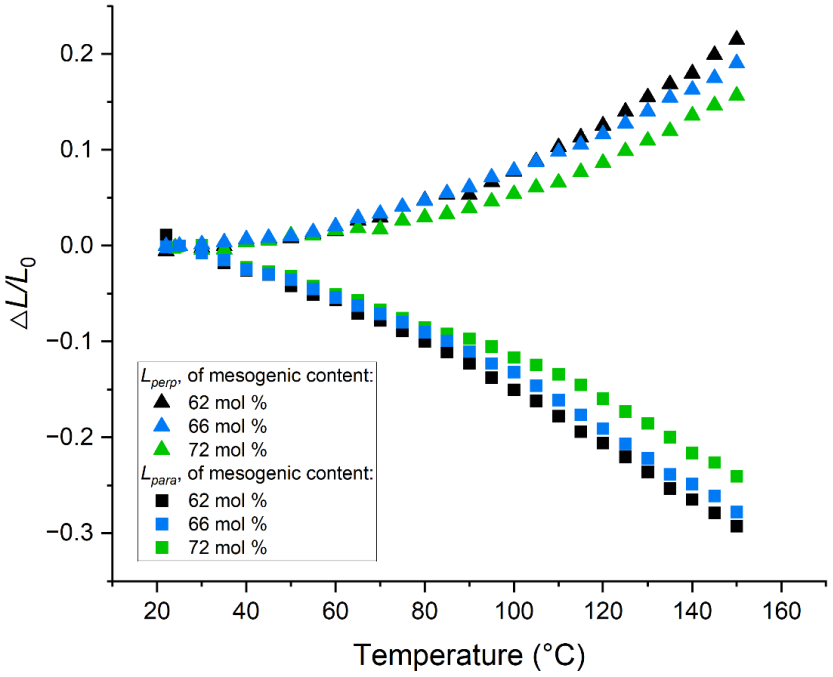

Figure 5.5. The dimension changes between 22°C and 150°C for monodomain nematic LCEs of varied composition: with 62 mol% (black), 66 mol% (blue), and 72 mol% (green) mesogenic content for lengths perpendicular (L_{perp} - triangles) and parallel (L_{para} - squares) to the director.

In Figure 5.5, there are different onset temperatures of the material's shape change depending on the mesogenic content; this is likely due to the different glass transition temperatures, T_g, of each of the materials. This can be investigated further through comparison of $\Delta L/L_0$ for each network against a reduced temperature, defined here as $T - T_g$, which enables the comparison of the shape changes at the same relative temperature to T_g. For the calculation of a reduced temperature, $T - T_g$, we will use the glass transition temperature measured as the peak in the loss tangent with DMTA. Previously in Sections 4.2.3 and 4.3.4, the measured glass transition temperatures were shown to depend on the technique used (DSC and DMTA), which is in line with findings throughout literature; it is well known that the glass transition temperature varies depending on the material property probed and the methodology used (29).

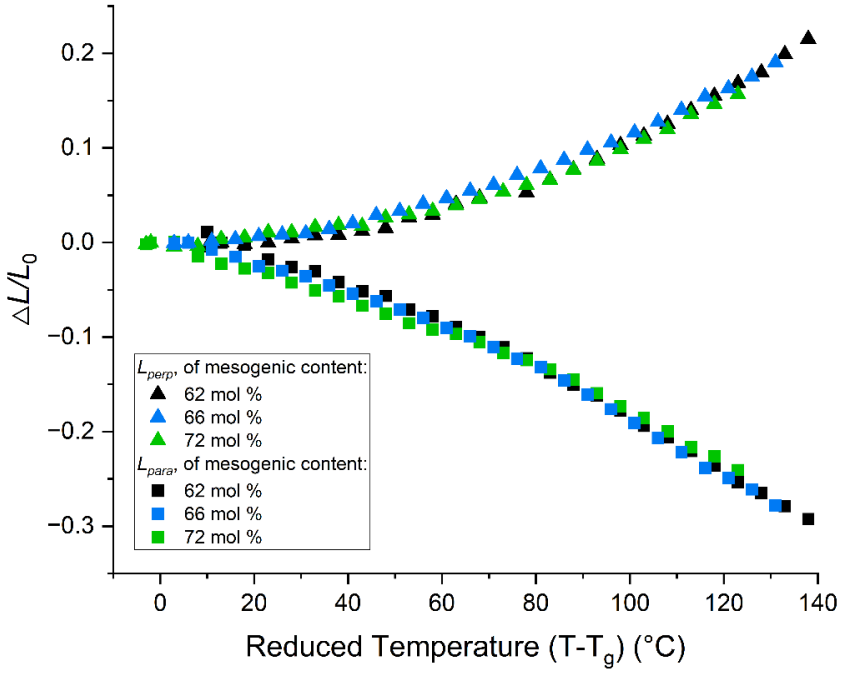

Figure 5.6. The dimension changes against the reduced temperature ($T - T_g$) for monodomain nematic LCEs of varied composition: with 62 mol% (black), 66 mol% (blue), and 72 mol% (green) mesogenic content for lengths perpendicular (L_{perp} - triangles) and parallel (L_{para} - squares) to the director. The reduced temperature uses the glass transition temperature measured as the peak in the loss tangent with DMTA.

Remarkably, we see from Figure 5.6 that there is a strong overlap in the shape changes for each composition, when mapping the shape changes against a reduced temperature. This behaviour indicates that the relative temperature to T_g is fundamental to the onset of the LCE shape change response.

5.3.2 The Order Parameter and the Shape Change Response

Previous investigations into the shape change response of a liquid crystalline network often relate the observed change in length with the measured order parameters. Equation 5-3 by Broer *et al*. shows how the length change ($\Delta L/L_0$) can be predicted for the axis parallel to the director, where $\langle P_2 \rangle_T$ is the order parameter measured at temperatures, T, and $\langle P_2 \rangle_0$ is the order parameter measured at 25°C (13).

$$\frac{\Delta L}{L_0} = \left[\frac{2(\langle P_2\rangle_T - \langle P_2\rangle_0)}{2\langle P_2\rangle_0 + 1} + 1\right]^{1/2} - 1 \qquad \textit{Equation 5-3}$$

The temperature-dependent order parameter of a single monodomain nematic LCE (nLCE-62) was investigated using Raman Spectroscopy and Equation 5-3, to verify whether the observed length change ($\Delta L/L_0$) agrees with the order parameter as predicted. The method used for measuring the temperature-dependent order parameter is similar to the method previously used for Raman Spectroscopy, with the additional step of placing the sample on a glass coverslip coated with a small amount of silicon oil to prevent contact between the surfaces. The coverslip was then placed on a Linkam HFS600 hot stage connected to a Linkam TMS 94 controller to regulate the temperature. Incidentally, the temperature-dependent order parameter will be provided in full later in Chapter 7, since the raw data is not relevant to this discussion.

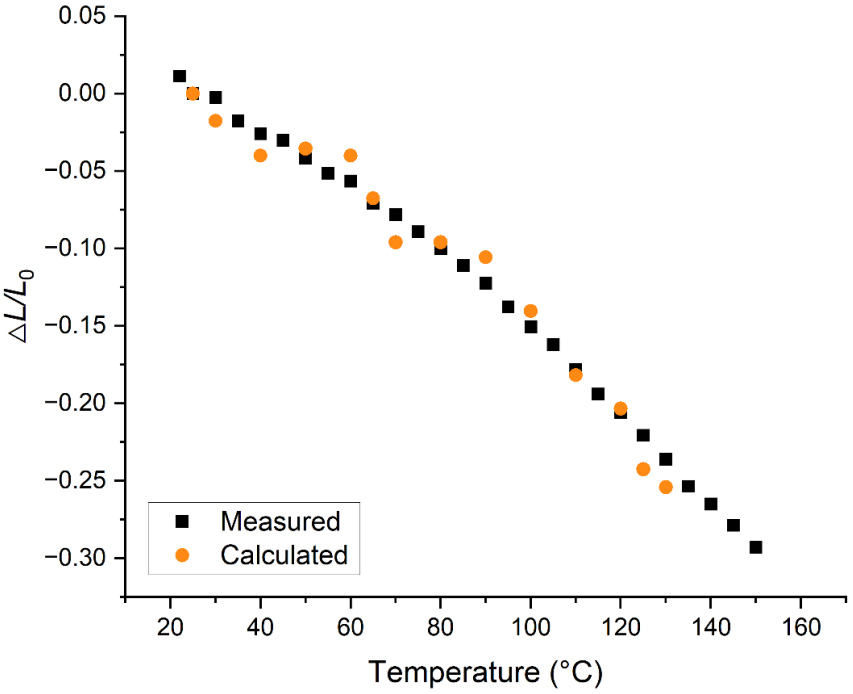

Figure 5.7. The measured length change using microscopy (black squares) and the calculated length change using Raman Spectroscopy (orange circles) of the axis parallel to the director (L_{para}) for a monodomain nematic LCE with 62 mol% mesogenic content. The calculated length change is using the order parameter measured with Raman Spectroscopy and Equation 5-3.

An excellent agreement can be seen in Figure 5.7 for the observed length change using microscopy and the length change calculated with Equation 5-3 and the temperature-dependent order parameter. By observing the thermal shape change of the networks we can demonstrate that the relative behaviour of the order parameter

and the shape change response for these materials is in agreement with that expected of densely crosslinked liquid crystalline networks (13).

This concludes the investigations into the order parameters of the monodomain nematic LCEs using Raman Spectroscopy, X-ray Scattering, and microscopy techniques. We shall now turn to X-ray Scattering to discover the underlying network structure of monodomain nematic and isotropic LCEs.

5.4 The Intermolecular Spacing

As aforementioned in Sections 2.4.1 and 3.4.2, the scattering of X-rays from a polymeric material enables the realisation of the internal structure. Wide-Angle X-ray Scattering (WAXS) yields information on the smaller spacings within a network and Small Angle X-ray Scattering (SAXS) can be used to measure the larger structures within a network. Both scattering methods will be used in the following section to realise the whole network structure of the LCEs. The first part of this section will give an insight into the scattering features of these materials that can be easily observed and show the influence of the thickness on the scattering intensity. In later sections, we will reveal all the scattering features detected and uncover the role of phase and composition on the intermolecular spacing.

The following experimental work involves the X-ray Scattering of monodomain nematic and isotropic LCEs, which was in collaboration with my supervisor, Devesh Mistry. This section also uses a sample of poly-EHA synthesised by Stuart Berrow and the X-ray Scattering for this sample was run by Thomas Raistrick. Lastly, this section also compares to X-ray Scattering previously reported for similar materials by Stuart *Berrow et al.* (30) and the data was accessed and analysed from the following dataset (31).

5.4.1 An Introduction to The Scattering of This Family of Nematic LCEs

An example of WAXS on a monodomain nematic LCE can be seen in Figure 5.8 (A & B) in reciprocal space (q, nm^{-1}) of up to $q \sim 35$ nm^{-1}. Here, three key anisotropic scattering features can be readily observed at $q \sim 1.5$ nm^{-1}, 5 nm^{-1}, and 14 nm^{-1}; the feature appearing at $q \sim 14$ nm^{-1} is orientated perpendicular to the director, and the features appearing at $q \sim 1.5$ nm^{-1} and 5 nm^{-1} are parallel to the

director. These three features also appear for isotropic LCEs however, they exhibit no anisotropy.

Figure 5.8 (C & D) also shows the SAXS for the same monodomain nematic LCE, where a scattering of up to $q \sim 14$ nm^{-1} can be well observed. Comparing all the reciprocal space scattering images (Figure 5.8 A - D) WAXS has the capabilities to detect all of the three observable scattering features ($q \sim 1.5$ nm^{-1}, 5 nm^{-1}, and 14 nm^{-1}), however SAXS provides a greater depth of information for the smallest-angle scattering feature ($q \sim 1.5$ nm^{-1}).

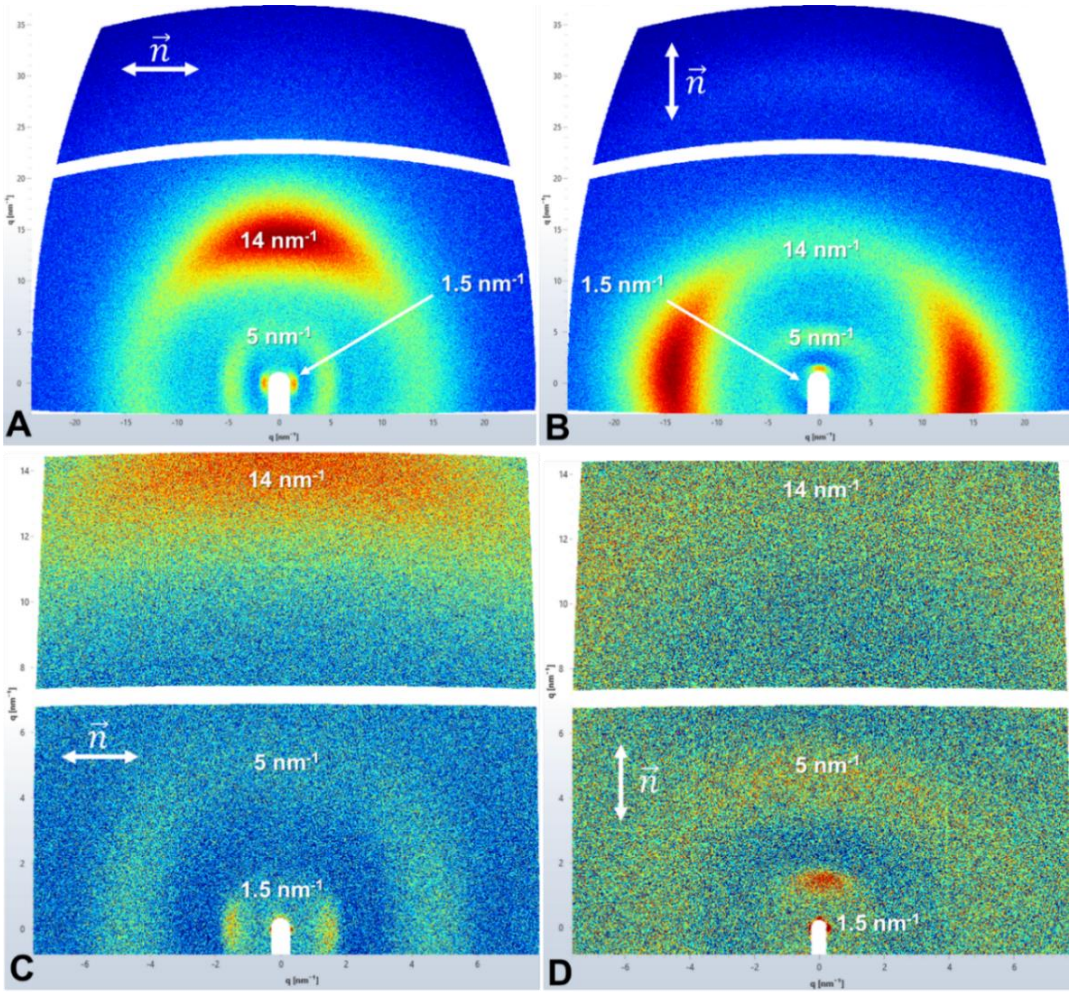

Figure 5.8. (A, B) Wide Angle X-ray Scattering (WAXS) of a 62 mol% mesogenic content monodomain nematic LCE (nLCE-62) in reciprocal space. (C, D) Small Angle X-ray Scattering (SAXS) of nLCE-62 in q-space. Three anisotropic scattering features observed at q ~ 1.5 nm^{-1}, 5 nm^{-1}, and 14 nm^{-1} using SAXS and WAXS. (A) and (C) show scattering at the same sample rotation, which is orthogonal to (B) and (D). The director of the sample is horizontal in (A) and (C) and is vertical in (B) and (D). The WAXS (A, B) is investigated to a q ~ 35 nm^{-1}, the SAXS (C, D) is investigated to a q ~ 14 nm^{-1}.

Figure 5.8 also demonstrates that by scattering for two orthogonal rotations of the sample (A & C) and (B & D), we can gain additional information for the features oriented perpendicular or parallel to the director. Throughout the following work, both rotations will be used to understand each scattering feature.

5.4.2 The Scattering Intensity

Intriguingly, further features of relatively low scattering intensities can be observed upon closer examination of the scattering with SAXS and WAXS. We shall first explore the scattering intensity of the monodomain nematic and isotropic LCEs using WAXS for both the absolute intensity and an intensity that is normalised by thickness, in Figure 5.9A and Figure 5.9B, respectively (following the method outlined in Section 3.4.2). In this section, the scattering intensities have been examined over a ~ 100° cone extending from low to high q along the director of the monodomain nematic LCEs, in a manner that has been similarly shown in Figure 3.11 in Section 3.4.2.

Since there is some variation in the LCE thickness that would affect the scattering intensity, a normalised intensity was used and is simply defined as the absolute intensity divided by the thickness of the LCE (the thicknesses of the LCE samples can be found in Table 3-2 in Section 3.4.2). Although this measure of a normalised thickness will be revealed as a helpful tool to compare the scattering intensities independent of the thicknesses, this measure is not wholly representative of the system. The role of thickness on the scattering intensity is complicated and difficult to quantify; one may expect that a thicker LCE will generate greater scattering, however the scattering intensity may also decay with an increase in the LCE thickness because of absorption effects. Nonetheless, we can use the normalised intensity as a qualitative tool to examine the changes to the scattering intensity due to the varied mesogenic content of LCEs.

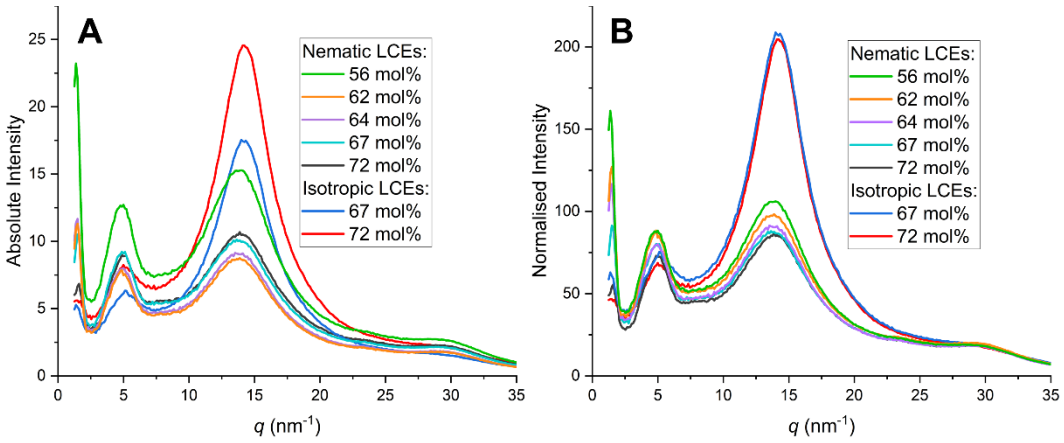

Figure 5.9. (A) The absolute intensity and (B) the normalised intensity of the scattering with Wide-Angle X-ray Scattering (WAXS), determined for the monodomain nematic and isotropic LCEs of varied mesogenic content. The normalised intensity is determined by dividing the absolute intensity by the thickness of the LCE. The scattering was investigated for a ~ 100° cone extending across q and parallel to the director.

We shall first consider the information gained from the absolute intensity of the scattering. Clearly, three key features can be observed at $q \sim 1.5$ nm^{-1}, ~ 5 nm^{-1}, and ~ 14 nm^{-1} (Figure 5.9A), however it is difficult to detect any other scattering features and there is no indication of a trend between the scattering intensity and the composition of the LCEs.

Normalising the scattering intensity by the thickness shows a clear trend of higher scattering intensity for monodomain nematic LCEs with a lower mesogenic content, which is particularly evident in Figure 5.9B for $q < 20$ nm^{-1}. Using the normalised scattering also highlights the existence of two diffraction features at $q \sim 23$ nm^{-1} and 29 nm^{-1}. The feature at $q \sim 23$ nm^{-1} appears perpendicular to the director, however due to a low scattering intensity, it is difficult to determine if there is any orientation to the feature at $q \sim 29$ nm^{-1}. These features are likely higher order diffractions and intriguingly, the feature at $q \sim 23$ nm^{-1} is only observed for the monodomain nematic LCEs.

Lastly, in Figure 5.9B the isotropic LCEs appear to demonstrate a higher scattering than the monodomain nematic LCEs around the $q \sim 14$ nm^{-1} feature. This is solely due to the methodology used, with the scattering intensity investigated parallel to the director for the monodomain nematic LCEs (the axis of weakest scattering intensity for the $q \sim 14$ nm^{-1} feature). Further clarification on this methodology was given in Section 3.4.2.

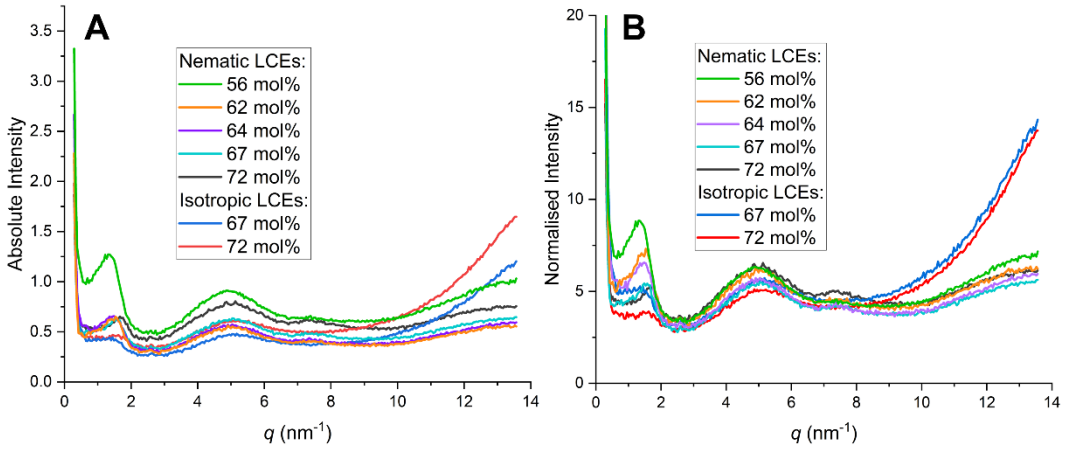

Figure 5.10. The absolute intensity (A) and normalised intensity (B) of the Small-Angle X-ray Scattering (SAXS), determined for the monodomain nematic and isotropic LCEs of varied mesogenic content. The normalised intensity is determined by dividing the absolute intensity by the thickness of the LCE. This scattering is investigated for a ~ 100° cone extending across q and parallel to the director.

A similar comparison between the absolute and normalised scattering intensities can be made using SAXS, as in Figure 5.10. Using the normalised scattering, further features are pronounced at approximately $q \sim 2.6$ nm^{-1} and ~ 7.4 nm^{-1}. The small feature at $q \sim 2.6$ nm^{-1} appears in the trough of the scattering curve with a low intensity (peak is ~ 9% above the intensity of trough) and the feature at $q \sim 7.4$ nm^{-1} appears on the shoulder of the $q \sim 5$ nm^{-1} feature (peak intensity ~ 7% above shoulder intensity). Both scattering features exhibit anisotropy in the monodomain nematic LCEs, with an orientation perpendicular to the director. Interestingly, the feature at $q \sim 7.4$ nm^{-1} is only observed in the monodomain nematic LCEs and is particularly prominent for nLCE-72.

Therefore, the position and intensity of the larger q scattering features ($q \sim 14$ nm^{-1}, 23 nm^{-1} and 29 nm^{-1}) will be quantified using WAXS and the smaller q scattering features ($q \sim 1.5$ nm^{-1}, 2.6 nm^{-1}, 5 nm^{-1}, 7.4 nm^{-1}) will be measured using SAXS. The significance of each scattering feature's intensity and position will be discussed below and will be related to the mesogenic content of the material.

Figure 5.11 below shows a schematic that summarises of all the scattering features for the monodomain nematic (Figure 5.11A) and isotropic (Figure 5.11B) LCEs. This diagram also indicates the appearance of the features and shows the scattering feature orientations with respect to the director for the monodomain nematic LCEs.

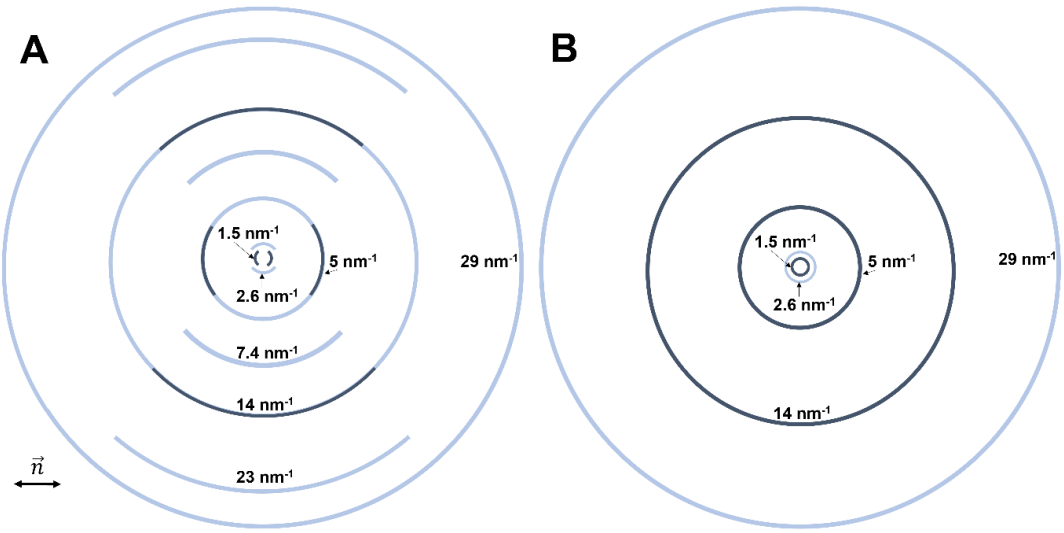

Figure 5.11. A schematic of the SAXS and WAXS scattering features observed for the (A) monodomain nematic and (B) isotropic LCEs; the director of the monodomain nematic LCE is indicated. The colour of the arcs and circles represents the strong (dark blue) or weak (light blue) scattering appearance of each feature.

A summary of all the scattering features in the schematic Figure 5.11 is also given in Table 5-3 below. This table provides the appearance and the orientation of each of the scattering features with respect to the director for the monodomain nematic LCEs. Also included are the approximate spacings that these features correspond to. The spacings are not calculated for the features at $q \sim 23$ nm^{-1} and 29 nm^{-1}, since these weak features are due to higher orders of scattering. In the following sections, we will discuss the nature of each of these scattering features.

Table 5-3. A summary of information about the scattering features observed using SAXS WAXS, including their position in reciprocal space (q), their orientation with respect to the director for monodomain nematic LCEs, the appearance of the scattering feature, and the approximate spacing that the feature corresponds to. The two features marked with an Asterix (*) only appear for the monodomain nematic LCEs. There is also difficulty in determining the orientation of the feature at 29 nm^{-1}.

Feature in q (nm^{-1})	Orientation to Director	Scattering Appearance	Approximate Spacing (Å)
1.5	Parallel	Strong	45
2.6	Perpendicular	Weak	24
5	Parallel	Strong	12
7.4*	Perpendicular	Weak	8.5
14	Perpendicular	Strong	4.4
23*	Perpendicular	Weak	
29	N/A	Weak	

5.4.3 The Impact of Templating and Composition on the Scattering Feature Positions

In this section, we will provide a brief overview of all the scattering features and demonstrate that the key features exhibit positional changes with composition. Following this, we will then determine the cause of each of these scattering features. For simplicity, we will examine the features that are orientated perpendicular to the director for the monodomain nematic LCEs and then address the features that are parallel to the director.

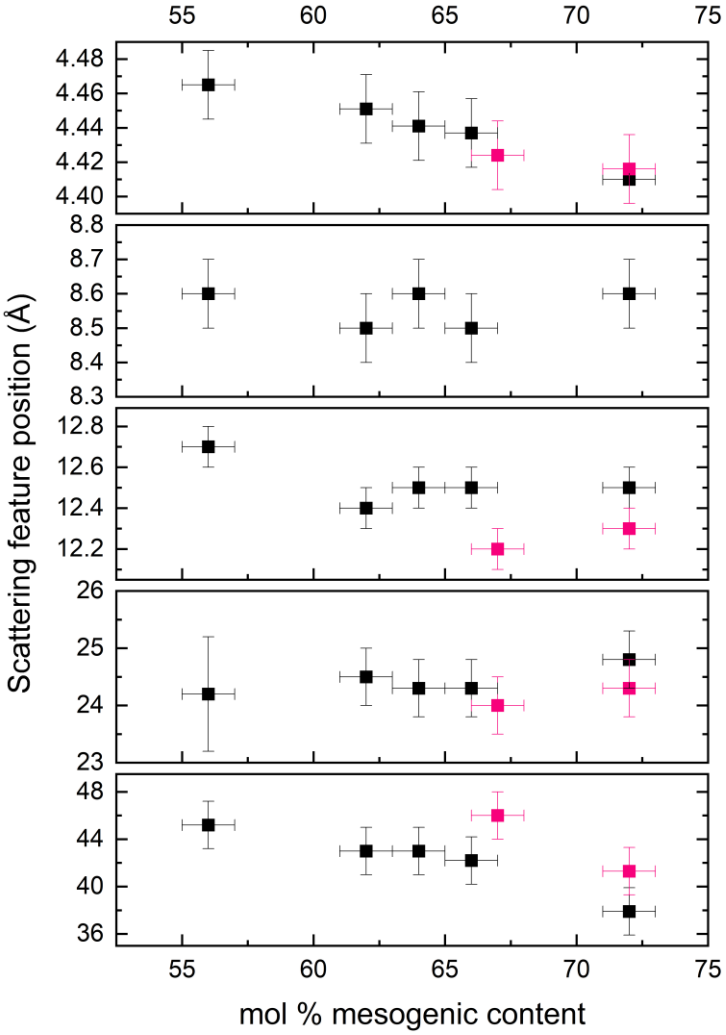

Figure 5.12. The changes to the network spacings measured at ~ 4.4 Å, 8.5 Å 12 Å, 24 Å and 45 Å for the monodomain nematic (black) and isotropic (pink) LCEs, measured using WAXS and SAXS. In general, the LCEs demonstrate an increase in the feature position in reciprocal space, q (ergo a decrease in the network spacing) due to an increase in the mesogenic content. The conversions between the scattering feature position and the network spacing are shown in Table 5-3. The higher order scattering features at q ~ 23 nm^{-1} and ~ 29 nm^{-1} were not converted to a network spacing or investigated as a function of mesogenic content.

Firstly, we observe a shifting in the scattering feature positions with a change in the mesogenic content; specifically, the feature positions in q were observed to increase, corresponding to a reduction in the network spacing, as a results of an increase in the mesogenic content. Figure 5.12, shows these changes in terms of the network spacings (Å) rather than the scattering feature position in q (nm^{-1}). The conversions between the scattering feature position and the real network spacing are shown previously in Table 5-3.

To the best of this author's knowledge, a reduction in the network spacings within the isotropic and monodomain nematic LCEs due to an increased mesogenic content, has not been previously reported. However, similar changes to the smectic layer spacings of smectic LCEs has been seen for varied crosslinking density (32), applied electric field (33) and for applied strain, relaxation, and heating (34). These reports on the smectic layer spacings often discuss the shifting of the spacing within the context of a changing tilt angle, which is fundamentally due to the strength of an applied field (strain, electrical). For this series of monodomain nematic and isotropic LCEs, we may be able to attribute the reduction in the network spacings to an increase in the internal strain of the LCEs. This will be further discussed during later investigations into the role of internal strain for these LCEs in Chapter 7.

5.4.3.i Features Perpendicular to the Director

The scattering features observed at $q \sim 2.6$ nm^{-1}, 7.4 nm^{-1}, 14 nm^{-1} and 23 nm^{-1} appear perpendicular to the director. The strongest scattering feature is at $q \sim 14$ nm^{-1} and emerges as a diffused ring for isotropic LCEs and exhibits anisotropy for the monodomain nematic LCEs. This is a significant feature for the monodomain nematic LCEs, since it's anisotropic scattering intensity is used to provide an order parameter for the material, and this was measured earlier and compared to the order parameters measured with Raman Spectroscopy.

The feature at $q \sim 14$ nm^{-1} corresponds to an average spacing within the network of approximately 4.4 Å, that can be attributed to the side-to-side liquid-like ordering of the mesogenic units. Although there is difficulty with determining the orientation of the faint feature at $q \sim 29$ nm^{-1}, this can be attributed as a second order ($m = 2$)

scattering feature from the strong feature at $q \sim 14$ nm^{-1}. This can be understood by considering the order of diffraction, m, from Bragg's Law $m\lambda = 2d \sin \theta_{Bragg}$.

Interestingly, the scattering feature at $q \sim 14$ nm^{-1} appears in similar positions for the monodomain nematic LCEs, isotropic LCEs and also for a sample of poly-EHA (Figure 5.13). Therefore, each of these materials have a ~ 4.4 Å spacing, which is similar to the typically spacing of ~ 4.5 Å measured for hydrocarbon molecules (35). This suggests that both the EHA side group and the mesogenic units contribute to the scattering feature observed for the LCEs, and this may account for the presence of the weak isotropic-like scattering appearing like a 'background' for this feature in the monodomain nematic LCEs (Figure 5.13A). The sample of poly-EHA was synthesised by Stuart Berrow and the WAXS was run by Thomas Raistrick.

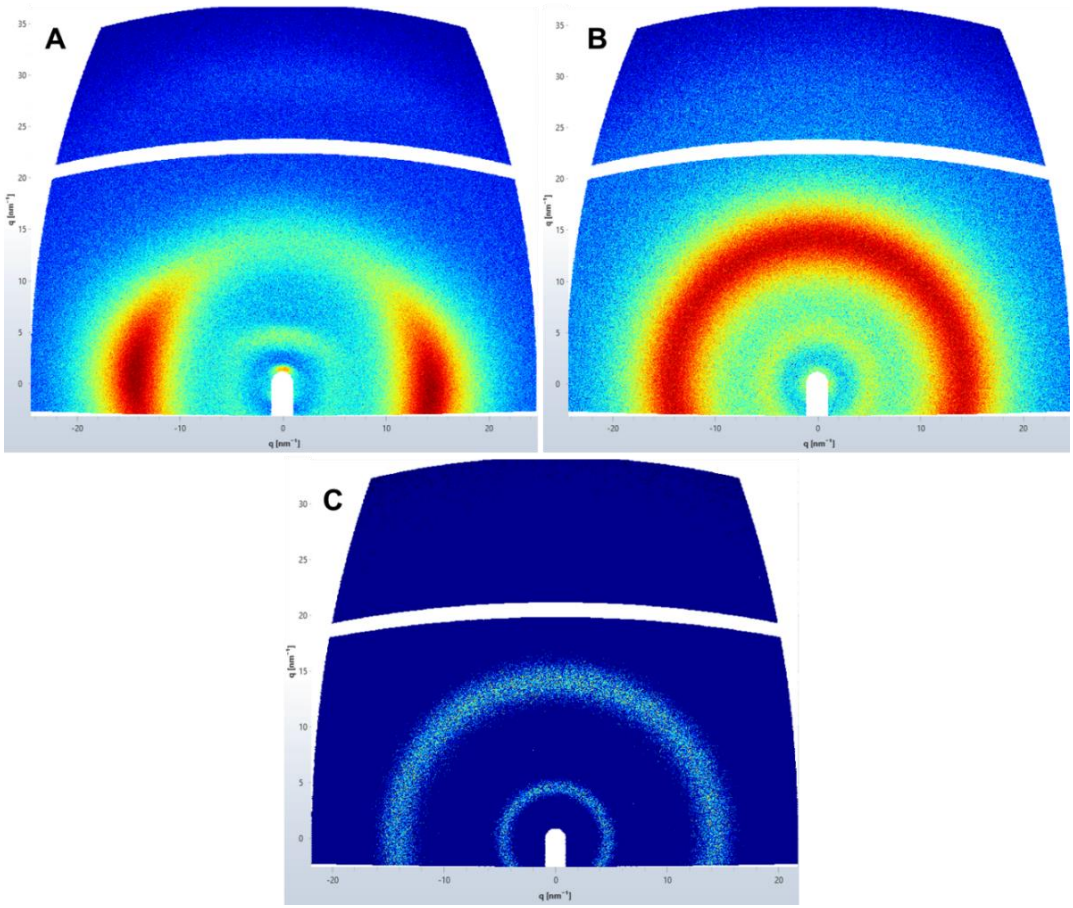

Figure 5.13. WAXS to a q ~ 35 nm^{-1} on a (A) monodomain nematic LCE, (B) isotropic LCE, and (C) poly-EHA sample. All samples exhibit scattering features around q ~ 5 nm^{-1} and ~ 14 nm^{-1}, which appear isotropic for (B) and (C) but exhibit anisotropy for (A). The sample of poly-EHA was synthesised by Stuart Berrow and placed within a glass capillary tube for WAXS, which was run by Thomas Raistrick.

The next scattering feature perpendicular to the director is solely seen for the monodomain nematic LCEs and appears at q ~ 7.4 nm^{-1}. This feature corresponds to a network spacing of ~ 8 Å and does not appear to vary with mesogenic content (Figure 5.12), however this could be due to the difficultly in measuring the feature position since it appears on the shoulder of the q ~ 5 nm^{-1} feature. Another scattering feature that is similarly only apparent for the monodomain nematic LCEs is the feature at q ~ 23 nm^{-1}, which is also orientated perpendicular to the director. Due to the analogous behaviour, these two features (q ~ 7.4 nm^{-1} and q ~ 23 nm^{-1}) could likely be orders of diffraction from the same structure, where m is the order of diffraction from Bragg's Law $m\lambda = 2d \sin\theta_{Bragg}$. In fact, if the q ~ 7.4 nm^{-1} feature is the first order diffraction feature (m = 1), we see an integer order of diffraction for the q ~ 23 nm^{-1} feature (m = 3). However, if this is the case, then further work needs to be undertaken to reveal the significance of an average ~ 8 Å spacing perpendicular to the director in these materials.

Finally, another small feature appears at q ~ 2.6 nm^{-1} for both the monodomain nematic and isotropic materials and indicates an average spacing of 24.4 Å perpendicular to the director. Although this feature at q ~ 2.6 nm^{-1} also evidences some longer-range ordering perpendicular to the director, further investigation would be required to understand the significance of this spacing.

5.4.3.ii Features Parallel to the Director

The scattering features observed at q ~ 1.5 nm^{-1} and 5 nm^{-1} appear with high scattering intensities and are anisotropic and orientated parallel to the director for the monodomain nematic LCEs. These features appear as diffused rings for isotropic LCEs and are equivalent to average network spacings around 42 Å and 12 Å, respectively. Interestingly, we can see from Figure 5.12 that these network spacings also reduce with an increased mesogenic content, for both the monodomain nematic and the isotropic templates.

From the information provided so far, one may attempt to attribute the feature at q ~ 5 nm^{-1} to a higher order diffraction of the q ~ 1.5 nm^{-1} feature, however, an integer of the diffraction order cannot be calculated from these features (m ~ 3.4). Of these two features, only the feature at q ~ 5nm^{-1} appears for all the monodomain nematic,

isotropic LCEs and poly-EHA samples (Figure 5.13), which suggests that this feature is intrinsic to an EHA containing network.

To resolve the underlying network structure that produces features at $q \sim 1.5$ nm^{-1} and 5 nm^{-1}, we will study the series of monodomain nematic and isotropic LCEs critical to this thesis (a series of LCEs with the same components but a varied mesogenic ratio) and make comparisons to the series of monodomain nematic and smectic LCEs by Berrow *et al.* (30) (a series of LCEs with a fixed mesogenic ratio but a varied length of the mesogenic side group). These two series of materials are within the same acrylate family of LCEs that can exhibit an auxetic response in the monodomain nematic template. For simplicity, we will refer to the LCEs investigated throughout this thesis as the '*mesogenic content series'*, and the materials by Berrow *et al.* (31) as the '*spacer length series'*, which will reflect the changing factor of each series. All LCEs across both series exhibit features at $q \sim 1.5$ nm^{-1} and 5 nm^{-1}, so using a wider range of templates and phases will enable us to see how these features change with order and composition, and therefore identify the network structure parallel to the director.

Recently, Berrow *et al.* (30, 31) demonstrated that monodomain nematic (nLCE) and smectic (sLCE) LCE phases can be attained through the variation of the mesogenic side group spacer length (all the LCEs contained a fixed ratio of 62 mol% mesogenic content). Notably, they uncovered that the LCEs, especially those they identified as having a 'smectic-like' phase, exhibited slightly overlapping side groups between nearby backbones. Using SAXS and WAXS, they identified the feature at $q \sim 1.5$ nm^{-1} to correspond to smectic layers of ~ 39 Å: a similar spacing to the simulated length of the fully extended crosslinker (RM82) ~ 38 Å (30, 36). Looking at the dataset, this feature was also observed for their monodomain nematic LCEs, but corresponded to larger spacing of ~ 43 Å. Lastly, they also observed a feature at $q \sim 5$ nm^{-1} parallel to the director for all LCEs, which corresponded to spacings of ~ 12 Å.

The spacings of the $q \sim 1.5$ nm^{-1} and 5 nm^{-1} features have been measured and compared in Figure 5.14 for smectic, monodomain nematic and isotropic LCEs. Remarkably, the spacer length series of LCEs formulated by Berrow *et al.* (30, 31) also exhibited a slight shifting of the positions of the $q \sim 1.5$ nm^{-1} and 5 nm^{-1}

features; the monodomain nematic LCE made with the side group A4OCB has spacings parallel to the director of approximately ~ 12 Å and ~ 46 Å, whereas the smectic LCE made with A9OCB has spacings of approximately ~15 Å and ~ 40 Å. This trend was generally seen across the whole spacer length series by Berrow *et al.* (30, 31), with an increasing 12 Å spacing, yet a decreasing 40 Å spacing (with however, a slight odd-even trend observed for the 40 Å spacing).

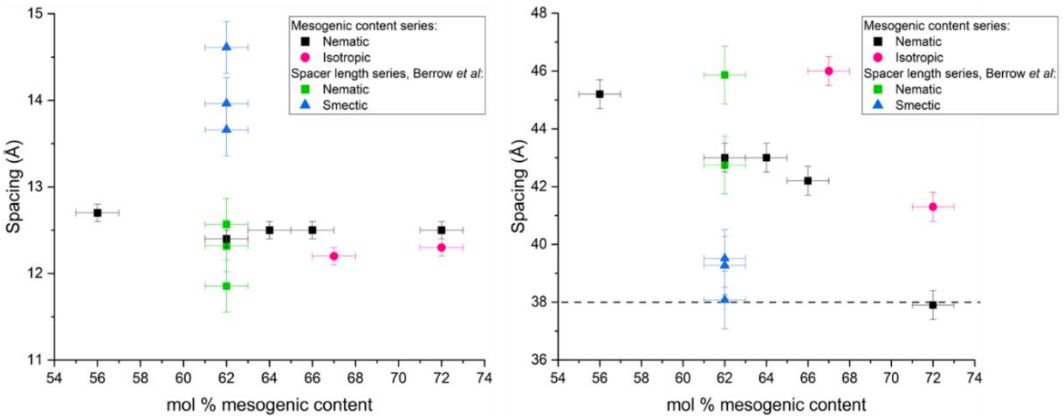

Figure 5.14. The network spacing parallel to the director for the scattering features at (A) q ~ 5 nm^{-1} and (B) 1.5 nm^{-1}, which correspond to network spacings of approximately 12 Å and 40 Å, respectively. (A) A similar spacing is seen around 12 Å for nematic (black and green squares) and isotropic (pink circles) LCEs, with larger spacings seen for smectic LCEs (blue triangles). (B) The layers of the smectic LCEs (blue triangles) and the average end-to-end distance for nematic (black and green squares) and isotropic LCEs (pink circles). The raw data for the monodomain nematic and smectic LCEs of the spacer length series was accessed from the dataset by Berrow et al. (30, 31).

By comparing the mesogenic content series of LCEs to the sample of poly-EHA (Figure 5.13) and the spacer length series by Berrow *et al.* (Figure 5.14) (30, 31), we can ascertain that the feature appearing at q ~ 5 nm^{-1} is inherent to a network containing EHA. This feature presents as a network spacing of 14 Å in poly-EHA, spacings of 12 Å - 15 Å for the spacer length series, and spacings of 12 Å - 13 Å for the mesogenic content series. In fact, molecular simulations predict the fully extended length of EHA to be ~ 16 Å (36), which would suggest that this side group may adopt a relaxed configuration within the network for all the LCE series investigated.

We will now study the scattering feature at q ~ 1.5 nm^{-1}. In the prior study by Berrow *et al.*, this feature was recognised to be the smectic layer spacing of ~ 39 Å in the smectic LCEs, which is comparable to the predicted length of RM82 of ~ 38

Å from molecular simulations (30, 36). However, a larger average spacing is seen for most of the monodomain nematic and isotropic LCEs across both the mesogenic content series and the spacer length series, with spacings of up to ~ 46 Å, which will be considered as the average 'end-to-end' spacing.

Nonetheless, there is evidence that a smectic-like layering may in fact be present for some of the more ordered materials in the mesogenic content series, particularly for nLCE-72, which has a measured spacing of ~ 38 Å (see Figure 5.14). When considering that this family of LCEs have exhibited high order parameters (Section 5.2) and higher orders of diffraction scattering features for both the monodomain nematic and smectic LCEs (Section 5.4.3.i), it is admittedly difficult to distinguish between these templates (30). Therefore, we shall next investigate the correlation length of each of these materials, to quantitatively evaluate any long-range ordering within these templates.

5.4.4 The Correlation Length

The correlation length provides an insight into the range of ordering that is within a material and is often used to investigate the ordering within smectic systems (37, 38) and the smectic-to-nematic transitions (39-41). A larger correlation length corresponds to a longer-range of ordering through a material and its change can demonstrate the shift from an ordered and layered smectic to an ordered nematic phase (no layers) (41).

Here, the mesogenic content series will be compared to the varied spacer length series by Berrow *et al.* (30, 31), whose LCEs have a fixed mesogenic content and the same component ratio as LCE-62 in the mesogenic content series. The correlation lengths parallel ($\xi_{\parallel}$) to the director can be calculated according to Equation 5-4, which is based on the Scherrer equation and was recently used by Kennedy *et al.* for nematic LCEs (37). This equation uses the full width half maximum ($w_{\parallel}$) of the $q \sim 1.5$ nm^{-1} feature. No orientation order will be seen for the isotropic LCEs however the correlation lengths of this phase were also calculated as a control.

$$\xi_{\parallel} = \frac{2\pi}{w_{\parallel}} \qquad \textit{Equation 5-4}$$

The correlation length parallel to the director can be seen in Figure 5.15, comparing isotropic, monodomain nematic, and smectic LCEs within this larger acrylate family. Firstly, we confirm that the smectic LCEs of 62 mol% mesogenic content (blue triangles) have a greater correlation length than the monodomain nematic LCEs of the same composition (green squares and the black square at 62 mol%). The long-range ordering of the smectic LCEs investigated is observed to extend through 4 – 6 smectic layers (dashed lines indicate the length of RM82 as a guide for the eye in Figure 5.15), which is still a weak long range-order compared to other smectic LCEs (41). In fact, Kennedy *et al.* (37) recently demonstrated that their mainchain nematic LCEs have a correlation length that extends through 4 – 9 molecules.

Berrow *et al.* have previously appreciated this weakly smectic behaviour and have fittingly described their system as 'smectic-like' (30); indeed, their LCEs have spacings of ~ 39 Å that indicate a layered structure to the material, however further characteristics that are typical of a smectic phase, such as very sharp scattering features and sharp higher orders of diffractions, are not seen.

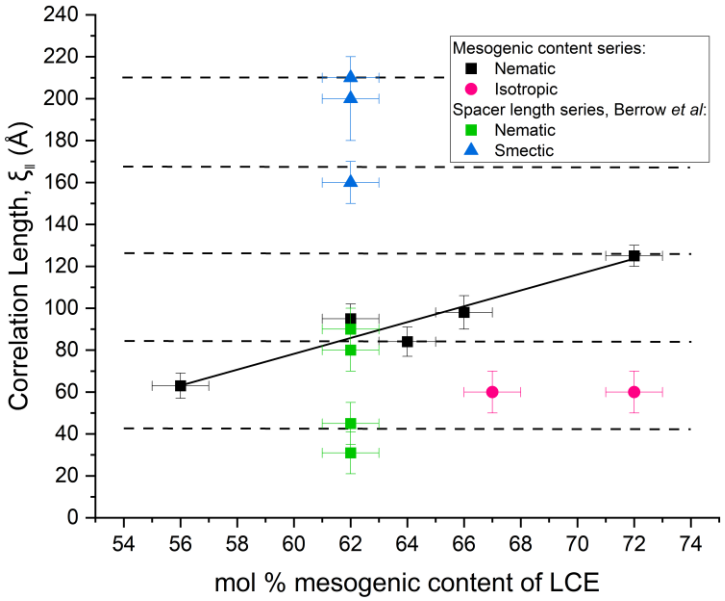

Figure 5.15. The correlation length parallel to the director for smectic (blue triangles) and monodomain nematic LCEs (black and green squares) and the correlation length of isotropic LCEs (pink circles) are added as a control. Black dotted lines of ~ 38 Å separation have been added as a guide for the eye, to show the range of ordering through the smectic layers. A linear fitting (solid black line) is applied to the monodomain nematic LCEs in the mesogenic content series. The raw data for the monodomain nematic and smectic LCEs of the spacer length series was accessed from the dataset by Berrow et al. (30, 31).

Figure 5.15 also demonstrates that the correlation length of the mesogenic content series of monodomain nematic LCEs (black squares) is approximately linear, increasing with the mesogenic content of the network. Interestingly, the nematic materials have an ordering that extends across an effective distance of 2 – 3 average 'end-to-end' spacings within the material; however, we again observe an exception with nLCE-72. This material has a spacing of ~ 38 Å which is reminiscent of smectic layers and can now be seen to exhibit a correlation length parallel to the director that extends across 3 – 4 molecular lengths: greater than all other monodomain nematic LCEs in this family. This one material appears to be at an interface between the behaviours of the monodomain nematic and smectic materials and its phase is difficult to characterize; we shall now refer to this one material as 'smectic-like', for reasoning analogous to that by Berrow *et al.* (30). To be clear, there is no evidence of layer formation for the remaining monodomain nematic LCEs, since these exhibit an average end-to-end spacing of > 42 Å.

5.5 The Density of LCEs

X-ray scattering has so far revealed the role of the composition and the phase on the internal structure of the LCEs. Critically, we have observed a closer packing of the network for LCEs comprising of a higher proportion of mesogenic content, which remarkably suggests an increase in the network density. In this section, the densities of LCEs are measured to fully comprehend the role of composition on the network structure, using the monodomain nematic and isotropic LCEs that were previously investigated using X-ray Scattering.

Previous literature involving the direct measurement of liquid crystalline network densities is limited and mostly focuses on the volume change associated with the UV-induced *trans-to-cis* isomerization of azobenzene containing cholesteric polymer networks (42, 43). This has been previously demonstrated by Liu *et al., via* the resultant change in density of a cholesteric material initially submerged in salt brine that switches to floating under UV exposure (42, 43). There have also been molecular dynamic studies to model the change in density with time during the *trans-to-cis* isomerization in liquid crystalline polymer networks (44).

The methodology used in the following work is akin to the research by Liu *et al.*, who recorded the change in density of cholesteric films submerged in salt brine (42,

43). Here, varied concentrations of glycerol solutions will be used to measure the density of LCEs at room temperature; the methodology can be accessed in Section 3.6.

The densities of varied mesogenic content LCEs are shown in Table 5-4, where an increase in the mesogenic content of the network is seen to lead to an increase in the density, clearly corroborating the inferred density changes from the X-ray Scattering results (Figure 5.12). The density of the monodomain nematic LCEs at 21°C, were measured between 1.12 and 1.16 g/cm^3 for LCEs between 56 and 72 mol% mesogenic content, respectively. The density of isotropic LCEs were measured to be 1.15 g/cm^3 for both LCEs of 67 and 72 mol% mesogenic content.

Although we see only a rather small increase in the density (~ 4%) corresponding to a larger increase in the mesogenic content (~ 16 mol%) of the LCEs, the findings are significant since it confirms that X-ray Scattering can detect a variation of the density for a series of materials. Furthermore, the good agreement between the monodomain nematic and isotropic LCEs of the same mesogenic content suggests that the density is controlled by the composition of the LCE, rather than the phase.

Table 5-4. The density of a series of monodomain nematic and isotropic LCEs between 56 and 72 mol% mesogenic content, measured using aqueous glycerol solutions at room temperature (21°C).

Phase of LCE	Mesogenic content (± 1 mol %)	Density (± 0.01 g/cm^3)
Nematic (*monodomain*)	56	1.12
	62	1.13
	64	1.15
	67	1.15
	72	1.16
Isotropic	67	1.15
	72	1.15

5.6 Summary

In this chapter, the order and network structure has been uncovered for a family of LCEs that exhibit auxetic behaviour in the monodomain nematic template.

Formulation limits have been established for nematic LCEs, wherein sufficient mesogenic material (> 55 mol%) is required to form an ordered nematic phase. The limitation of the nematic phase was deduced with a concentration-dependent adapted Haller equation fitted to the order parameters that were measured with Raman Spectroscopy. Furthermore, the limitations to the phase were experimentally observed, with phase separation present in LCEs with > 55 mol % mesogenic content.

The order parameters measured with both Raman Spectroscopy and X-ray Scattering exhibited good agreement in the order parameter, $\langle P_2 \rangle$. However, the order parameter, $\langle P_4 \rangle$, that was measured with X-ray Scattering was systematically lower than that measured with Raman Spectroscopy. The order parameters measured with Raman Spectroscopy were in good agreement to Maier-Saupe theory, with the exception of the phase separated LCEs. The systematically low measurements of $\langle P_4 \rangle$ using X-ray Scattering are consistent with previous literature using various liquid crystalline systems (9-12).

Then, the temperature-dependent order parameter, $\langle P_2 \rangle$, was considered through the thermal shape changes of the network. Excellent agreement was demonstrated between the observed thermal shape change of a monodomain nematic LCE and the predicted shape change from the order parameter, in line with findings by Broer *et al.* for densely crosslinked liquid crystalline networks (13). Intriguingly, we also demonstrated that the thermal shape change of the network is largely independent of the composition for the three monodomain nematic LCEs investigated. This was shown by considering the data with respect to a reduced temperature relative to T_g, with the glass transition temperature obviously controlling the onset of the shape change behaviour.

To reveal the structure of the network, Small- and Wide- Angle X-ray Scattering (SAXS and WAXS) were used. Several scattering features were found amongst the monodomain nematic and isotropic LCEs and these features were more apparent when considering the intensity normalised by the material thickness. The reduced thickness method highlighted that a greater normalised scattering intensity occurs for nematic LCEs with lower mesogenic content.

The scattering features that were observed using SAXS and WAXS appeared at $q \sim 1.5$ nm^{-1}, 2.6 nm^{-1}, 5 nm^{-1}, 7.4 nm^{-1},14 nm^{-1}, 23 nm^{-1}, and 29 nm^{-1}; the features at $q \sim 1.5$ nm^{-1} and 5 nm^{-1} were parallel to the director, the orientation of the feature at $q \sim 29$ nm^{-1} could not be determined, and the remaining features appeared perpendicular to the director. The features at $q \sim 1.5$ nm^{-1}, 5 nm^{-1} and 14 nm^{-1} were of particular interest due to their high scattering intensity and strongly anisotropic nature.

The feature at $q \sim 1.5$ nm^{-1} was previously attributed to a smectic layer spacing of ~ 39 Å for the 'smectic-like' LCEs by Berrow *et al.* (30, 31) and in line with their reasoning, nLCE-72 in this work shall hence be described as 'smectic-like'. In general, the monodomain nematic and isotropic LCEs in this work showed a larger spacing of ~ 42 Å, which was attributed to an average 'end-to-end' distance. We also demonstrated that these materials have a correlation length that extends through 4 – 6 layers for the smectic LCEs and across 3 – 4 molecules for the smectic-like material nLCE-72; these are relatively low correlation lengths of nematic and smectic LCEs when compared to literature (37, 41). The monodomain nematic LCEs demonstrated an even lower correlation length, as expected, which extends through 2 – 3 molecular 'end-to-end' distances.

The feature at $q \sim 5$ nm^{-1} was determined to be most likely due to scattering from the length of the side group, EHA, since this feature is present for all LCEs in the mesogenic content series, the spacer length series, and in poly-EHA. The last key feature at $q \sim 14$ nm^{-1} also appears across all the LCEs investigated and in poly-EHA. This feature is due to the side-to-side spacing within the material and has a strongly anisotropic nature in the monodomain nematic LCEs. This feature corresponds to a spacing of ~ 4.4 Å for all LCEs and poly-EHA, which is close to the typical spacing of ~ 4.5 Å seen for hydrocarbon molecules (35).

Crucially, the X-ray Scattering also revealed a closer packing of the network for LCEs with a higher mesogenic content, which strongly indicated an increase in the density. Aqueous glycerol solutions of varied concentration were used to measure the density of monodomain nematic and isotropic LCEs as between 1.12 and 1.16 g/cm^3 for LCEs between 56 and 72 mol% mesogenic content, respectively. This corresponds to a relatively small increase in the density (~ 4%) for a large increase

in the mesogenic content (~ 16 mol%) of the LCEs, however is significant in establishing X-ray Scattering as a technique that can detect a change in density.

In the following chapter, Chapter 6, we will be exploring the tunability of the optical properties of this varied mesogenic content series of LCEs. This is of particular importance when considering the potential optical applications of these materials, such as optical strain sensors (7), diffraction gratings (45) and impact resistant glass (1).

5.7 References

1. Cooper, E.J., Reynolds, M., Raistrick, T., Berrow, S.R., Jull, E.I.L., Reshetnyak, V., Mistry, D. and Gleeson, H.F. Controlling the Optical Properties of Transparent Auxetic Liquid Crystal Elastomers. *Macromolecules.* 2024, **57**(5), pp.2030-2038. Available from: https://doi.org/10.1021/acs.macromol.3c02226
2. Jull, E.I.L., Mandle, R.J., Raistrick, T., Zhang, Z., Hine, P.J. and Gleeson, H.F. Toward In Silico Design of Highly Tunable Liquid Crystal Elastomers. *Macromolecules.* 2022, **55**(11), pp.4320-4330. Available from: https://doi.org/10.1021/acs.macromol.2c00587
3. Cordoyiannis, G., Lebar, A., Zalar, B., Žumer, S., Finkelmann, H. and Kutnjak, Z. Criticality Controlled by Cross-Linking Density in Liquid Single-Crystal Elastomers. *Physical Review Letters.* 2007, **99**(19), p.197801. Available from: https://doi.org/10.1103/PhysRevLett.99.197801
4. Finkelmann, H., Kock, H.-J. and Rehage, G. Investigations on liquid crystalline polysiloxanes 3. Liquid crystalline elastomers — a new type of liquid crystalline material. *Die Makromolekulare Chemie, Rapid Communications.* 1981, **2**(4), pp.317-322. Available from: https://doi.org/10.1002/marc.1981.030020413
5. Jia, Y.-G., Zhang, B.-Y., Tian, M. and Pan, W. Synthesis and structure of polysiloxane liquid crystalline elastomers with a mesogenic crosslinking agent. *Journal of Applied Polymer Science.* 2004, **93**(4), pp.1736-1742. Available from: https://doi.org/10.1002/app.20604
6. Barnes, M., Cetinkaya, S., Ajnsztajn, A. and Verduzco, R. Understanding the effect of liquid crystal content on the phase behavior and mechanical

properties of liquid crystal elastomers. *Soft Matter.* 2022, **18**(27), pp.5074-5081. Available from: https://doi.org/10.1039/D2SM00480A

7. Mistry, D., Nikkhou, M., Raistrick, T., Hussain, M., Jull, E.I.L., Baker, D.L. and Gleeson, H.F. Isotropic Liquid Crystal Elastomers as Exceptional Photoelastic Strain Sensors. *Macromolecules.* 2020, **53**(10), pp.3709-3718. Available from: https://doi.org/10.1021/acs.macromol.9b02456
8. Tajbakhsh, A.R. and Terentjev, E.M. Spontaneous thermal expansion of nematic elastomers. *The European Physical Journal E.* 2001, **6**(2), pp.181-188. Available from: https://doi.org/epje/v6/p181(epje01094)
9. Raistrick, T., Mandle, R.J., Zhang, Z., Tipping, P.J. and Gleeson, H.F. Order-disorder behavior in the ferroelectric nematic phase investigated via Raman spectroscopy. *Physical Review E.* 2024, **110**(4), p.044702. Available from: https://doi.org/10.1103/PhysRevE.110.044702
10. Singh, G., Fu, J., Agra-Kooijman, D.M., Song, J.-K., Vengatesan, M.R., Srinivasarao, M., Fisch, M.R. and Kumar, S. X-ray and Raman scattering study of orientational order in nematic and heliconical nematic liquid crystals. *Physical Review E.* 2016, **94**(6), p.060701. Available from: https://doi.org/10.1103/PhysRevE.94.060701
11. Sanchez-Castillo, A., Osipov, M.A. and Giesselmann, F. Orientational order parameters in liquid crystals: A comparative study of x-ray diffraction and polarized Raman spectroscopy results. *Physical Review E.* 2010, **81**(2), p.021707. Available from: https://doi.org/10.1103/PhysRevE.81.021707
12. Sims, M.T., Abbott, L.C., Richardson, R.M., Goodby, J.W. and Moore, J.N. Considerations in the determination of orientational order parameters from X-ray scattering experiments. *Liquid Crystals.* 2019, **46**(1), pp.11-24. Available from: https://doi.org/10.1080/02678292.2018.1455227
13. Broer, D.J. and Mol, G.N. Anisotropic thermal expansion of densely cross-linked oriented polymer networks. *Polymer Engineering & Science.* 1991, **31**(9), pp.625-631. Available from: https://doi.org/10.1002/pen.760310902
14. Raistrick, T., Zhang, Z., Mistry, D., Mattsson, J. and Gleeson, H.F. Understanding the physics of the auxetic response in a liquid crystal elastomer. *Physical Review Research.* 2021, **3**(2), p.023191. Available from: https://doi.org/10.1103/PhysRevResearch.3.023191

15. Wang, Z., Raistrick, T., Street, A., Reynolds, M., Liu, Y. and Gleeson, H.F. Direct Observation of Biaxial Nematic Order in Auxetic Liquid Crystal Elastomers. *Materials.* 2022, **16**(1). Available from: https://doi.org/10.3390/ma16010393

16. Berrow, S.R., Mandle, R.J., Raistrick, T., Reynolds, M. and Gleeson, H.F. Toward Monodomain Nematic Liquid Crystal Elastomers of Arbitrary Thickness through PET-RAFT Polymerization. *Macromolecules.* 2024, **57**(11), pp.5218-5229. Available from: https://doi.org/10.1021/acs.macromol.4c00245

17. Broer, D.J., Hikmet, R.A.M. and Challa, G. In-situ photopolymerization of oriented liquid-crystalline acrylates, 4. Influence of a lateral methyl substituent on monomer and oriented polymer network properties of a mesogenic diacrylate. *die Makromolekulare Chemie.* 1989, **190**(12), pp.3201-3215. Available from: https://doi.org/10.1002/macp.1989.021901218

18. Haller, I. Thermodynamic and static properties of liquid crystals. *Progress in Solid State Chemistry.* 1975, **10**, pp.103-118. Available from: https://doi.org/10.1016/0079-6786(75)90008-4

19. Barbero, G. and Evangelista, L.R. Concentration dependence of the scalar order parameter in liquid-crystalline systems with variable molecular shape. *Physical Review E.* 2000, **61**(3), pp.2749-2752. Available from: https://doi.org/10.1103/PhysRevE.61.2749

20. Maier, W. and Saupe, A.Z. Eine einfache molekulare Theorie des nematischen kristallinflüssigen Zustandes. *Naturforsch.* 1958, **13a**, pp.564-566.

21. Maier, W. and Saupe, A.Z. Eine einfache molekular-statistische Theorie der nematischen kristallinflüssigen Phase. Teil I[1]. *Naturforsch.* 1959, **14a**, pp.882–889.

22. Maier, W. and Saupe, A.Z. Eine einfache molekular-statistische Theorie der nematischen kristallinflüssigen Phase. Teil II. *Naturforsch.* 1960, **15a**, pp.287–292.

23. Zannoni, C. Order Parameters and Orientational Distributions in Liquid Crystals. In: Samori, B. and Thulstrup, E.W. eds. *Polarized Spectroscopy of Ordered Systems*. Dordrecht: Springer Netherlands, 1988, pp.57-83.

24. Andrienko, D. Introduction to liquid crystals. *Journal of Molecular Liquids.* 2018, **267**, pp.520-541. Available from: https://doi.org/10.1016/j.molliq.2018.01.175

25. Kratky, O. Zum Deformationsmechanismus der Faserstoffe, I. *Kolloid-Zeitschrift.* 1933, **64**(2), pp.213-222. Available from: https://doi.org/10.1007/BF01434162

26. Ware, T.H., McConney, M.E., Wie, J.J., Tondiglia, V.P. and White, T.J. Voxelated liquid crystal elastomers. *Science.* 2015, **347**(6225), pp.982-984. Available from: https://doi.org/doi:10.1126/science.1261019

27. Cviklinski, J., Tajbakhsh, A.R. and Terentjev, E.M. UV isomerisation in nematic elastomers as a route to photo-mechanical transducer. *The European Physical Journal E.* 2002, **9**(1), pp.427-434. Available from: https://doi.org/10.1140/epje/i2002-10095-y

28. Mol, G.N., Harris, K.D., Bastiaansen, C.W.M. and Broer, D.J. Thermo-Mechanical Responses of Liquid-Crystal Networks with a Splayed Molecular Organization. *Advanced Functional Materials.* 2005, **15**(7), pp.1155-1159. Available from: https://doi.org/10.1002/adfm.200400503

29. Achorn, P.J. and Ferrillo, R.G. Comparison of thermal techniques for glass transition measurements of polystyrene and cross-linked acrylic polyurethane films. *Journal of Applied Polymer Science.* 1994, **54**(13), pp.2033-2043. Available from: https://doi.org/10.1002/app.1994.070541305

30. Berrow, S.R., Raistrick, T., Mandle, R.J. and Gleeson, H.F. Structure–Property Relationships in Auxetic Liquid Crystal Elastomers—The Effect of Spacer Length. *Polymers.* 2024, **16**(14), p.1957. Available from: https://www.mdpi.com/2073-4360/16/14/1957

31. Berrow, S.R., Raistrick, T., Mandle, R. and Gleeson, H.F. Dataset associated with "Structure-Property Relationships in Auxetic Liquid Crystal Elastomers – The Effect of Spacer Length". [Online]. 2024. Available from: https://doi.org/10.5518/1449

32. Liang, T., van Kuringen, H.P.C., Mulder, D.J., Tan, S., Wu, Y., Borneman, Z., Nijmeijer, K. and Schenning, A.P.H.J. Anisotropic Dye Adsorption and Anhydrous Proton Conductivity in Smectic Liquid Crystal Networks: The Role of Cross-Link Density, Order, and Orientation. *ACS Applied Materials*

& Interfaces. 2017, **9**(40), pp.35218-35225. Available from: https://doi.org/10.1021/acsami.7b09386

33. Spillmann, C.M., Konnert, J.H., Deschamps, J.R., Naciri, J. and Ratna, B.R. Molecular Packing in Electroclinic Liquid Crystal Elastomer Films. *Chemistry of Materials.* 2008, **20**(19), pp.6130-6139. Available from: https://doi.org/10.1021/cm801335j
34. Dey, S., Agra-Kooijman, D.M., Ren, W., McMullan, P.J., Griffin, A.C. and Kumar, S. Soft Elasticity in Main Chain Liquid Crystal Elastomers. *Crystals.* 2013, **3**(2), pp.363-390. Available from: https://www.mdpi.com/2073-4352/3/2/363
35. Agra-Kooijman, D.M. and Kumar, S. X-Ray Scattering Investigations of Liquid Crystals. In: J. W. Goodby, P. J. Collings, T. Kato, C. Tschierske, H. F. Gleeson and P. Raynes eds. *Handbook of Liquid Crystals*. Second ed., 2014, pp.1-38.
36. Mandle, R. *Private correspondence on predicted liquid crystal elastomer structure using molecular simulations*, 2024.
37. Kennedy, D.T., Hoang, J.D., Toney, M.F. and White, T.J. Deconvoluting the Contribution of Polymerization Temperature to Liquid Crystalline Elastomer Actuation. *Macromolecules.* 2024. Available from: https://doi.org/10.1021/acs.macromol.4c01713
38. Witkowski, L.T. and Terentjev, E.M. Quenched random disorder and x-ray scattering in smectic elastomers. *Physical Review E.* 2009, **80**(5), p.051701. Available from: https://doi.org/10.1103/PhysRevE.80.051701
39. de Jeu, W.H., Ostrovskii, B.I., Kramer, D. and Finkelmann, H. Random disorder and the smectic-nematic transition in liquid-crystalline elastomers. *Physical Review E.* 2011, **83**(4), p.041703. Available from: https://doi.org/10.1103/PhysRevE.83.041703
40. Clark, N.A., Bellini, T., Malzbender, R.M., Thomas, B.N., Rappaport, A.G., Muzny, C.D., Schaefer, D.W. and Hrubesh, L. X-ray scattering study of smectic ordering in a silica aerogel. *Physical Review Letters.* 1993, **71**(21), pp.3505-3508. Available from: https://doi.org/10.1103/PhysRevLett.71.3505

41. de Jeu, W.H. and Ostrovskii, B.I. Order and Disorder in Liquid-Crystalline Elastomers. In: *Liquid Crystal Elastomers: Materials and Applications*. Berlin, Heidelberg: Springer Berlin Heidelberg, 2011.

42. Liu, D., Bastiaansen, C.W.M., den Toonder, J.M.J. and Broer, D.J. Light-Induced Formation of Dynamic and Permanent Surface Topologies in Chiral–Nematic Polymer Networks. *Macromolecules.* 2012, **45**(19), pp.8005-8012. Available from: https://doi.org/10.1021/ma301628h

43. Liu, D. and Broer, D.J. New insights into photoactivated volume generation boost surface morphing in liquid crystal coatings. *Nature Communications.* 2015, **6**(1), p.8334. Available from: https://doi.org/10.1038/ncomms9334

44. Peeketi, A.R., Joseph, E., Swaminathan, N. and Annabattula, R.K. Photo-activated dynamic isomerization induced large density changes in liquid crystal polymers: A molecular dynamics study. *The Journal of Chemical Physics.* 2024, **160**(10). Available from: https://doi.org/10.1063/5.0187320

45. Moorhouse, T. and Raistrick, T. Sub-Micron Diffractive Optical Elements Facilitated by Intrinsic Deswelling of Auxetic Liquid Crystal Elastomers. *Advanced Optical Materials.* 2024, **12**(24), p.2400866. Available from: https://doi.org/10.1002/adom.202400866

Chapter 6 The Tuneable Optical Properties of LCEs

Large portions of the work throughout this chapter have previously been published in (1):

Emily J. Cooper, *et al*. "*Controlling the Optical Properties of Transparent Auxetic Liquid Crystal Elastomers"*. Macromolecules, 2024, **57**(5), 2030-2038.

Figures that have been published will be stated in the caption. Any experimental work that was not performed by the author, Emily Jane Cooper, will be stated in the text or the figure caption.

6.1 Introduction

In this thesis so far, we have established that the full characterisation of the properties of a material is imperative for applications. As aforementioned, commercial materials have well recorded properties (2) including the thermal, mechanical, physical, and optical. In the previous chapters, we have detailed a number of these properties for a series of LCEs and have verified these materials as effective energy dissipators.

In the following chapter, we will investigate the optical properties of monodomain nematic and isotropic templates within this family of acrylate LCEs; the optical properties of the polydomain nematic template will not be investigated due to opacity. However, we will demonstrate that the monodomain nematic LCEs have a high optical transparency, proving these materials to be excellent candidates as laminates in applications such as impact resistant glass. The isotropic template has previously been shown to behave mechanically like conventional isotropic elastomers but with exceptionally large photoelastic coefficients and therefore with excellent potential as optical strain sensors (3).

Later in this chapter, we will demonstrate that the refractive indices and the birefringence of these LCEs can be tuned *via* the mesogenic content of the material and can be selected based on the composition. We will also show that within a near ambient temperature range (25°C - 50°C), the temperature-dependent optical properties appear to be dominated by density changes in the material, likewise seen in optical plastics. Finally, this chapter will connect the optical properties and the

order parameters of the monodomain nematic LCEs, the latter of which were previously discussed in Section 5.2.

6.2 Spectrometry of Polymeric Materials

In this preliminary section, we will report the transmission spectrum of a monodomain nematic LCE and the reflection spectrum of a poly-EHA sample. These results are analysed first, since these are crucial for later discussions in this chapter; the transmission spectrum of the LCE is required to select the best optical method and wavelength to characterise the material, and the reflection spectrum of poly-EHA is needed to determine a refractive index for this material.

Firstly, the transmission spectrum for a 62 mol% mesogenic content monodomain nematic LCE is shown in Figure 6.1. The transmission spectrum was measured and corrected for Fresnel losses along the axes corresponding to the extraordinary and ordinary axes, n_o and n_e, respectively. The synthesis of this LCE and the measurement of the transmission spectrum was performed by Ethan Jull. The Fresnel losses were corrected for by Ethan Jull and Helen Gleeson.

Clearly, the monodomain nematic LCE demonstrates a good optical transparency across the spectrum, and there is no noticeable difference in the transmission between either axis. In fact, we observe a high transmission of ~ 94% across the material for a wavelength of 589 nm. Therefore, the monodomain nematic LCEs show a good optical transparency in the visible range, thus the refractive indices of the material can be determined using a suitable refractometry method; we will shortly explore the existing methods that have been used to determine the refractive indices of liquid crystals and plastics so far and choose a suitable method for these LCEs.

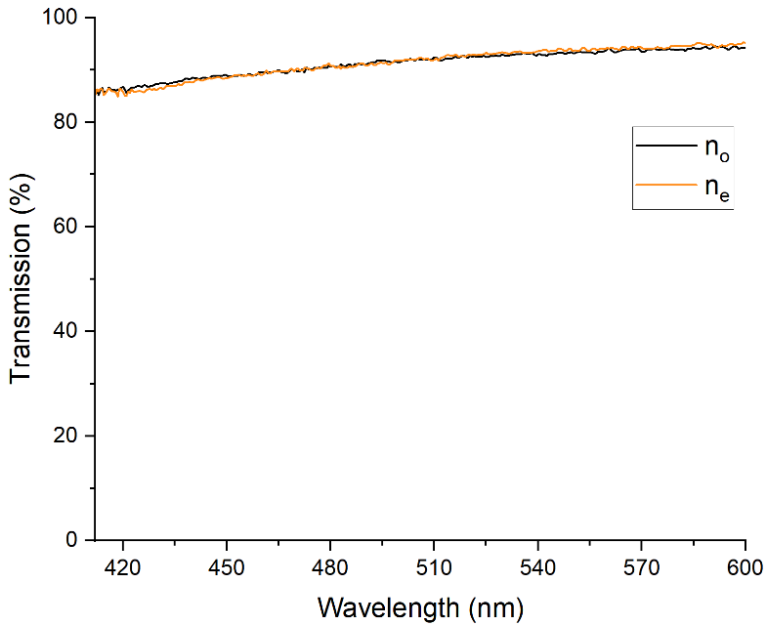

Figure 6.1. The transmission spectrum of a monodomain nematic LCE (nLCE-62), measured with the light polarized along both n_o and n_e across visible wavelengths. The data have been corrected for the light losses due to Fresnel reflections. The transmission of the LCE is > 94% for both orientations at 589nm. The synthesis of this LCE and the measurement of the transmission spectra was performed by Ethan Jull. The Fresnel losses were corrected for by Ethan Jull and Helen Gleeson. This figure has been published by Cooper et al. (1).

To determine whether the mesogenic content has an impact on the refractive indices and the birefringence of LCEs, we need to investigate the properties of the materials at the limitations of the mesogenic content, as done in the previous chapters. However, as outlined in Section 3.2.1, phase separation is observed for LCEs with less than ~ 55 mol% mesogenic content and the refractive indices for these materials cannot be measured. Therefore, we used a film of poly-EHA (referred to as pEHA), as a measure of the average refractive index for a material with 0 mol% mesogenic content. Reflection Spectroscopy was used to measure the refractive index of pEHA, following the methodology described in Section 3.5.2. The pEHA material was made by Stuart Berrow.

In Figure 6.2, the visible light spectrum of a thin film of pEHA is shown (red dots) alongside a fitting to the spectrum (blue line). Crucially, the positions of the peaks and troughs of the fitting (blue line) are particularly dependent on the refractive index. Figure 6.2, the fitting to the spectrum shows a good agreement, particularly when considering the positions of the peaks and troughs. The fitting provides a

measurement for the average refractive index of pEHA as n_{pEHA} = 1.46 $\pm$ 0.01 at 25.4 $\pm$ 0.1 ˚C.

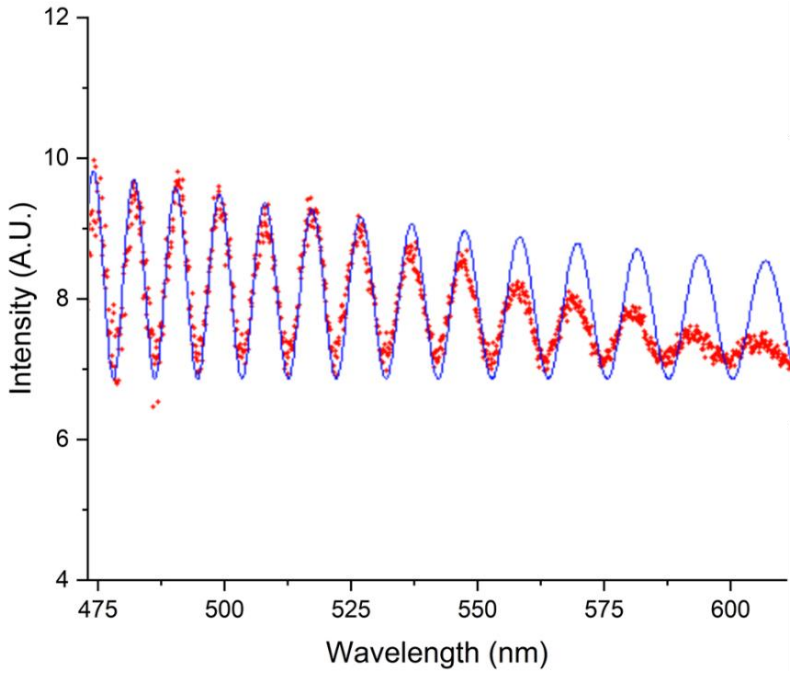

Figure 6.2. The spectrum of poly-EHA (red dots) and the fitting program (blue line) with a refractive index of n_{pEHA} = 1.46 and a film thickness of 9 µm. The poly-EHA material was synthesised by Stuart Berrow. The refractive index extracted from this figure is published by Cooper et al. (1).

6.3 The Temperature-Dependent Optical Properties of LCEs

In the following section, we will investigate the temperature-dependent optical properties of monodomain nematic LCEs. Crucially, this includes direct measurements of the refractive indices, a parameter which has rarely been reported for LCEs. To therefore recognize the significance of these measurements and the methodology employed, we shall first briefly review the existing literature. We will then outline the results for this series of LCEs.

6.3.1 Literature on Refractive Indices for LCEs and Similar Materials

The optical properties of optical plastics, such as the refractive indices, are widely reported in the range of 10°C - 40°C, and are used to optimize the suitability of the materials for applications at near ambient conditions (4). The refractive indices of low molar mass liquid crystals have also been widely reported, however there have rarely been measurements of the individual refractive indices of LCEs. This is

further surprising when considering that LCEs have often been suggested as good candidates for optical functions. We shall first consider the existing optical measurements of LCNs and LCEs, before providing results for the present series of materials.

The optical properties of LCEs, particularly the values of the ordinary (n_o) and extraordinary (n_e) refractive indices and the birefringence (Δn), will affect the proposed function of the material. The refractive indices of LCEs are critical to their sensitivity and appearance in optical strain sensing and mechanochromic devices which are based on the photoelastic (strain-induced birefringence) and selective reflection (strain-dependent chiral nematic pitch) effects (3, 5-7). More broadly, where a LCE is integrated into an optical or display device, for instance for haptic (8), cleaning (9), or protection purposes (10), the material refractive indices and transparency will affect the optical quality of the whole device.

Broer *et al.* (11, 12) used an Abbé Refractometer to measure the temperature dependence of densely crosslinked LCNs and focused on the refractive indices' temperature dependence in the glassy phase, concluding that the decrease in refractive indices with temperature was likely to be driven by the changing density of the network. Their studies demonstrated that the final networks' refractive indices were controlled *via* the temperature at which polymerisation was performed, however the studies did not consider how refractive indices of the networks could be controlled *via* formulation.

Several papers report the birefringence of LCEs, for instance as a function of temperature, however as highlighted above, knowledge of the refractive indices themselves is important (13, 14). Varanytsia *et al.* (15) analysed the reflection spectra of a chiral nematic acrylate LCE designed for lasing, to deduce that n_o and n_e took values between 1.50 – 1.53 and 1.65 – 1.59 respectively, over a temperature range from ~ 23˚C to 75˚C. This technique can be extremely accurate for chiral liquid crystals where excellent alignment can be achieved and a fit can be made to the reflection spectra to deduce the optical coefficients (16). Optical diffraction has also been reported for measurements of refractive index modulation in azo-doped siloxane LCEs, with modifications of the birefringence of the order of ~ 10^{-2} (17). These few studies indicate the challenge in measuring the refractive indices of LCEs

and therefore, the lack of knowledge of how to control refractive indices using methods such as formulation.

We will now report the refractive indices and the birefringence of monodomain nematic and isotropic LCEs, which were directly measured using Abbé Refractometry; the work in this chapter has been published by Emily Cooper *et al.* (1).

6.4 The Temperature-Dependent Optical Properties of Nematic LCEs

We consider the temperature-dependent optical properties for a series of monodomain nematic LCEs of varied compositions: nLCE-62, nLCE-64, nLCE-67, and nLCE-72. The optical properties of these LCEs were investigated since the materials within this range have each been demonstrated as effective energy dissipators in Section 4.3.2. However, nLCE-72 has also exhibited a smectic-like behaviour in Sections 4.3.3and 5.4.4, which adds further intrigue to the material's optical behaviour. Specifically, we will reveal the refractive indices, the temperature coefficients of refractive index, and the birefringence for this series of monodomain nematic LCEs.

Figure 6.3 shows the ordinary and extraordinary refractive indices, n_o and n_e respectively, determined for each monodomain nematic LCE as a function of temperature. The refractive indices were measured using an Abbé Refractometer and the method has been previously described in Section 3.5.1. We can see that for an increase in the mesogenic content, there is clearly a greater increase in n_e than n_o; for a 10 mol% change in the mesogenic content, n_e increased by ~ 0.026, while n_o increased by only ~ 0.003. The role of composition on the optical properties of the monodomain nematic LCEs will be discussed later; we will first focus on the temperature-dependence of these optical properties.

For each material in Figure 6.3, the refractive indices, n_o and n_e, linearly decrease by ~ 0.005 and ~ 0.015 respectively, over the ~ 30°C window studied. Such a linear decrease in the refractive index with temperature is typically attributed to changes in density and is common for many optical plastics. Similar behaviour was reported by Broer *et al.* (11, 12) in the glassy phase of liquid crystalline networks and this was attributed to a density change in the network.

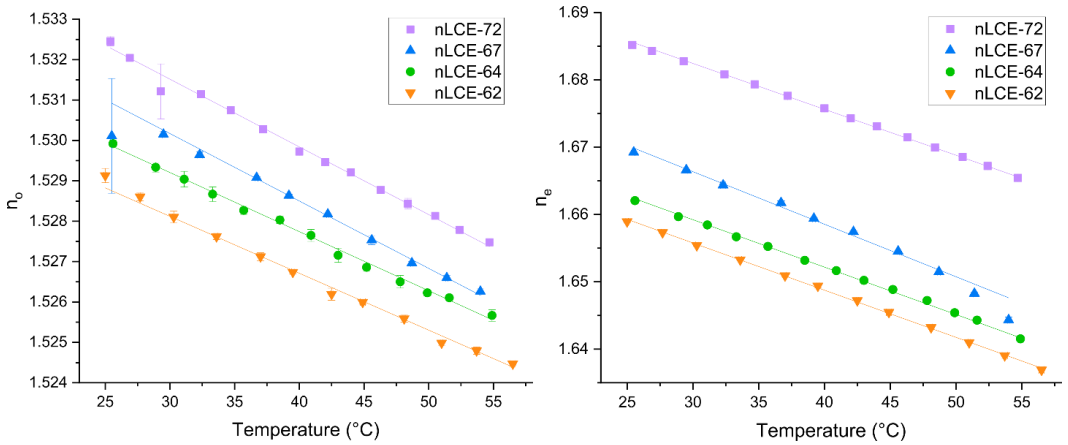

Figure 6.3. The temperature dependence of the ordinary and extraordinary refractive indices, n_o and n_e respectively, for the monodomain nematic LCEs: nLCE-72 (purple squares), nLCE-67 (blue triangles), nLCE-64 (green circles) and nLCE-62 (orange triangles). The nLCE-62 used was synthesised by Matthew Reynolds. This figure has been published by Cooper et al. (1).

It is noteworthy that the clearly linear behaviour of the refractive indices, over the temperature range studied, is quite distinct from the usual temperature dependence of refractive indices of liquid crystals that was established in Section 2.5 (18). Specifically, although n_e reduces with increasing temperature in all liquid crystals, its behaviour is not usually linear and n_o typically increases with increasing temperature. Such behaviour is driven by the reduction in the order parameter of nematic liquid crystals with increasing temperature.

The fact that the monodomain nematic LCEs reported here have no measurable T_{NI} up to 250°C (using DSC in Section 4.2.1), explains why the linear fits with a negative gradient can describe the temperature dependence of all the refractive indices so well; the variation in the temperature-dependent order parameter must be negligible over the ~ 30°C temperature range studied. This will be proven to be the case in the following chapter, Chapter 7.

We shall now consider the average refractive indices of the monodomain nematic LCEs, n_{av}, which can be determined according to Equation 6-1. This equation was introduced in Equation 2-11 in Section 2.5, and has been written here again for convenience. This relation by Vuks (19) uses the ordinary and extraordinary refractive indices, n_o and n_e, that were previously measured.

$$n_{av} = \sqrt{\frac{(n_e{}^2 + 2n_o{}^2)}{3}} \qquad \textit{Equation 6-1}$$

The average refractive indices in Figure 6.4 are shown to decrease with an increase in temperature and follow an approximately linear trend similar to Figure 6.3. Again, we observe that nLCE-72 has the highest refractive index of the materials at any given temperature.

We will now use the linear fittings in Figure 6.3 and Figure 6.4 to measure an optical property known as the temperature coefficient of refractive index $\left(\frac{dn}{dT}\right)$ (4). This can be measured for the ordinary, extraordinary, and average refractive indices of the monodomain nematic LCEs.

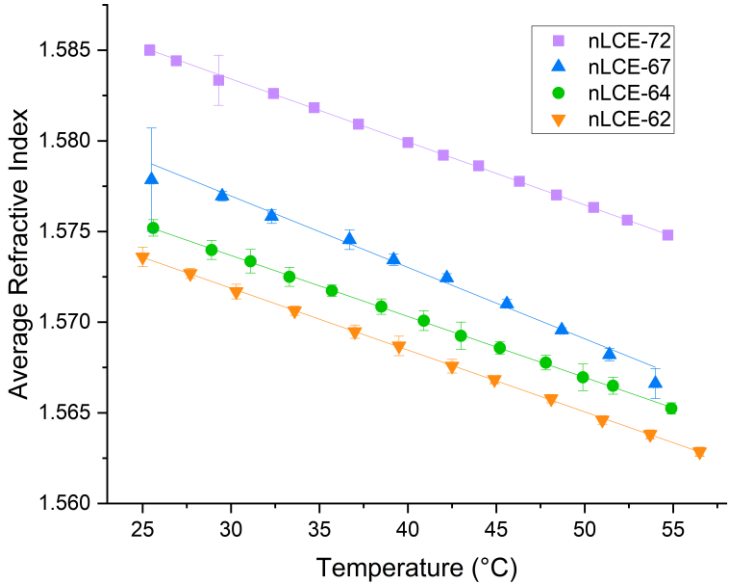

Figure 6.4. The temperature dependence of the average refractive indices, n_{av}, for the monodomain nematic LCEs: nLCE-72 (purple squares), nLCE-67 (blue triangles), nLCE-64 (green circles), and nLCE-62 (orange triangles). The average refractive indices are determined according to Equation 6-1. The nLCE-62 used was synthesised by Matthew Reynolds. This figure has been published by Cooper et al. (1).

All the measured temperature coefficients of refractive index are shown in Table 6-1 below. The coefficients of the ordinary $\left(\frac{dn_o}{dT}\right)$ and extraordinary $\left(\frac{dn_e}{dT}\right)$ refractive indices were all measured between $-1 \times 10^{-4}\ \mathrm{K}^{-1}$ and $-8 \times 10^{-4}\ \mathrm{K}^{-1}$, and are of the same order as many optical plastics (4). Moreover, the temperature coefficient of the average refractive index $\left(\frac{dn_{av}}{dT}\right)$ for the LCEs were all measured around $-3.5 \times 10^{-4}\ \mathrm{K}^{-1}$ and are comparable to the reported experimental values of coefficients for acrylate elastomers, which are between $-4.2 \times 10^{-4}\ \mathrm{K}^{-1}$ and $-4.5 \times 10^{-4}\ \mathrm{K}^{-1}$ (20, 21).

Table 6-1. The temperature coefficients of refractive index for the ordinary, extraordinary, and average refractive indices, $\frac{dn_o}{dT}$, $\frac{dn_e}{dT}$ and $\frac{dn_{av}}{dT}$ respectively, for the monodomain nematic LCEs studied. The nLCE-62 used was synthesised by Matthew Reynolds. This table has been published by Cooper et al. (1).

Mesogenic content of nLCE (± 1 mol%)	Temperature coefficient of refractive index ($\times 10^{-4}\ K^{-1}$)		
	$\frac{dn_o}{dT}$	$\frac{dn_e}{dT}$	$\frac{dn_{av}}{dT}$
72	-1.68 ± 0.01	-6.82 ± 0.05	-3.47 ± 0.02
67	-1.67 ± 0.03	-7.8 ± 0.3	-3.94 ± 0.01
64	-1.46 ± 0.02	-7.05 ± 0.08	-3.37 ± 0.02
62	-1.41 ± 0.03	-7.02 ± 0.05	-3.41 ± 0.02

We shall now consider the birefringence of these materials, which quantifies the anisotropy of the refractive indices. In Figure 6.5, a greater birefringence is observed in for an increase in the mesogenic content, which is driven by the larger changes in n_e than n_o, as in Figure 6.3. The largest birefringence measured was ~ 0.15 for nLCE-72 at ~ 25°C, which is significantly greater than the birefringence of ~ 0.13 measured for nLCE-62 at the same temperature. Furthermore, the birefringence in Figure 6.5 clearly decreases with an increase in the temperature, analogous to the prior behaviour of the refractive indices in Figure 6.3 and Figure 6.4.

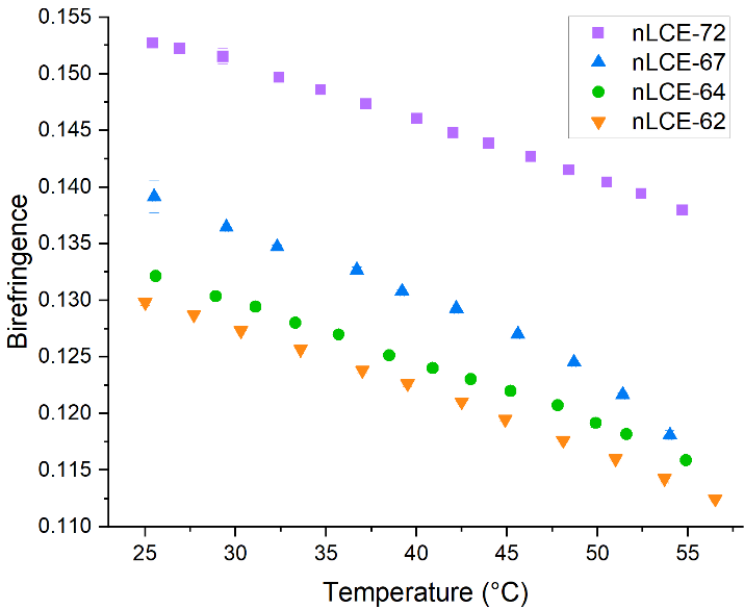

Figure 6.5. The temperature dependence of the birefringence for the monodomain nematic LCEs: nLCE-72 (purple squares), nLCE-67 (blue triangles), nLCE-64 (green circles), and nLCE-62 (orange triangles). The birefringence is higher for LCEs with a greater mesogenic content. The nLCE-62 used was synthesised by Matthew Reynolds. This figure has been published by Cooper et al. (1).

To conclude this section, we have examined the thermal behaviour of the refractive indices and the birefringence of a series of monodomain nematic LCEs. We have demonstrated that all the optical properties of these LCEs decrease approximately linearly with temperature, within the range of ~ 25 - 55°C, which is indicative of a density dominated material at these temperatures. Indeed, the temperature coefficients of refractive index for these materials are comparable to the coefficients of acrylate elastomers, showing that the thermal changes to the optical properties are like other optical plastics.

6.5 The Dependence of the Optical Properties on the Composition

Previously, we have seen that the composition has an influence on the refractive indices and the birefringence. Indeed, a higher mesogenic content has been shown to result in both greater refractive indices and birefringence. In the following section, we will consider the average refractive indices of LCEs in the context of how mixing rules might be used as a predictor in this system and shall begin by examining the average refractive indices of two chemically identical materials of different templates.

6.5.1 The Average Refractive Index of Nematic and Isotropic LCEs

We will first examine chemically identical LCEs with different templating, using the composition of 62 mol% mesogenic content. The average refractive index, n_{av}, of a monodomain nematic LCE calculated from Equation 6-1, can be compared to the values measured for the isotropic version of the LCE, n_{iso} (3). Figure 6.6 demonstrates an excellent agreement between the n_{av} and n_{iso} for the monodomain nematic and the isotropic LCEs, respectively. This result validates the use of the geometric average of the anisotropic refractive indices to calculate an average refractive index for the monodomain nematic LCEs and shows that this index is decoupled from the effects of the temperature of polymerisation and order, i.e. it is purely dependent on the chemical composition. This result also confirms that the optical anisotropy should be solely related to the order parameter, a factor which is further examined in the later Section 6.6.1.

The lack of influence of the order parameter on the average refractive index, can be further understood by looking at the mesogenic and non-mesogenic contributions to the refractive indices of the material, where the mesogenic contribution will involve the temperature-dependent order parameter and the density, and the non-mesogenic will involve only the temperature-dependent density. In Figure 6.6, we observe an approximately linear temperature dependence of the averaged refractive index, within the relatively small temperature interval 30 - 50°C.

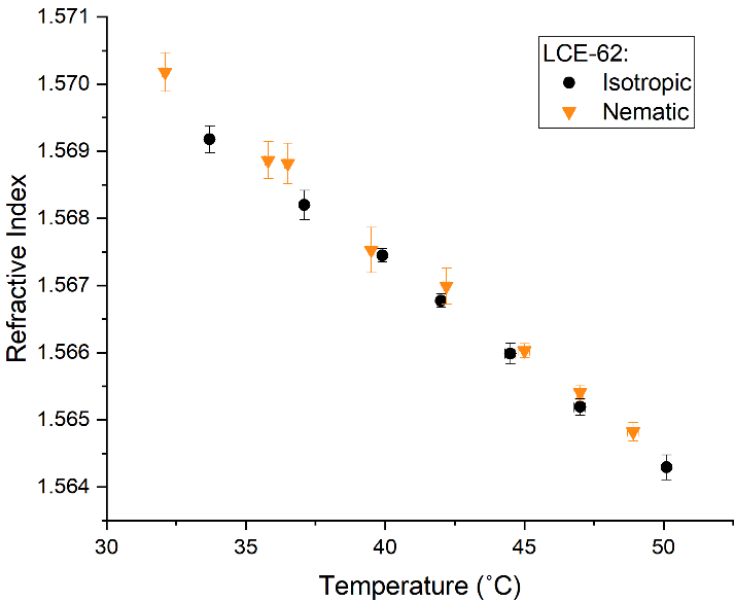

Figure 6.6. The average refractive index deduced for a monodomain nematic LCE (orange triangles) and measured for an isotropic LCE (black circles) of the same chemical composition, with 62 mol% mesogenic content. The indices are measured across the same temperature range. The isotropic LCE used was made by Matthew Reynolds. This figure has been published by Cooper et al. (1).

To conclude this subsection, the average refractive indices of chemically identical monodomain nematic and isotropic LCEs have been shown to have a good agreement, which therefore demonstrate that the average refractive index is solely controlled by the composition. We shall now consider the average refractive indices for a range of LCE compositions, to uncover the tunability of this index.

6.5.2 The Tuneable Average Refractive Index

Here, we will contemplate how the average refractive index of an LCE depends on the relative concentrations of the mesogenic and non-mesogenic components. A similar investigation on the relation between the mesogenic content and the order parameter was previously shown in Section 5.2.1 (Figure 5.1), which gives us good reason to expect a predictable behaviour between the mesogenic content and the refractive indices.

Reis *et al.* (22) describe how the refractive index of a two-component mixture depends on the concentration of each component. Equation 6-2, adapted from the Newton equations (22), relates the average refractive index of the LCE to the mole fraction of mesogenic content, M, the refractive index of pEHA, n_{pEHA}, and a fitting

parameter that describes refractive index of the purely mesogenic material, $n_{mesogen}$.

$$n_{av} = \sqrt{\left((1 - M) \times {n_{pEHA}}^2\right) + \left(M \times {n_{mesogen}}^2\right)} \quad \textit{Equation 6-2}$$

Figure 6.7 demonstrates a good fitting to Equation 6-2 and uses the pEHA refractive index at 0 mol% mesogenic content. This fitting also extracts a parameter which represents the average refractive index of an LCE with 100% mesogenic content, $n_{mesogen}$= 1.634 ± 0.002.

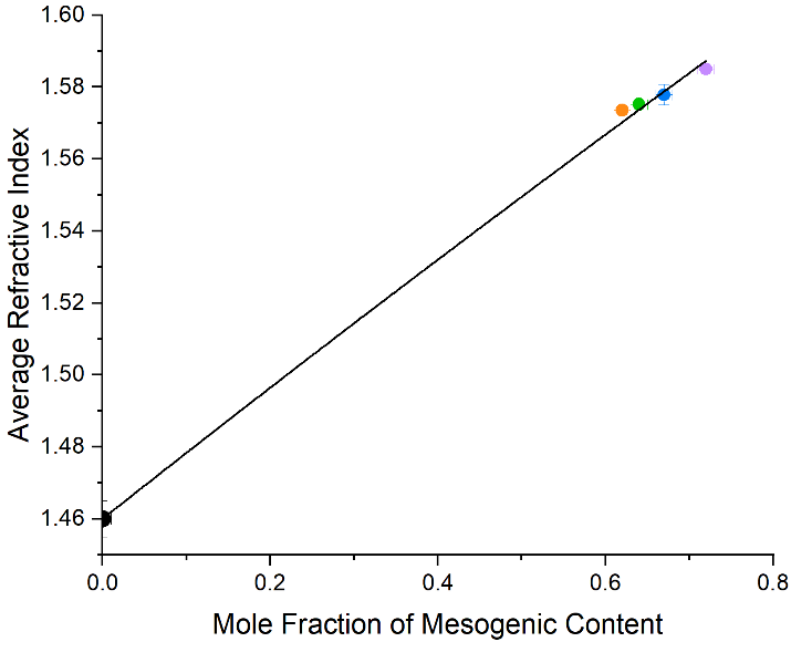

Figure 6.7. The average refractive index of monodomain nematic LCEs and pEHA measured at 25.4 ± 0.4 °C for various mole fractions of mesogenic content. The straight line fit to the data uses Equation 6-2. The data corresponds to nLCE-72 (purple circle), nLCE-67 (blue circle), nLCE-64 (green circle), and nLCE-62 (orange circle). The sample of poly-EHA was made by Stuart Berrow. The nLCE-62 used was synthesised by Matthew Reynolds. This figure has been published by Cooper et al. (1).

Therefore, the average refractive index of a monodomain nematic LCE, and the refractive index of an isotropic LCE, can be directly tuned through composition. Furthermore, this refractive index can be predicted using mixing equations together with a knowledge of the refractive indices of the pure mesogenic and non-mesogenic components.

6.6 The Role of the Order Parameter on the Optical Properties

In Section 6.5.1, the composition clearly had a role in setting the average refractive index of a material, irrespective of the template. In Section 6.4, significant differences in the anisotropic optical properties of monodomain nematic LCEs, such as the birefringence, were observed and attributed to changes in the composition. So in this following section, we will deconvolute the influences of order and composition, by considering the direct impact of the order parameter on the optical anisotropy of the LCEs.

6.6.1 The Optical Anisotropy of Monodomain Nematic LCEs

Here, we will investigate whether the order parameters measured for the different compositions in this series of monodomain nematic LCEs can be directly related to their refractive indices. Such a relationship is commonly used to deduce the temperature dependence of the order parameter from refractive indices in low molar mass liquid crystals (18). Here, a correlation would allow a direct method of controlling the optical anisotropy of the LCEs.

The refractive index anisotropy of a liquid crystal is represented by $\frac{{n_e}^2-{n_o}^2}{{n_{av}}^2-1}$ in Equation 6-3, and relates the refractive indices to the order parameter, $\langle P_2 \rangle$, where $\Delta\alpha = (\alpha_{\parallel} - \alpha_{\perp})$ is the difference in polarizability along the extraordinary and ordinary axes, and $\bar{\alpha} = (\alpha_{\parallel} + 2\alpha_{\perp})/3$ is the average polarizability (18).

$$\langle P_2 \rangle = \frac{\bar{\alpha}}{\Delta\alpha}\left(\frac{{n_e}^2-{n_o}^2}{{n_{av}}^2-1}\right) \qquad \textit{Equation 6-3}$$

The linear interdependence of the refractive index anisotropy, $\frac{{n_e}^2-{n_o}^2}{{n_{av}}^2-1}$, and the order parameter, $\langle P_2 \rangle$ is shown in Figure 6.8, for various monodomain nematic LCEs at room temperature. This analysis uses the order parameters, $\langle P_2 \rangle$, which were previously measured for these compositions in Section 5.2.1

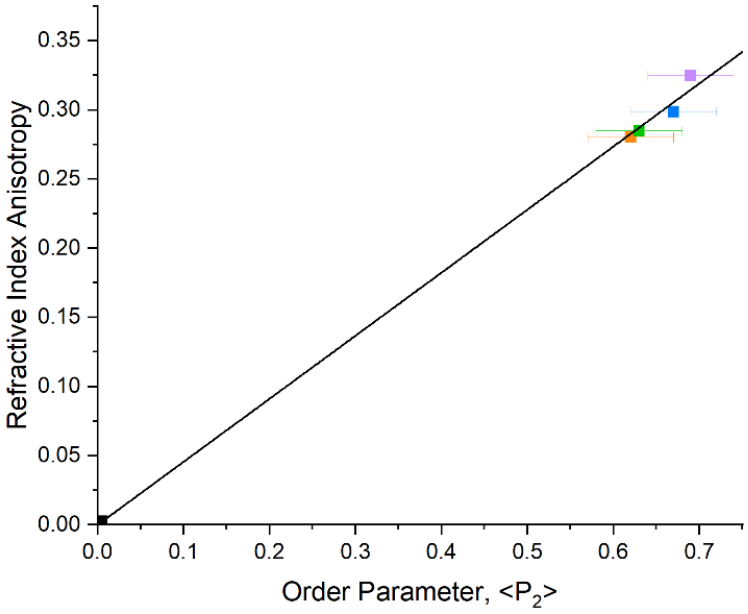

The applicability of Equation 6-3 to this family of LCEs is both useful and interesting. In general, one would not expect the properties of chemically different liquid crystals to be related in this way, rather a single material will follow such behaviour as a function of temperature (18). Indeed, Gleeson *et al.* (18) showed that materials with very different values of birefringence (ranging from ~ 0.05 to ~ 0.2) have extremely similar order parameter behaviour; it is the temperature dependence of the order parameters and refractive index anisotropy that is correlated. The observation that Equation 6-3 can be used for this family of monodomain nematic LCEs is perhaps to be expected as the concentration dependent fitting to the order parameter seen previously in Section 5.2.1 (Figure 5.1) demonstrated that concentration is analogous to the temperature for this system.

6.7 Conclusions

This chapter has demonstrated that a family of highly transparent LCEs can be tuned *via* their composition, enabling control of the optical properties. Through investigations of these optical properties, we have determined factors which may

be used for optical tuning of these materials. The majority of the work within this chapter has been published by Cooper *et al.* (1).

Considering composition first, both n_o and n_e of the monodomain nematic LCEs were shown to increase for an increased mesogenic content of the LCE, with refractive indices changing by up to 0.026 and the birefringence by ~18% for a 10 mol% increase in the mesogenic content. Temperature studies demonstrated a linear variation of the refractive indices, with temperature coefficients of refractive index of the order of 10^{-4} K^{-1}, which is close to literature values for other optical plastics. The linear dependence that was observed, allows us to conclude that for such materials, where a T_{NI} cannot be observed up to 250°C, the temperature dependence of the refractive indices is dominated by changes in the temperature-dependent density.

Furthermore, the average refractive index of the monodomain nematic and isotropic LCEs can be tuned solely *via* composition (order independent) and can be anticipated based on fittings of the Newton equations to the mole fraction of mesogenic content. Finally, we observe that for monodomain nematic LCEs of varied mesogenic content, the relationship between the measured order parameter $\langle P_2 \rangle$ and the refractive index anisotropy can be well predicted. This further demonstrates that the order parameters and optical properties of this acrylate LCE family can be anticipated, which gives the opportunity for precise design.

These results give a detailed insight into the design of auxetic liquid crystal elastomers for a variety of optical applications, including impact resistant glass, where it is desirable to be able to design their average refractive index and the anisotropy, for example, to control the intensity of Fresnel reflections.

The next chapter will expand on the present investigation of the optical properties for this family of LCEs by examining the opacity of the polydomain nematic templated LCE. The polydomain nematic template was not investigated in the present chapter because of the high opacity, which made measurement of the refractive indices, birefringence, and temperature coefficients of refractive index difficult to achieve with the current techniques. Chapter 7 will focus on the evidence of a continuous order-to-disorder transition for the nematic templated materials within this family, and the opacity of a polydomain nematic LCE will contribute to this study.

6.8 References

1. Cooper, E.J., Reynolds, M., Raistrick, T., Berrow, S.R., Jull, E.I.L., Reshetnyak, V., Mistry, D. and Gleeson, H.F. Controlling the Optical Properties of Transparent Auxetic Liquid Crystal Elastomers. *Macromolecules.* 2024, **57**(5), pp.2030-2038. Available from: https://doi.org/10.1021/acs.macromol.3c02226
2. Campo, E.A. 1 - Polymeric Materials and Properties. In: Campo, E.A. ed. *Selection of Polymeric Materials*. Norwich, NY: William Andrew Publishing, 2008, pp.1-39.
3. Mistry, D., Nikkhou, M., Raistrick, T., Hussain, M., Jull, E.I.L., Baker, D.L. and Gleeson, H.F. Isotropic Liquid Crystal Elastomers as Exceptional Photoelastic Strain Sensors. *Macromolecules.* 2020, **53**(10), pp.3709-3718. Available from: https://doi.org/10.1021/acs.macromol.9b02456
4. Kasarova, S.N., Sultanova, N.G. and Nikolov, I.D. Temperature dependence of refractive characteristics of optical plastics. *Journal of Physics: Conference Series.* 2010, **253**(1), p.012028. Available from: https://doi.org/10.1088/1742-6596/253/1/012028
5. Geng, Y., Kizhakidathazhath, R. and Lagerwall, J.P.F. Robust cholesteric liquid crystal elastomer fibres for mechanochromic textiles. *Nature Materials.* 2022, **21**(12), pp.1441-1447. Available from: https://doi.org/10.1038/s41563-022-01355-6
6. Kizhakidathazhath, R., Geng, Y., Jampani, V.S.R., Charni, C., Sharma, A. and Lagerwall, J.P.F. Facile Anisotropic Deswelling Method for Realizing Large-Area Cholesteric Liquid Crystal Elastomers with Uniform Structural Color and Broad-Range Mechanochromic Response. *Advanced Functional Materials.* 2020, **30**(7), p.1909537. Available from: https://doi.org/10.1002/adfm.201909537
7. Geng, Y. and Lagerwall, J.P.F. Multiresponsive Cylindrically Symmetric Cholesteric Liquid Crystal Elastomer Fibers Templated by Tubular Confinement. *Advanced Science.* 2023, **10**(19), p.2301414. Available from: https://doi.org/10.1002/advs.202301414
8. Liu, D., Liu, L., Onck, P.R. and Broer, D.J. Reverse switching of surface roughness in a self-organized polydomain liquid crystal coating.

Proceedings of the National Academy of Sciences. 2015, **112**(13), pp.3880-3885. Available from: https://doi.org/10.1073/pnas.1419312112

9. Feng, W., Broer, D.J. and Liu, D. Oscillating Chiral-Nematic Fingerprints Wipe Away Dust. *Advanced Materials.* 2018, **30**(11), p.1704970. Available from: https://doi.org/10.1002/adma.201704970
10. Mistry, D., Traugutt, N.A., Sanborn, B., Volpe, R.H., Chatham, L.S., Zhou, R., Song, B., Yu, K., Long, K.N. and Yakacki, C.M. Soft elasticity optimises dissipation in 3D-printed liquid crystal elastomers. *Nature Communications.* 2021, **12**(1), p.6677. Available from: https://doi.org/10.1038/s41467-021-27013-0
11. Broer, D.J., Hikmet, R.A.M. and Challa, G. In-situ photopolymerization of oriented liquid-crystalline acrylates, 4. Influence of a lateral methyl substituent on monomer and oriented polymer network properties of a mesogenic diacrylate. *die Makromolekulare Chemie.* 1989, **190**(12), pp.3201-3215. Available from: https://doi.org/10.1002/macp.1989.021901218
12. Broer, D.J., Lub, J. and Mol, G.N. Synthesis and photopolymerization of a liquid-crystalline diepoxide. *Macromolecules.* 1993, **26**(6), pp.1244-1247. Available from: https://doi.org/10.1021/ma00058a007
13. Mistry, D., Connell, S.D., Mickthwaite, S.L., Morgan, P.B., Clamp, J.H. and Gleeson, H.F. Coincident molecular auxeticity and negative order parameter in a liquid crystal elastomer. *Nature Communications.* 2018, **9**(1), p.5095. Available from: https://doi.org/10.1038/s41467-018-07587-y
14. Mistry, D., Morgan, P.B., Clamp, J.H. and Gleeson, H.F. New insights into the nature of semi-soft elasticity and "mechanical-Fréedericksz transitions" in liquid crystal elastomers. *Soft Matter.* 2018, **14**(8), pp.1301-1310. Available from: https://doi.org/10.1039/C7SM02107K
15. Varanytsia, A., Nagai, H., Urayama, K. and Palffy-Muhoray, P. Tunable lasing in cholesteric liquid crystal elastomers with accurate measurements of strain. *Scientific Reports.* 2015, **5**(1), p.17739. Available from: https://doi.org/10.1038/srep17739
16. Roberts, N.W., Guillou, J.P.S., Gleeson, H.F., Kirar, I., Watson, S.J. and Arikainen, E.O. Optical Properties of Cholesteric Materials used in Surface Stabilised Cholesteric Texture Devices. *Molecular Crystals and Liquid*

Crystals. 2004, **411**(1), pp.57-70. Available from: https://doi.org/10.1080/15421400490434793

17. Tašič, B., Li, W., Sánchez-Ferrer, A., Čopič, M. and Drevenšek-Olenik, I. Light-Induced Refractive Index Modulation in Photoactive Liquid-Crystalline Elastomers. *Macromolecular Chemistry and Physics.* 2013, **214**(23), pp.2744-2751. Available from: https://doi.org/10.1002/macp.201300493
18. Gleeson, H.F., Southern, C.D., Brimicombe, P.D., Goodby, J.W. and Görtz, V. Optical measurements of orientational order in uniaxial and biaxial nematic liquid crystals. *Liquid Crystals.* 2010, **37**(6-7), pp.949-959. Available from: https://doi.org/10.1080/02678292.2010.488818
19. Vuks, M.F. Determination of the optical anisotropy of aromatic molecules from the double refraction of crystals. *Optics and Spectroscopy.* 1966, **20**.
20. Averina, L.M. and Milyavskii, Y.S. Temperature dependence of the refractive index of acrylate elastomers. *Journal of Optical Technology.* 2004, **71**(4), pp.249-250. Available from: https://doi.org/10.1364/JOT.71.000249
21. Averina, L.M., Kravchenko, V.B., Milyavskii, Y.S., Nanushyan, S.R., Simanovskaya, E.I. and Feld, S.Y. Investigation of temperature dependences of optical polymer characteristics for lightguides of the glass-polymer type. *Zhurnal Tekhnicheskoi Fiziki.* 1985, **55**(8), pp.1605-1611.
22. Reis, J.C.R., Lampreia, I.M.S., Santos, Â.F.S., Moita, M.L.C.J. and Douhéret, G. Refractive Index of Liquid Mixtures: Theory and Experiment. *ChemPhysChem.* 2010, **11**(17), pp.3722-3733. Available from: https://doi.org/10.1002/cphc.201000566

Chapter 7 Evidence of an Order-to-Disorder Transition in Nematic LCEs

7.1 Introduction

As aforementioned in Section 2.3, the nematic-to-isotropic transition temperature, T_{NI}, of a thermotropic mesogen is well known to be a typically weak first order transition (1). For such materials, Differential Scanning Calorimetry (DSC) is an often-used technique to measure the transition temperatures. In Section 4.3.1, we used DSC to measure the T_{NI} of the LCE precursor mixtures (prior to polymerization) and these exhibited a linearly relationship with the mesogenic content that has previously been reported in literature (2-4).

However, a nematic-to-isotropic transition has not been observed for the polymerized nematic LCEs in this family using either DSC or Polarized Optical Microscopy (POM). In fact, the absence of a nematic-to-isotropic transition has been well reported for this family, given that these materials undergo degradation before a transition can be observed (2, 5-7). In the previous chapters, particularly in Section 4.2.1, we proved that a first order transition cannot be detected for any of the nematic LCE templates. Furthermore, we showed that the macroscopic behaviour of a polydomain nematic LCE was thermally identical to isotropic LCEs, which was particularly evident through the characterisation of the thermal shape change of the materials and by studying the heat flow with DSC.

Therefore, in the following short chapter, we will search for any evidence of a nematic-to-isotropic transition for the monodomain and polydomain nematic LCEs, and to seek to answer two key questions:

i. Does such a transition occur in these polydomain and monodomain nematic LCEs?
ii. And, if such a transition does exist, what is its nature?

Before we search for a transition in the nematic materials of this family, we must first discuss the observed nature and the influencing factors of this transition for other families of LCEs.

7.1.1 Nematic-to-Isotropic Transitions in LCEs

As mentioned earlier, the nematic-to-isotropic transition temperature, T_{NI}, of a liquid crystalline material is typically a first order, discontinuous, transition (8). Discontinuous transitions into an isotropic phase are also possible for crosslinked liquid crystalline materials such as LCEs, however a change in the nature of this transition has been observed in the presence of a sufficiently strong magnetic, electrical, or mechanical field (1). For an applied field with a magnitude below a critical strength, $\sigma_{critical}$, the order parameter of the LCE has been seen to discontinuously transition into what is referred to as a '*paranematic'* phase with low, non-zero order (1). However, for an LCE with an applied field above $\sigma_{critical}$, the order parameter at the transition has been observed to reduce continuously and, interestingly, has not been attributed to either a first or a second order transition (1, 9). This transition shall be described as an order-to-disorder transition and a schematic of each of these three forms of the order-to-disorder transition are shown in Figure 7.1.

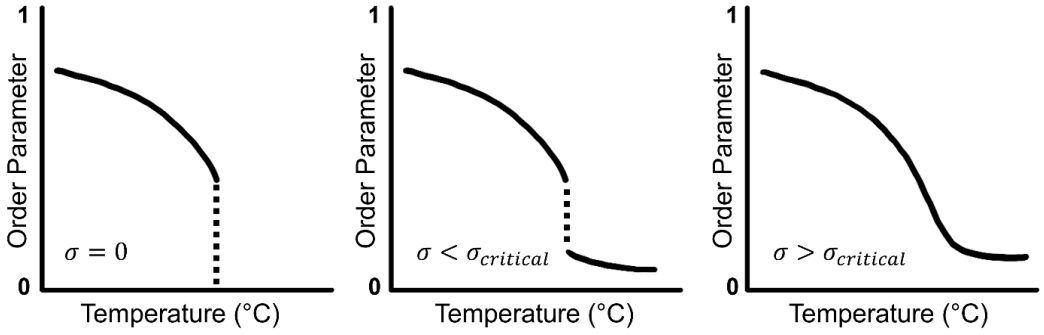

Figure 7.1. A schematic of the reducing order parameter during an order-to-disorder transition of a crosslinked liquid crystalline network for three scenarios: with no applied field ($\sigma = 0$), with an applied field below a critical strength ($\sigma < \sigma_{critical}$), and an applied field above a critical strength ($\sigma > \sigma_{critical}$). For no applied field, or an applied field below a critical strength, the observed transition is discontinuous. Above a critical field strength, the observed transition is continuous. For the situation of $\sigma < \sigma_{critical}$, the material transitions into a 'paranematic phase' of non-zero order (1). This schematic is based on previous modelling by Selinger et al. (9).

7.1.2 Internal Strain in Monodomain Nematic LCEs

In this short section, we will discuss what we know about the internal strain field of these LCEs and whether this field has an influence on the transition. In Section 5.4.3, a reduction in the network spacing was attributed to an increase in the internal

strain of the LCEs. We reasoned that an internal strain field is present for these materials, since our reduction in spacing was comparable to reports for smectic LCEs, where reductions were due to the crosslinking density (10), applied electric field (11) and applied strain, relaxation and heating (12). Further discussion on the evidence of an internal strain field was given in Section 5.4.3.

Perhaps surprisingly, the critical strength of a mechanical field required to cause a continuous transition of an LCE, has previously been achieved from solely the crosslinking (1, 13) and the swelling (14) of the network. Knowing that the internal strain is significant to the network structure, we need to explore the possibility that there is a sufficient internal strain in the nematic LCEs considered in this work to produce a continuous order-to-disorder transition. In fact, the results within this chapter will support the case that a sufficiently large internal strain causes a continuous transition in the nematic templated LCEs. This investigation will solely involve the nematic LCEs of 62 mol% mesogenic content, since the properties of this material have been well recorded throughout this thesis and in literature (2, 5-7).

7.2 Order Parameter

Here we will investigate the order parameters of a monodomain nematic LCE (nLCE-62) at different temperatures. The temperature-dependent order parameter was briefly introduced in Section 5.3.2, but the raw data was not provided; the full results will be reported shortly in Section 7.2.2.

The method used for measuring the temperature-dependent order parameters is already described in Section 3.4.1, with a further step of placing the sample on a glass coverslip coated with a small amount of silicon oil to prevent contact between the surfaces. This method has been shown as effective to stop any induced strain on the sample during heating and has been used during the thermal shape change investigations in Sections 4.2.1 and 5.3.1. The coverslip was placed on a Linkam HFS600 hot stage connected to a Linkam TMS 94 controller to regulate the temperature. The measurements using Raman Spectroscopy were taken once the LCE had been held at the desired temperature for 10 minutes to ensure that the sample was investigated at a constant temperature.

7.2.1 The Effect of Silicon Oil and Elevated Temperature

As aforementioned, silicon oil was used between the LCE and the coverslip whilst investigating the impact of the temperature on the order parameters. As a control, we need to ensure that there is no influence from the silicon oil on the LCE during the order parameter measurements and we also need to ensure that there is no impact from holding the LCE at an elevated temperature. The order parameters of nLCE-62 have been well reported (2, 7, 15, 16) which makes this material highly suitable for the following investigation.

Firstly, the influence of the silicon oil on the material and the order parameter measurements shall be investigated. To be clear, we do not expect any significant influence of the silicon oil on the material, however it is important to validate this for an experimental control. The order parameters of nLCE-62 were investigated at room temperature (22°C) without silicon oil and were measured as $\langle P_2 \rangle = 0.62 \pm 0.05$ and $\langle P_4 \rangle = 0.31 \pm 0.05$. We measured similar order parameters of $\langle P_2 \rangle = 0.65 \pm 0.05$ and $\langle P_4 \rangle = 0.31 \pm 0.05$, for the same sample, on silicon oil and held at 25°C with a temperature-controller. We can therefore conclude that the silicon oil has no influence on the order parameters that are measured for experiments at relatively low temperatures.

We shall now consider the effect of an elevated temperature on nLCE-62, whilst the sample is on silicon oil. Here, we want to make sure that there is no deterioration of the material and the oil due to prolonged elevated temperatures. Truthfully, we do not expect there to be any impact of an elevated temperature on the material, since we know that the LCEs can be cyclically heated to 250°C with no signs of deterioration, however we have not yet investigated the effect of temperature on the silicon oil.

This investigation uses the methodology described above to measure the order parameters of nLCE-62 (on silicon oil) at an elevated temperature of 100°C. After the material was held at 100°C for 10 minutes, the order parameters were measured and recorded at time t_1. The temperature of the material was fixed at 100°C for a further 4 hours and the order parameters were remeasured at time t_2.

Figure 7.2 shows the fittings of the depolarization ratio for nLCE-62 at time t_1 and t_2; the depolarization ratio was previously introduced in Section 2.4.2. As expected,

Figure 7.2 shows that the elevated temperature has no effect of the order parameters of nLCE-62 (on silicon oil), since the order parameters show a good agreement at both times.

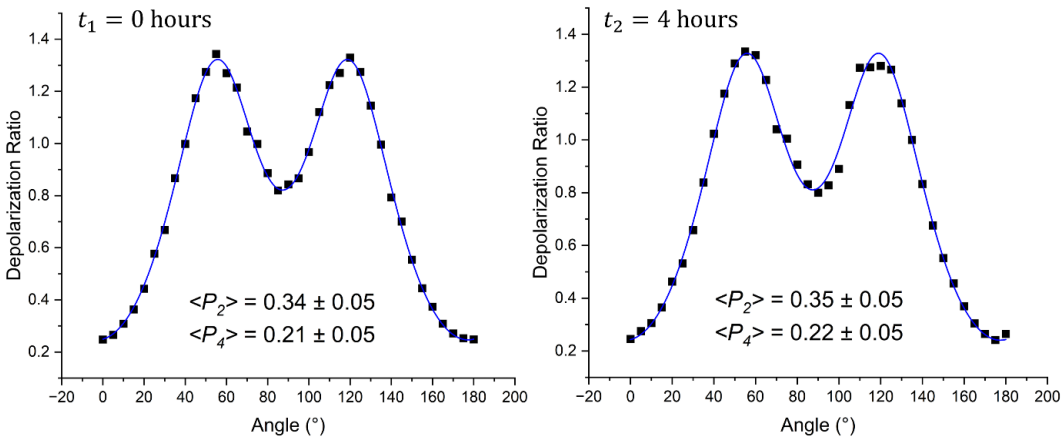

Figure 7.2. The fitting of the depolarization ratio for a monodomain nematic LCE of 62 mol% mesogenic content (nLCE-62), at an elevated temperature of 100°C and measured at time t_1 (0 hours) and t_2 (4 hours). The depolarization ratio is fitting according to the methodology outlined in Section 2.4.2.

Now that we have confirmed that the silicon oil has no effect on the measurements of the order parameter, and that the sample and the oil do not degrade when held at an elevated temperature, we can now measure the order parameters of the LCE for an increasing temperature.

7.2.2 The Temperature-Dependent Order Parameters of nLCE-62

The method to measure the order parameters of the monodomain nematic LCE of 62 mol% mesogenic content (nLCE-62) follows the method described above in Section 7.2. Figure 7.3 shows the order parameters, which were measured in regular increments between 25°C and 135°C. We clearly see a reduction in the order parameters, with the greatest change in order seen for $\langle P_2 \rangle$.

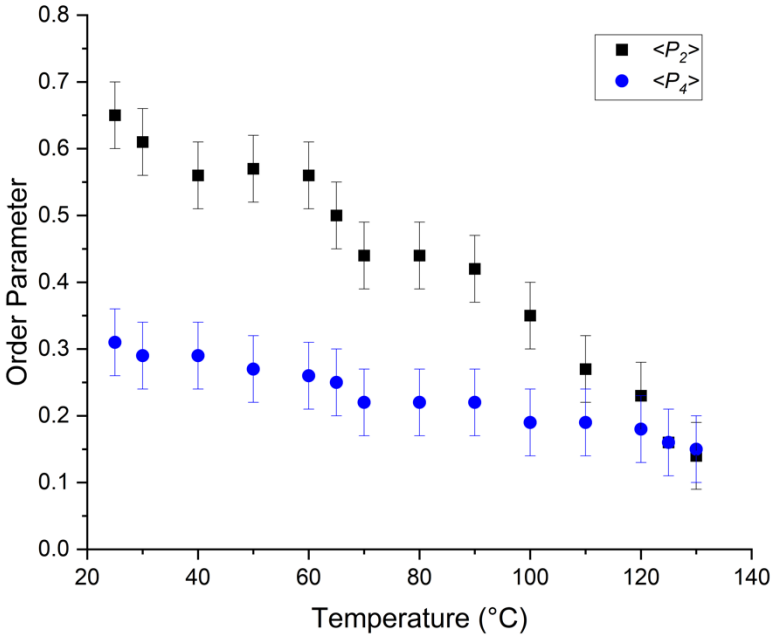

Figure 7.3. The temperature-dependent order parameters, $\langle P_2 \rangle$ (black squares) and $\langle P_4 \rangle$ (blue circles), of a monodomain nematic LCE of 62 mol% mesogenic content (nLCE-62) between 25°C and 135°C. These measurements were made using Raman Spectroscopy.

A summary of the temperature-dependent order parameters is given in Table 7-1 below. In line with our previous predictions in Section 6.4, there is a relatively small change in the order parameters below ~ 50°C, where the value of $\langle P_2 \rangle$ drops from 0.65 ± 0.05 to 0.57 ± 0.05. However, we clearly see that $\langle P_2 \rangle$ significantly reduces at higher temperatures, such that $\langle P_2 \rangle$ = 0.14 ± 0.05 at 130°C. The material was in fact investigated to 135°C, however the order of the material was too low to be measured above 130°C. We will now investigate whether a continuous or a discontinuous transition is occurring in this material.

Table 7-1. The temperature-dependent order parameters, $\langle P_2 \rangle$ and $\langle P_4 \rangle$, of the monodomain nematic LCE of 62 mol% mesogenic content (nLCE-62), which have been measured between 25°C and 135°C. The order parameters could not be measured at 135°C, due to low ordering.

Temperature (± 1°C)	**$\langle P_2 \rangle$ (± 0.05)**	**$\langle P_4 \rangle$ (± 0.05)**
25	0.65	0.31
30	0.61	0.29
40	0.56	0.29
50	0.57	0.27
60	0.56	0.26
65	0.5	0.25
70	0.44	0.22
80	0.44	0.22
90	0.42	0.22
100	0.35	0.19
110	0.27	0.19
120	0.23	0.18
125	0.16	0.16
130	0.14	0.15
135	N/A	N/A

We shall now consider whether a typical Haller model (17) would suitably fit to $\langle P_2 \rangle$ in Figure 7.3. The well-known Haller model was outlined in Equation 2-3 in Section 2.4 and revisited in Equation 5-1 in Section 5.2.1. This model fits to the temperature in Kelvin (T), with a critical temperature typically just above T_{NI} (T^*), and an exponent fitting constant (τ) (17). The exponent fitting constant may show a slight variation across liquid crystalline materials but is expected to have values of 0.17- 0.23 (17).

The Haller model has been fitted to the order parameter, $\langle P_2 \rangle$, in Figure 7.4 below and provides fitting parameters of $\tau = 0.36 \pm 0.02$ and $T^* = 398 \pm 3$ K (125 ± 3 °C). By first examining the exponent fitting constant, τ, we notice a significantly higher than expected value for a liquid crystalline material, which strongly suggests that the Haller model, derived for a discontinuous transition, is not an appropriate fitting for this system. Secondly, the critical temperature, T^*, suggests a nematic-to-isotropic transition around 125 °C, however, we have experimentally measured order parameters of $\langle P_2 \rangle > 0$ above this temperature. This further supports the

working theory of a continuous transition into a '*paranematic*' phase for this material since we measure a non-zero order parameter above an effective order-to-disorder transition temperature (T^*). If this is indeed the case, we know that there must be sufficient internal strain within the network to cause a continuous transition.

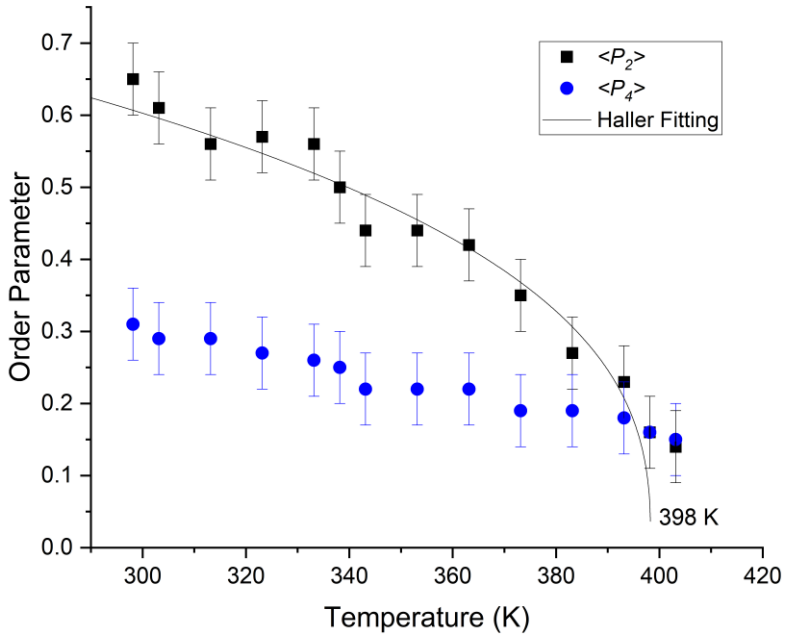

Figure 7.4. The temperature-dependent order parameters, $\langle P_2 \rangle$ (black squares) and $\langle P_4 \rangle$ (blue circles), of the monodomain nematic LCEs of 62 mol% mesogenic content (nLCE-62), which have been measured between 25°C and 135°C – note that the temperature is in Kelvin. The order parameters could not be measured at 135°C, due to low ordering. The Haller model (black line) has been fitted to $\langle P_2 \rangle$ and indicates fitting parameters of τ = 0.36 ± 0.02 and T^* = 398 ± 3 K (125 ± 3 °C).

Our last consideration in the order parameter investigation is to compare the order parameters of nLCE-62 to Maier-Saupe theory, which has been similarly investigated in literature (18-22) and was also considered earlier in Sections 5.2.1 and 5.2.2 for a series of LCEs with varied composition. Figure 7.5 shows the Maier-Saupe theory (black line) compared to the order parameters of nLCE-62 at increasing temperatures, with the lowest temperature of 25°C shown in blue and the highest temperature of 130°C shown in red.

We clearly observe that at lower temperatures, the order parameters have a good agreement to the Maier-Saupe theory. However, we see significant deviation from the Maier-Saupe theory at temperatures above 60°C. Interestingly, the temperature range between ~ 25°C to ~ 60°C was predicted in Section 6.4 to have order

parameters that show relatively little variation, which we also observe in Figure 7.3. Therefore, within this temperature range around ambient conditions, we know that there is not a significant variation in the order parameters, and that the order parameters are in good agreement with Maier-Saupe theory. At the higher temperatures of Figure 7.5, the deviation from the Maier-Saupe theory is likely due to the occurrence of a transition from an ordered phase to a more disordered phase.

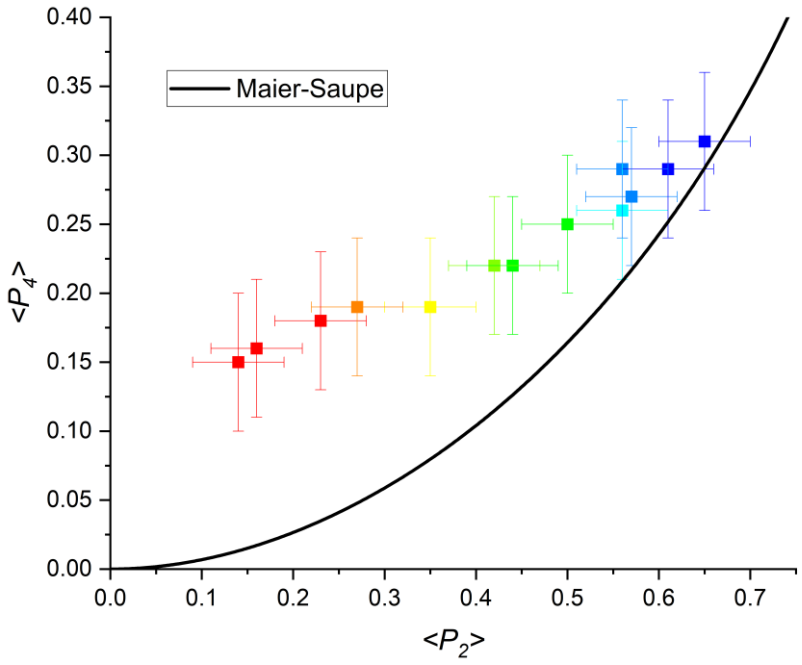

Figure 7.5. A comparison of the order parameters, $\langle P_2 \rangle$ and $\langle P_4 \rangle$, measured using Raman Spectroscopy for nLCE-62 (squares) and Maier-Saupe theory (black line) (18-22). At lower temperatures (blue), we see good agreement of the order parameters to the Maier-Saupe theory, however we clearly see deviation from the theory at higher temperatures (red). The order parameters are measured at increasing temperatures from right to left. The Maier-Saupe fitting was provided by Thomas Raistrick.

7.3 Transmission Spectrometry

So far, we have investigated evidence of an order-to-disorder transition in a monodomain nematic LCE; we shall now consider whether there is evidence of a transition in a polydomain nematic LCE. As aforementioned in Chapter 6, the polydomain nematic template in this family of LCEs appears opaque at room temperature. We also know from Section 4.2.1 that this material shows an isotropic shape change that is simply accounted for by the thermal expansion of the material. Not previously mentioned in Section 4.2.1, is that during the thermal shape change investigations, the polydomain nematic LCE exhibited an intriguing decrease in opacity with an increase in temperature, suggesting a transition to an disordered

phase. Therefore, in this section, we will explore whether the change in opacity of the polydomain nematic LCE is in fact evidence of an order-to-disorder transition.

In the following work, a polydomain nematic LCE of 62 mol% mesogenic content was used. The methodology used here has been described previously in Section 3.5.2, and involved a small sample of the LCE placed directly on a coverslip; we know from Section 4.2.1 that there is not a significant thermal shape change for this template to 150°C, particularly when compared to the shape change seen in the monodomain nematic LCE, so no silicon oil was used here.

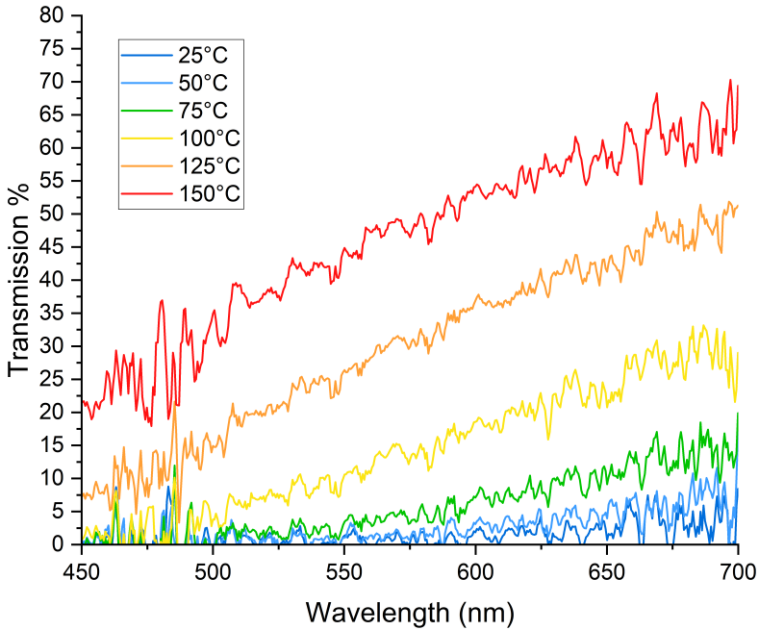

Figure 7.6. The transmission spectrum of a polydomain nematic LCE of 62 mol% mesogenic content, at temperatures between 25°C and 150°C, in 25°C increments. The transmission clearly increases as the material is heated.

Figure 7.6 shows the transmission spectra of the polydomain nematic LCE at temperatures between 25°C and 150°C, in 25°C steps. Critically, across the spectra we observe an increase in the optical transparency of the material due to an increase in the temperature. We also observe larger increases in the transparency at higher temperatures; the optical transmission of the material does not appear to linearly increase with temperature.

We shall now consider the changes in the transmission of the polydomain nematic material for a particular wavelength of 589 nm, which was selected to complement previous studies with the Abbé Refractometer at 589 nm. Figure 7.7 shows the

transmission of the material at shorter temperature intervals (5 - 10°C) between 25°C and 160°C. Interestingly, Figure 7.7 clearly shows a sharp change in the transmission at ~ 86°C, which was measured by the intercept of linear fittings to the surrounding data. This change in the transmission could be indicative of an onset of the continuous order-to-disorder transition.

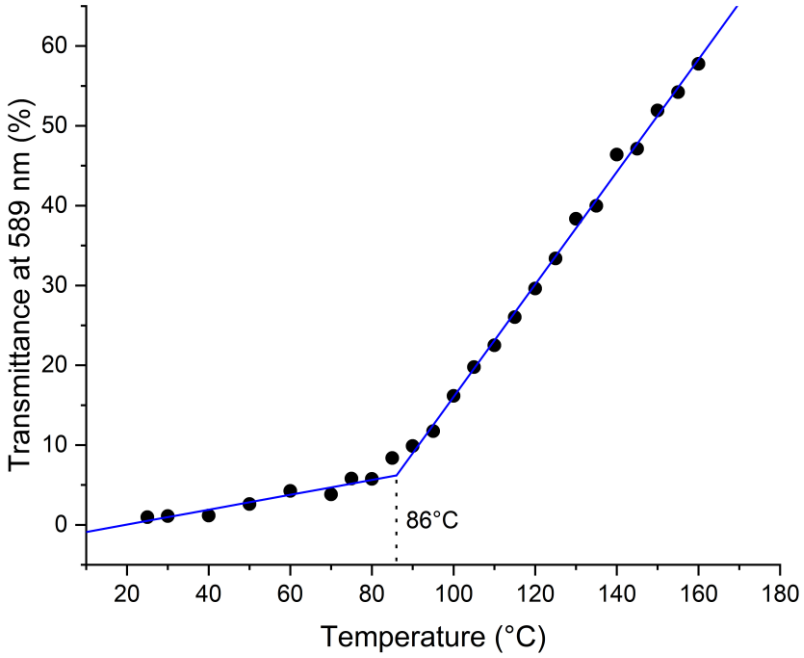

Figure 7.7. The transmission of a polydomain nematic LCE of 62 mol% mesogenic content. The transmission was measured as ~ 1% at 25°C and increased to ~ 58% at 160°C. We clearly observe the transmission of the material to sharply increase at 86°C, determined by the intercept of two linear fittings.

7.4 Summary

Throughout this thesis, we have consistently demonstrated that the nematic templates within this family show no clear evidence of a nematic-to-isotropic transition. In fact, the polydomain nematic template has regularly behaved thermally like an isotropic template, and the behaviour has been distinctive from the monodomain nematic template. Yet, in this chapter we have shown evidence of a continuous order-to-disorder transition in both of the nematic templates for this family of LCEs.

At the start of this chapter, we sought to answer two questions: does an order-to-disorder transition exist in the polydomain and monodomain nematic LCEs, and if such a transition does occur, what is its nature? Below we shall summarise the proof

of a continuous order-to-disorder transition in both of the nematic templated LCEs within this family.

Using Raman Spectroscopy, the temperature-dependent order parameters of a monodomain nematic material (nLCE-62) were shown to significantly decrease upon heating to 135°C. In fact, an order parameter at 135°C could not be quantified, which has been attributed to a low ordering. We demonstrated that the Haller model, a model typically used for liquid crystals, is not suitable for this material; the exponent fitting constant, τ, was much larger than expected and the critical temperature, T^*, indicated a transition to an isotropic phase occurring at ~ 125°C, despite having measurable order parameters above this temperature.

We also demonstrated that the opaque polydomain nematic template of nCLE-62 increases in transparency with an increase in temperature, such that the transmission changes from ~ 1% at 25°C to ~ 58% at 160°C. We also observed a sudden increase in the transparency at ~ 86°C, which could indicate an onset of the transition in the polydomain nematic material.

For a continuous transition to indeed occur in these materials, there must be an applied field of sufficient strength. In line with findings in literature (1, 13), we believe that the crosslinking of these LCEs provides a strong internal strain field. Previously in Section 5.4.3, we observed changes to the network structure for LCEs of different composition, in a manner that has been similarly observed for smectic LCEs with changes to field strength (due to the crosslinking density (10), and applied electric field (11), strain, relaxation, and heating (12)). Therefore, the nematic templated LCEs in this acrylate family, show evidence of a continuous order-to-disorder transition to a paranematic phase, that occurs due to a strong internal strain generated by the crosslinking.

Lastly, more evidence is needed to establish the exact transition temperatures associated with the order-to-disorder transition. The transitions of the polydomain and the monodomain nematic templates need to be further examined and compared to determine whether these materials do in fact share comparable transitions despite very few similarities in their thermal behaviour. Further work would also involve investigating a range of compositions of nLCEs to identify the role of the internal strain on the transition, since we know that the internal strain does indeed vary with

composition. This work will be discussed in the ensuing conclusions chapter, since collaborations are in progress with Victor Reshentyak to model the internal strain of these materials. Additionally, a series of similar LCEs with a varied crosslinking density have been developed by Thomas Raistrick and Matthew Reynolds; this series of materials will provide further insight into the role of crosslinking on the internal strain field. A paper on this collaborative work is in preparation.

7.5 References

1. Disch, S., Schmidt, C. and Finkelmann H. Nematic elastomers beyond the critical point. *Macromolecular Rapid Communications.* 1994, **15**, pp.303-310. Available from: https://doi.org/10.1002/marc.1994.030150402
2. Cooper, E.J., Reynolds, M., Raistrick, T., Berrow, S.R., Jull, E.I.L., Reshetnyak, V., Mistry, D. and Gleeson, H.F. Controlling the Optical Properties of Transparent Auxetic Liquid Crystal Elastomers. *Macromolecules.* 2024, **57**(5), pp.2030-2038. Available from: https://doi.org/10.1021/acs.macromol.3c02226
3. Barnes, M., Cetinkaya, S., Ajnsztajn, A. and Verduzco, R. Understanding the effect of liquid crystal content on the phase behavior and mechanical properties of liquid crystal elastomers. *Soft Matter.* 2022, **18**(27), pp.5074-5081. Available from: https://doi.org/10.1039/D2SM00480A
4. Jull, E.I.L., Mandle, R.J., Raistrick, T., Zhang, Z., Hine, P.J. and Gleeson, H.F. Toward In Silico Design of Highly Tunable Liquid Crystal Elastomers. *Macromolecules.* 2022, **55**(11), pp.4320-4330. Available from: https://doi.org/10.1021/acs.macromol.2c00587
5. Mistry, D., Morgan, P.B., Clamp, J.H. and Gleeson, H.F. New insights into the nature of semi-soft elasticity and "mechanical-Fréedericksz transitions" in liquid crystal elastomers. *Soft Matter.* 2018, **14**(8), pp.1301-1310. Available from: https://doi.org/10.1039/C7SM02107K
6. Raistrick, T. *Understanding the mechanical behaviour of novel liquid crystal elastomers*. PhD thesis, University of Leeds, 2022.
7. Berrow, S.R., Raistrick, T., Mandle, R.J. and Gleeson, H.F. Structure–Property Relationships in Auxetic Liquid Crystal Elastomers—The Effect of Spacer Length. *Polymers.* 2024, **16**(14), p.1957. Available from: https://www.mdpi.com/2073-4360/16/14/1957

8. Collings, P.J. and Goodby, J.W. Introduction to Liquid Crystals : Chemistry and Physics, Second Edition. In: Milton, UNITED KINGDOM: Taylor & Francis Group, 2019, pp.pp 95-136.
9. Selinger, J.V., Jeon, H.G. and Ratna, B.R. Isotropic-Nematic Transition in Liquid-Crystalline Elastomers. *Physical Review Letters.* 2002, **89**(22), p.225701. Available from: https://doi.org/10.1103/PhysRevLett.89.225701
10. Liang, T., van Kuringen, H.P.C., Mulder, D.J., Tan, S., Wu, Y., Borneman, Z., Nijmeijer, K. and Schenning, A.P.H.J. Anisotropic Dye Adsorption and Anhydrous Proton Conductivity in Smectic Liquid Crystal Networks: The Role of Cross-Link Density, Order, and Orientation. *ACS Applied Materials & Interfaces.* 2017, **9**(40), pp.35218-35225. Available from: https://doi.org/10.1021/acsami.7b09386
11. Spillmann, C.M., Konnert, J.H., Deschamps, J.R., Naciri, J. and Ratna, B.R. Molecular Packing in Electroclinic Liquid Crystal Elastomer Films. *Chemistry of Materials.* 2008, **20**(19), pp.6130-6139. Available from: https://doi.org/10.1021/cm801335j
12. Dey, S., Agra-Kooijman, D.M., Ren, W., McMullan, P.J., Griffin, A.C. and Kumar, S. Soft Elasticity in Main Chain Liquid Crystal Elastomers. *Crystals.* 2013, **3**(2), pp.363-390. Available from: https://www.mdpi.com/2073-4352/3/2/363
13. Cordoyiannis, G., Lebar, A., Zalar, B., Žumer, S., Finkelmann, H. and Kutnjak, Z. Criticality Controlled by Cross-Linking Density in Liquid Single-Crystal Elastomers. *Physical Review Letters.* 2007, **99**(19), p.197801. Available from: https://doi.org/10.1103/PhysRevLett.99.197801
14. Lebar, A., Kutnjak, Z., Žumer, S., Finkelmann, H., Sánchez-Ferrer, A. and Zalar, B. Evidence of Supercritical Behavior in Liquid Single Crystal Elastomers. *Physical Review Letters.* 2005, **94**(19), p.197801. Available from: https://doi.org/10.1103/PhysRevLett.94.197801
15. Berrow, S.R., Mandle, R.J., Raistrick, T., Reynolds, M. and Gleeson, H.F. Toward Monodomain Nematic Liquid Crystal Elastomers of Arbitrary Thickness through PET-RAFT Polymerization. *Macromolecules.* 2024, **57**(11), pp.5218-5229. Available from: https://doi.org/10.1021/acs.macromol.4c00245

16. Raistrick, T., Zhang, Z., Mistry, D., Mattsson, J. and Gleeson, H.F. Understanding the physics of the auxetic response in a liquid crystal elastomer. *Physical Review Research.* 2021, **3**(2), p.023191. Available from: https://doi.org/10.1103/PhysRevResearch.3.023191
17. Haller, I. Thermodynamic and static properties of liquid crystals. *Progress in Solid State Chemistry.* 1975, **10**, pp.103-118. Available from: https://doi.org/10.1016/0079-6786(75)90008-4
18. Maier, W. and Saupe, A.Z. Eine einfache molekulare Theorie des nematischen kristallinflüssigen Zustandes. *Naturforsch.* 1958, **13a**, pp.564-566.
19. Maier, W. and Saupe, A.Z. Eine einfache molekular-statistische Theorie der nematischen kristallinflüssigen Phase. Teil 1[1]. *Naturforsch.* 1959, **14a**, pp.882–889.
20. Maier, W. and Saupe, A.Z. Eine einfache molekular-statistische Theorie der nematischen kristallinflüssigen Phase. Teil II. *Naturforsch.* 1960, **15a**, pp.287–292.
21. Zannoni, C. Order Parameters and Orientational Distributions in Liquid Crystals. In: Samori, B. and Thulstrup, E.W. eds. *Polarized Spectroscopy of Ordered Systems*. Dordrecht: Springer Netherlands, 1988, pp.57-83.
22. Andrienko, D. Introduction to liquid crystals. *Journal of Molecular Liquids.* 2018, **267**, pp.520-541. Available from: https://doi.org/10.1016/j.molliq.2018.01.175

Chapter 8 Conclusion and Future Work

8.1 Summary of Key Results

To conclude the research presented in this thesis, a short summation of the critical results shall be provided here. Later portions of this conclusion chapter will consider the optimal material template and composition for a laminate in impact resistant glass and following this, future avenues of further work will be suggested.

In this work, we focused on the role of templating and composition on the material properties of a series of LCEs. The templates of LCEs that were considered included the polydomain nematic, the monodomain nematic, and the isotropic. The compositions of polymerized LCEs ranged between 51 mol% and 84 mol% mesogenic content. A deep understanding of the role of templating and composition on the material characteristics has been realised in this work; the key results shall be outlined according to each chapter below.

Firstly, the fundamental thermal behaviour of the various LCE templates was investigated in Chapter 4. This was an essential start to the investigation to understand the key thermal characteristics and the formulation limitations of each of the LCE templates. During this study, both Differential Scanning Calorimetry (DSC) and the thermal shape change of the materials demonstrated that the isotropic and the polydomain nematic templates exhibit indistinguishable thermal behaviour, which are altogether different from the behaviour of the monodomain nematic template.

To provide the formulation limitations of the materials, Differential Scanning Calorimetry (DSC) was used to measure the transition temperatures (T_{NI} and T_g) of the precursor LCE mixtures and the corresponding polymerized films. Notably, a T_{NI} of the polymerized nematic LCEs could not be measured. All the transition temperatures measured demonstrated an increase with mesogenic content in line with previous literature that altered the liquid crystalline content and the crosslinker density of LCEs (1, 2). The T_{NI} of the precursor LCE mixtures were all above ~ 28°C, which enabled a nematic phase LCE to be polymerized at room temperature. Furthermore, a T_g of the polymerized LCEs below ~ 16°C resulted in rubbery LCEs at room temperature.

Later in Chapter 4, the impact of templating and composition on the dissipative properties was explored. Each template exhibited good dissipative capabilities around room temperature, however only the monodomain nematic templated LCEs displayed an auxetic response. Interestingly, the monodomain nematic LCEs of the lowest (nLCE-56) and the highest (nLCE-72) mesogenic content did not exhibit an auxetic response before failure. This suggests that there are further formulation limitations present for these materials, and that nLCE-56 and nLCE-72 are outside of the monodomain nematic LCE limitations for an auxetic response. In line with discussions by Berrow *et al.* for a similar series of materials (3), this indicates a degree of smecticity in nLCE-72, which was further investigated in Chapter 5.

The limitations of the composition of monodomain nematic LCEs were further explored in the following chapter, Chapter 5, using Raman Spectroscopy and X-ray Scattering. Additional formulation limitations were established, with a > 55 mol% mesogenic content required to form a stable and ordered nematic phase (with no sign of phase separation). Specifically, this limit was determined by the observed phase separation of LCEs with < 55 mol% mesogenic content, and also with a concentration-dependent fitting to the order parameters measured with Raman Spectroscopy.

The latter section of Chapter 5 probed the structure of the transparent materials (isotropic and monodomain nematic) using Small- and Wide- Angle X-ray Scattering (SAXS and WAXS). Several scattering features were found amongst the monodomain nematic and isotropic LCEs, and these features were more apparent when considering the intensity normalised by the thickness. Using a reduced thickness also emphasized that a greater normalised scattering intensity arises for lower mesogenic content nematic LCEs.

Several scattering features were observed using SAXS and WAXS and all features exhibited anisotropy. The scattering features measured at $q \sim 1.5$ nm^{-1}, 5 nm^{-1}, and 14 nm^{-1} were of particular interest due to their high scattering intensity and strongly anisotropic nature. The feature at $q \sim 14$ nm^{-1} was attributed to the side-to-side scattering of the network and was used to determine an order parameter for the material. The feature at $q \sim 5$ nm^{-1} was suggested to be due to the scattering from the length of the side group, EHA.

The feature at q ~ 1.5 nm^{-1} was attributed to an end-to-end layer distance, parallel to the director, and corresponded to a spacing of ~ 39 - 42 Å. The material nLCE-72 demonstrated the closest layer spacing of 39 Å, which was comparable to the spacing of the 'smectic-like' LCEs reported by Berrow *et al.* (3, 4); this further verifies that nLCE-72 is outside of the formulation limitations for a monodomain nematic templated LCE. Moreover, by comparing the correlation lengths of these materials, we were able to characterise the extent of the long-range ordering present in these materials. We observed that the monodomain nematic LCEs in this work demonstrated a low correlation length, through only 2 – 3 'end-to-end' spacings. Conversely, the smectic-like nLCE-72 exhibited a long-range ordering that extended further, through 3 – 4 layers, yet is still a weaker order when compared to the smectic LCEs by Berrow *et al.* (3, 4) which reached across 4 – 6 layers.

Finally, the X-ray Scattering in Chapter 5 also revealed a closer packing of the network for LCEs with a higher mesogenic content, which strongly indicated an increase in the density. Using aqueous glycerol solutions, the density was measured to be between 1.12 and 1.16 g/cm^3 for monodomain nematic LCEs between 56 and 72 mol% mesogenic content, respectively; this corresponded to a 4% increase in the density for a 16% increase in the mesogenic content of the network.

The penultimate result chapter, Chapter 6, explored the optical properties of this series of LCEs. The average refractive index and the refractive index anisotropy were shown to be well predicted by the composition of the network and can therefore be selected. Indeed, the refractive indices of the monodomain nematic LCE, n_o and n_e, demonstrated up to an 0.026 increase for a 10 mol% increase in the mesogenic content, with the birefringence accordingly changing by ~18%. All of the refractive indices were then shown to decrease linearly with an increase in temperature, with values of the temperature coefficients of refractive index close to those in literature for optical plastics (~ 10^{-4} K^{-1}). This linear relationship with temperature evidenced that these materials are dominated by the temperature-dependent density within the temperature range of ~ 20 - 60°C.

Finally, Chapter 7 presented evidence for a continuous order-to-disorder transition in a nematic LCE (nLCE-62) by assembling evidence from previous results chapters and providing new evidence. Chapter 4 presented that there is no indication

of a nematic-to-isotropic transition in the polymerized nematic LCEs, up to an investigated temperature of 250°C. The temperature-dependent order parameter was briefly introduced in Chapter 5 and revisited in Chapter 7, to provide the main evidence of a continuous transition. The temperature-dependent order parameters of the monodomain nematic material (nLCE-62) were measured using Raman Spectroscopy and were shown to significantly decrease upon heating to 135°C. Furthermore, an increase in the optical transparency of the polydomain nematic template of nLCE-62 with a rise in the temperature, also indicated an order-to-disorder transition.

For a continuous transition to indeed occur in these materials, there must be an applied field of sufficient strength across the material. In line with findings in literature (5, 6), the nematic templated LCEs in this acrylate family show evidence of a continuous order-to-disorder transition, which occurs due to a strong internal strain generated by the crosslinking within these materials.

8.2 The Optimal Material for Impact Resistant Devices

In this thesis, a series of LCEs with varied templates and compositions have been explored to uncover the best candidate for laminates in impact resistant glass. Of the three templates investigated (polydomain nematic, monodomain nematic, and isotropic), the polydomain nematic would be unsuitable for use in glass due to the high opacity of the material. The isotropic and monodomain nematic templates show good transparency and energy dissipation, however only materials with the monodomain nematic template are capable of auxetic behaviour, therefore lending themselves to be unique candidates for impact resistant devices.

Now that we have selected the best template for this application, we shall select the best composition. Of all the compositions investigated, nLCE-66 has the greatest dissipation capabilities whilst still retaining an auxetic response, and this material is highly dissipative around room temperature. Therefore, this composition is the best overall candidate for impact resistant devices at ambient temperatures. By increasing the mesogenic content slightly (~ 68-70 mol%) the dissipative properties of the material could be enhanced, with optimal operational temperatures shifting higher, however an auxetic response may not be achievable. By lowering the mesogenic content of this network (~ 62-64 mol%), the strain threshold for an

auxetic response can be lowered, the optimal temperature window for the material can also be reduced, however the material's dissipative capabilities could also decline.

As aforementioned, the monodomain nematic templates exhibit a good optical transparency. However, another consideration for impact resistant glass is the refractive index matching of the laminate to the glass to minimise dispersion and reflective losses. The refractive index for glass is ~ 1.52 which is ~ 4 % lower than the average refractive index of the monodomain nematic LCEs at ~ 1.58 (this is equivalent to the isotropic refractive index). However, we have proved that the optical properties for these materials are highly tuneable and can be selected by the composition.

There may however be formulation limitations that will ultimately restrict the selection of the LCE composition, and this has been a recurrent theme throughout this work. These limitations have been shown for both a low and a high mesogenic content. For LCEs with lower mesogenic content, the T_{NI} of the precursor mixture is lower and closer to room temperature, which makes the formation and the polymerization of nematic LCEs difficult to achieve. The lower compositional limit has been experimentally realised in the phase separation of nematic templated LCEs. For higher mesogenic content LCEs, the increasing T_g of the LCE film is a restriction for these materials. The increase in the smecticity of the materials is also a consideration, since the material with the highest mesogenic content (nLCE-72), failed to show an auxetic response.

8.3 Future Work

Throughout this work, routes to optimize the specific properties of these materials have been outlined. However, some questions remain unsolved, and some investigations require further confirmation:

- In Chapter 4, the dissipative properties and the auxetic response of the monodomain nematic LCEs were measured. The role of composition on the dissipation and on the auxetic response was investigated, however the direct impact of the auxetic response on the energy dissipation was not explored. For future work, the dissipation of these materials should be measured around the auxetic threshold by operating DMTA at higher strains.

- In Chapter 5, the X-ray Scattering results showed that a change in the LCE composition causes a change in the correlation length of these materials and evidences some smectic characteristics of the nematic materials. The failure of the auxetic response in the highly ordered and smectic-like materials should be further explored, by studying the impact of strain on the network structure and the correlation length.
- Furthermore, the formation of the network structure using time-resolved X-ray Scattering would be interesting to examine; it is known that the removal of 6OCB changes the network density, but a question remains on how this may also impact the fundamental network structure and phase.
- In Chapter 7, evidence of an order-to-disorder transition in a nematic templated LCE (nLCE-62) was presented. Importantly, this work indicated that a continuous transition occurs in these materials, which has been previously seen for materials with a sufficient applied field. Therefore, collaborative work into understanding the role of the crosslinking density, the corresponding internal strain, and the nature of the order-to-disorder transition has been ongoing. This collaborative work has included an adapted Maier-Saupe theory to encompass the strain effects, developed by Victor Reshetnyak. The order-to-disorder transitions of series of varied crosslinker density LCEs within this acrylate family have been investigated experimentally by Thomas Raistrick, Matthew Reynolds, and Emily Cooper. The combined experimental and theoretical work are currently in a paper in preparation.

8.4 References

1. Barnes, M., Cetinkaya, S., Ajnsztajn, A. and Verduzco, R. Understanding the effect of liquid crystal content on the phase behavior and mechanical properties of liquid crystal elastomers. *Soft Matter.* 2022, **18**(27), pp.5074-5081. Available from: https://doi.org/10.1039/D2SM00480A
2. Jull, E.I.L., Mandle, R.J., Raistrick, T., Zhang, Z., Hine, P.J. and Gleeson, H.F. Toward In Silico Design of Highly Tunable Liquid Crystal Elastomers. *Macromolecules.* 2022, **55**(11), pp.4320-4330. Available from: https://doi.org/10.1021/acs.macromol.2c00587

3. Berrow, S.R., Raistrick, T., Mandle, R.J. and Gleeson, H.F. Structure–Property Relationships in Auxetic Liquid Crystal Elastomers—The Effect of Spacer Length. *Polymers.* 2024, **16**(14), p.1957. Available from: https://www.mdpi.com/2073-4360/16/14/1957
4. Berrow, S.R., Raistrick, T., Mandle, R. and Gleeson, H.F. Dataset associated with "Structure-Property Relationships in Auxetic Liquid Crystal Elastomers – The Effect of Spacer Length". [Online]. 2024. Available from: https://doi.org/10.5518/1449
5. Disch, S., Schmidt, C., Finkelmann, H. Nematic elastomers beyond the critical point. *Macromolecular Rapid Communications.* 1994, **15**, pp.303-310. Available from: https://doi.org/10.1002/marc.1994.030150402
6. Cordoyiannis, G., Lebar, A., Zalar, B., Žumer, S., Finkelmann, H. and Kutnjak, Z. Criticality Controlled by Cross-Linking Density in Liquid Single-Crystal Elastomers. *Physical Review Letters.* 2007, **99**(19), p.197801. Available from: https://doi.org/10.1103/PhysRevLett.99.197801